MODELING OF CERAMIC BODIES DRYING AND FIRING PROCESSES AND THEIR EFFECTS ON PROPERTIES OF SINTERED CERAMIC BODIES

J. M. N. Jayaweera

208031L

Doctor of Philosophy

Department of Chemical Process and Engineering
Faculty of Engineering

University of Moratuwa
Sri Lanka

November 2024

MODELING OF CERAMIC BODIES DRYING AND FIRING PROCESSES AND THEIR EFFECTS ON PROPERTIES OF SINTERED CERAMIC BODIES

J. M. N. Jayaweera

208031L

Thesis/Dissertation submitted in partial fulfillment of the requirements for the degree

Doctor of Philosophy

Department of Chemical Process and Engineering

Faculty of Engineering

University of Moratuwa

Sri Lanka

November 2024

DECLARATION

I declare that this is my own work and this thesis/dissertation does not incorporate without acknowledgement any material previously submitted for a degree or diploma in any other University or Institute of higher learning and to the best of my knowledge and belief it does not contain any material previously published or written by another person except where the acknowledgement is made in the text. I retain the right to use this content in whole or part in future works (such as articles or books).

Signature: Date: 26.11.2024

The above candidate has carried out research for the PhD/~~MPhil/Masters~~ thesis/~~dissertation~~ under my supervision. I confirm that the declaration made above by the student is true and correct.

1. Name of Supervisor: Prof. M. Narayana

Signature of the Supervisor: Date: 26.11.2024

2. Name of Supervisor: Prof. S. U. Adikary

Signature of the Supervisor: Date: 26.11.2024

DEDICATION

I would like to dedicate this thesis to my parents, husband, and daughter; without their cooperation and support, this study will not be completed; they are the very important part of the research.

ACKNOWLEDGEMENT

I would like to express my most sincere gratitude and appreciation to my principal supervisor, Prof. M. A. Narayana, Professor, Department of Chemical Process and Engineering, Faculty of Engineering, University of Moratuwa, Sri Lanka, who provided me with the most invaluable and remarkable opportunity to read for a PhD research degree under his supervision. It is difficult to express in words for his invaluable guidance, encouragement, and support for me throughout the study. His thoughtfulness deeply inspired me to take the correct decision at a crucial stage in the study. Prof. S. U. Adikary, Professor, Department of Materials Science and Engineering, University of Moratuwa, the co-supervisor of the research, with his vast experience and professional knowledge in this specialist field of research, kept me on track with his guidance, supervision, and support throughout the research period. Many thanks are extended to my supervisors for their valuable advice and constructive comments on my research.

Prof. (Mrs.) S. M. Egodage, the Head of the Chemical & Process Engineering Department throughout the period, and all the lecturers of the Department of Chemical & Process Engineering, University of Moratuwa, who helped me in various ways to complete this research successfully, must be specially mentioned.

Mr. V. Sivahar, the Head of Materials Science and Engineering throughout the period, and all the lecturers of the Department of Materials Science and Engineering, University of Moratuwa, who helped me in various ways to complete this research successfully, must be specially mentioned.

I am also grateful to Dr. R. A. C. P. Ranasinghe, Prof. D.M.D.O.K. Dissanayake and Dr. L. D. Ranathunga for all the advice and encouragement that they gave me throughout the time as progress review committee members.

It is my pleasure to extend sincere appreciation to all who rendered support in numerous ways to make my research a success.

ABSTRACT

The ceramic tile industry is continuously exploring novel techniques to improve productivity while maintaining quality products. Optimization of drying and sintering steps of the ceramic tile manufacturing process can significantly enhance the productivity of the ceramic tile manufacturing industry. Thermal and mechanical stresses that occur within the ceramic body during the drying and sintering processes need to be precisely controlled to minimize defects and hence improve productivity. To optimize the drying process, the spatial variation of the moisture exchange rate within the ceramic tile body must be analyzed over time and kept below the critical moisture exchange rate. In the sintering process, controlling the quality of ceramic tiles depends on the spatial and temporal variations in linear shrinkage, MOR, and thermal stress throughout the sintering cycle. For an optimal sintering cycle, the thermal stress must remain below the MOR across both spatial and temporal dimensions. The existing kinetics models developed by previous researchers do not facilitate finding temporal and spatial changes in the moisture exchange rate, linear shrinkage, MOR, and thermal stress of the ceramic tiles, and it is difficult to optimize the drying and sintering processes. This investigation aimed to establish a robust numeric model for the drying and sintering processes of ceramic tile using computational fluid dynamics (CFD). The developed models are capable of predicting the moisture exchange rate, linear shrinkage, MOR, and thermal stress in ceramic tile during drying and sintering and optimizing each process. In this research, a Kaolin source named M2 Kaolin-based tile body composition was selected. The drying and sintering behaviors of ceramic tiles were investigated. Computational fluid dynamics (CFD)-based numerical models were developed separately for the drying and sintering processes for ceramic tiles. The drying model was used to evaluate the spatial variation of the moisture content in ceramic tiles and optimize the drying process of ceramic tiles for minimum drying time. The sintering model was used to assess the spatial and temporal variation in linear shrinkage, MOR, and thermal stress in the ceramic tile. The sintering process was optimized by accounting for thermal and mechanical stresses, ultimately determining the optimal sintering cycle where thermal stress remains below the modulus of rupture (MOR) throughout the ceramic body. To validate the ceramic tile drying and sintering models, the green body mixture of ceramic tile was prepared. Ceramic tiles were shaped by a powder pressing technique on a laboratory scale. The moisture variation of green ceramic tile with time was determined during the drying process. Dried tiles were sintered in a laboratory furnace by adjusting the maximum sintering temperatures. The structure of the green body mix and sintered ceramic tiles was analyzed. The linear shrinkage and modulus of rupture variation of each sintered tile were determined. Results developed by the simulated drying model were compared with data obtained by experiments conducted using green ceramic tiles. The results of the drying model for green ceramic tiles were validated and comply with the experiment results, and the R-squared value was 0.9. The CFD results regarding the moisture exchange rate of green ceramic tile with drying profiles were analyzed. It

confirmed that the optimum drying time was 60 minutes, and it was reduced by 76.2% of the time compared to the initial drying time. The developed drying model can be applied to optimize the local ceramic tile manufacturing process for improved productivity. The results obtained from the CFD model of the sintering process and the experimental outcomes of linear shrinkage and modulus of rupture were compared. The results of CFD simulation for the linear shrinkage and modulus of rupture of the tiles were validated and concurred with experimental outcomes, and the R-squared value of the results was 0.9. The CFD results regarding the thermal and mechanical stress of the ceramic tile body were analyzed, and it was confirmed that the optimum dynamic rate sintering cycle included 51.6 °C/min heating rate between 30-550 °C, 27.6 °C/min heating rate between 550-1200 °C, 57.0 °C/min cooling rate between 1200-1000 °C, and 19.8 °C/min cooling between 1000-30 °C. The optimum sintering time was 96 min, and the sintering time of the ceramic tile was reduced by 87.2% compared to the initial sintering profile. Hence, the developed CFD sintering model can predict the temporal and spatial changes in linear shrinkage and modulus of rupture of ceramic tiles through sintering without laboratory experimental effort. Therefore, the sintering model facilitates finding the exact sintering cycle associated with linear shrinkage and modulus of rupture. Finally, the quality of the ceramic tile is improved, and the drying and sintering times of ceramic tile are reduced. The developed CFD models for the drying and sintering processes enhanced the productivity of the ceramic tile, and the cost of production was reasonably lower.

Keywords: Ceramic Tile, Drying, Kaolin Clay, Numerical Modeling, Sintering

TABLE OF CONTENTS

LIST OF FIGURES

Figure **Description** **Page**

LIST OF TABLES

Table **Description** **Page**

LIST OF ABBREVIATIONS

Abbreviation	Description
CFD	Computer Fluid Dynamics
CM	Critical Moisture
CRP	Constant Rate Period
FRP	Falling Rate Period
DTA	Differential Thermal Analysis
TGA	Thermogravimetric Analysis
SEM	Scanning Electron Microscope
XRD	X-ray Diffraction Analysis
LOI	Loss on Ignition
MOR	Modulus of Rupture
EDXS	Energy Dispersive X-ray Spectroscopy
FDM	Finite Difference Method
FEM	Finite Element Method
FVM	Finite Volume Method
LBM	Lattice Boltzmann Method
SPH	Smoothed Particle Hydrodynamics
UDS	User Defined Subroutine
UDF	User Defined Function

LIST OF APPENDICES

CHAPTER 1

1. INTRODUCTION

1.1Background to the Research Problem

In the current economic context, manufacturing industries prioritise cost reduction and energy savings, which support the survival of highly competitive businesses [1], [2]. Manufacturing industries' main strategies are introducing new products and reducing production costs through innovation [1]-[3]. The ceramic product manufacturing process is extremely complex, and the cost of its manufacturing is very high compared to other manufacturing industries [2]-[4]. The ceramics industry is highly concerned with energy savings and controlling defects during the manufacturing process [3]-[5].

Ceramic tiles are a dense material that is characterised by excellent properties such as lower water absorption, high bending strength, abrasion, and stain resistance, etc. These characteristics allow its use in severe applications, both indoors and outdoors, in which a high level of reliability is required [4]-[6].

Ceramic tile is formulated from a mixture of clay material, quartz, feldspar and, dolomite. In general, clay materials contribute to the plasticity and dry mechanical strength of green ceramic tile bodies and give rise to mullite and glassy phase formation during sintering. The feldspar forms a glassy phase at low temperatures and encourages the sintering process. Quartz contributes to thermal and dimensional stability since it is the constituent with the highest melting temperature. An enhancement of the densification kinetics is often pursued by adding dolomite, which should improve the physical properties of the liquid phase by increasing its surface tension and decreasing its viscosity [4], [5], [7].

The main steps in manufacturing ceramic tiles are powder preparation, forming, drying and, sintering [5]. The body mix of the ceramic tile is prepared using appropriate raw materials and particle size or size distribution [4]-[9]. So, powder preparation is the first step in the ceramic tile manufacturing process. The forming process is given the shape of the tile, and powder pressing is used in most ceramic tile industries. The drying and sintering steps are critical for the ceramic tile production industry, and numerous defects can occur throughout these processes [6]-[9]. The drying process is a compulsory step to remove the moisture content from the ceramic tile body before

the sintering process. These processes consist of highly complex heat and mass transfer phenomena [10].

The drying behavior of the green ceramic tile body depends on the airflow rate, drying temperature, relative humidity, packing density, dimension of the tile, initial moisture content, etc. [10], [11]. Internal structure varies, and internal stresses appear during the drying process of ceramic tile. Drying defects appear due to uneven shrinkage or unwanted deformation of the green ceramic tile body, and undesired deformation affects the properties of sintered ceramic tile. Uneven shrinkage or undesired deformation can be avoided by controlling the drying rate of the green ceramic tile body [10]-[12]. However, raw material selection, blending, and shaping also affect the quality of sintered ceramic tile [7]-[9].

The sintering of ceramic tiles is a highly complicated process, and the great predominance of ceramic tile quality-relevant obstacles commence during the sintering process. Many factors affect the quality of ceramic tiles, such as the chemical composition and mineralogical structure of raw materials, body composition of each raw material, average particle size and distribution, sintering temperature, heating rate, and cooling rate [4]-[9]. Dimensional variation, or shrinkage, is utilised as a criterion to modify the size of the sintered ceramic tiles [5]-[7], [16]-[22]. The shrinkage of ceramic tiles has an important role in the manufacturing process because adjusting the shrinkage can control the physical properties and mechanical characteristics of sintered ceramic tiles, including bulk density, water adsorption, strength, and modulus of elasticity [4], [6]-[9].

Various transformations occur in the ceramic tile body mix between 200 °C and 800 °C, for example, eliminating unbound water, combustion of organic substances, transforming α-quartz into β-quartz, dihydroxylation of clays, and decomposition of carbonates. [4], [5], [23]-[27]. The main physicochemical reactions occur between 850 °C and 1350 °C [23], [24], [27].

The ceramic tile industry is continuously exploring novel techniques to improve productivity while maintaining quality products. Optimization of drying and sintering steps of the ceramic tile manufacturing process can significantly enhance the productivity of the ceramic tile manufacturing industry. Thermal and mechanical stresses that occur within the ceramic body during the drying and sintering processes need to be precisely controlled to minimize defects and hence improve productivity

[11], [24]. But the exact mechanical and physical properties, including thermal stress and mechanical stress, of ceramic tiles associated with the drying and sintering cycles are difficult to verify experimentally. The current ceramic tile industry requires worker expertise to determine the best drying and sintering cycles through trial-and-error; these cycles are not provided with precise mechanical and physical characteristics as needed. Therefore, it affects the quality of the final ceramic tiles, and production costs also increased due to the large amount of experimental work.

1.2 Research Aims and Objectives

The drying and sintering operation of the ceramic tile is simultaneous and combined with the energy and mass transmission approach, and this phenomenon can be explained by numerical models that provide pertinent details from a thermodynamic perspective. In this study, 3D dynamic models were developed for the drying and sintering processes separately. The aim of this investigation was to establish a robust numerical model for the drying and sintering processes of ceramic tile using CFD. The model solvers were created with OpenFOAM, which is an open-source CFD program. The developed models were validated by the experimental outcomes, and the model is capable of predicting the physical and mechanical property variations in ceramic tile during drying and sintering and optimising each process. Specific objectives of this research are as follows:

i. To determine the drying and firing kinetics of ceramic bodies with known chemical composition.
ii. To develop a three-dimensional CFD model for the drying and firing processes of ceramic bodies.
iii. To validate the developed model by comparison between the simulated and experimental data.
iv. To optimise the drying and firing processes of ceramic bodies to minimise energy (manufacturing cost) requirements by maintaining the quality of the product.

1.3 Significant of the Research

In this study, 3D dynamic models were developed for the drying and sintering processes separately and simulated using the CFD tool. The results of numerical

models can be utilised to assess the spatial variation of temperature, mechanical and physical characteristics of sintered ceramic tile, and moisture content within the green ceramic tile body. The developed models were validated by the experimental outcomes, and the developed CFD model is capable of predicting the temporal and spatial changes in temperature and physical properties of ceramic tiles through drying and sintering without laboratory experimental effort, and the model facilitates finding the exact drying and sintering cycle associated with physical properties. These models are instrumental in optimising the drying and sintering processes. Finally, the quality of the tile is increased, and production costs are also minimised.

1.4Structure of the Dissertation

This thesis consists of seven chapters. Chapter 1 includes a general overview of the study and the scope of the study. The study's review of the literature is presented in Chapter 2. Chapter 3 describes the methodology used to accomplish the objective of the study. Chapter 4 provides results of the experiments. Chapter 5 presents model validation results. The results and discussion of the study are presented in Chapter 6. Chapter-specific nomenclatures and abbreviations are given at the end of each chapter from Chapter 1 to 6. Chapter 7 presents the overall conclusion and the recommendations for future works. Finally, references and appendices are presented.

CHAPTER 2

2. LITERATURE REVIEW

2.1An Analysis of the Drying Process Literature

The drying process is compulsory to remove the moisture content from the ceramic tile body before the sintering process. The moisture content of a ceramic tile body is described as either the moisture content of a dry basis or the moisture content of a wet basis. They are expressed as shown in Equations (2.1) and (2.2).

$$Moisture\ Content\ (dry\ basis) = \frac{kg\ of\ moisture}{kg\ of\ dry\ solid} \quad ---------- \quad (2.1)$$

$$Moisture\ Content\ (wet\ basis) = \frac{kg\ of\ moisture}{kg\ of\ wet\ solid} \quad ---------- \quad (2.2)$$

The physical characteristics that are important in drying, such as the diffusion coefficient, heat capacity, activity of water, and thermal conductivity, are highly dependent on the body's moisture content.

2.1.1. Drying Mechanism

Drying is the removal of moisture adhering to a ceramic tile body by vaporization. Moisture is located on the surface and in the interior of the ceramic tile body, such as capillaries and interstices. When a sample of wet ceramic tile body is dried from initial moisture content to equilibrium moisture content, a typical variation of the moisture content of the ceramic tile sample with time can be shown in Figure 2.1. Equilibrium moisture content (Xe) is the moisture content of the ceramic tile body in equilibrium with the air at a given humidity and temperature. There are many steps involved in the process of drying a ceramic green tile body with constant temperature, relative humidity, and air velocity. The moisture content variation within the porous ceramic tile body is shown in Figure 2.2. The drying rate variations of a green ceramic tile body depending on the moisture content are shown in Figure 2.3 [10], [12], [92].

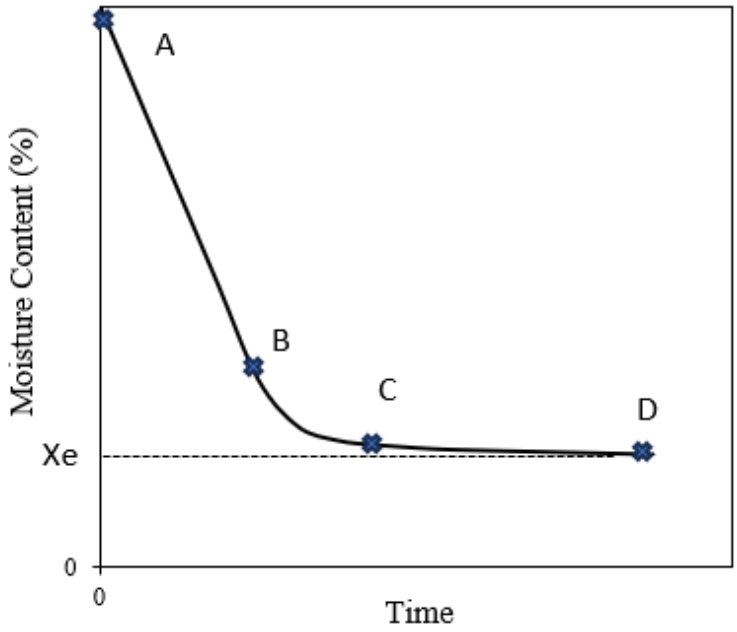

Figure 2.1: Moisture content variation of a green ceramic tile body against the drying time [92]

In general, the drying processes of ceramic tile bodies can be divided into two stages, such as the constant rate period and the falling rate period. During the first drying period, the ceramic tile body enters the hot medium, and moisture evaporation starts from the surface. The moisture migrates from the inner part of the solid rapidly enough to maintain surface saturation. This stage is called the constant rate period because the change in moisture per unit of time remains steady (A to B in Figure 2.1) [10], [11]. Moisture migration can no longer keep the surface steady, and the second drying period starts, which is called the falling rate period. The evaporation occurs through the pores of the green ceramic tile body, with the liquid diffusing out to the surface, and the temperature at the interface starts to increase [13], [14], [15], [92]. At this stage, the rate of the drying process is progressively controlled by an internal diffusion resistance in the drying ceramic tile body [10]-[15]. Furthermore, the falling rate period can be divided into two types based on the kind of ceramic material and the drying circumstances. A relationship between the rate of drying and the moisture content is evident during the first decreasing rate stage (B to C in Figure 2.1). The removal of the body's final remaining moisture content occurs during the second falling rate period. In this situation, the relationship between the drying rate and moisture content is no longer linear (C to D in Figure 2.1). This drying process is completed when the ceramic tile body achieves equilibrium moisture content with the surrounding medium.

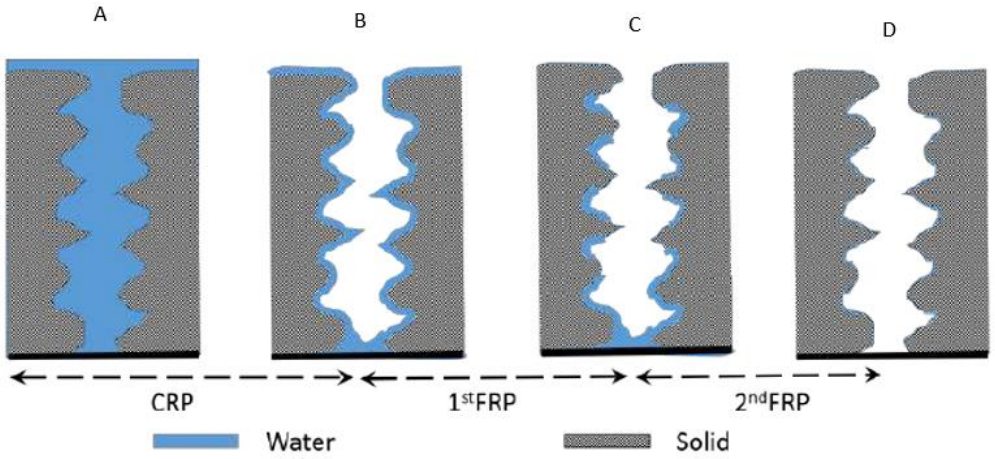

Figure 2.2: Schematic representations of drying stages within a porous ceramic tile body [92]

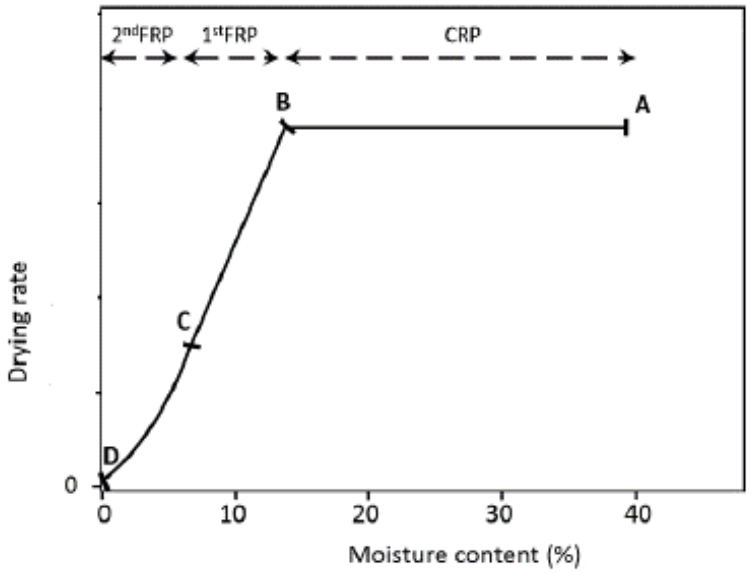

Figure 2.3: Drying rate of a green ceramic tile body against the drying time [92]

2.1.2. Theoretical Framework for Heat and Mass Transferring

The drying process consists of highly complex head and heat and mass transfer phenomena [10], and numerous researchers studied mass and heat transport in the context of drying techniques for porous substances [11]-[15]. K. Murugesan *et al.* (1996) analysed convective drying of porous materials in a one-dimensional [11]. The drying behaviours of porous media were studied by S. Messai *et al.* (2008) [12]. H. Suresh *et al.* (1999) examined the drying of porous material using the finite element

method [13]. K. Khalili *et al.* (2014) investigated numerical simulation for the drying of ceramic using finite elements and machine vision [14]. Juan Carlos Jarque *et al.* (2015) examined the non-isothermal modelling of drying behaviours of ceramic tiles [15].

Heat and mass transfer take place during the drying of the ceramic tile body, and Figure 2.4 shows a schematic representation of the moisture and heat transport of the porous ceramic tile body. Heat transports from the outer surface to the centre of the ceramic tile body. Moisture transports from the centre of the ceramic tile body to its outer surface, and then moisture transfers to the surrounding air of the ceramic tile body. The green ceramic tile body has two forms of water, such as bound and unbound water [10]-[12]. Water located at the ceramic tile body surface is called bound water, which is in layers of water molecules. Unbound water is in the internal structure of the ceramic tile body, and it moves through the ceramic tile body pores during drying [10]-[15]. Fundamental laws of heat and mass transport can be applied to the drying process of ceramic tile bodies.

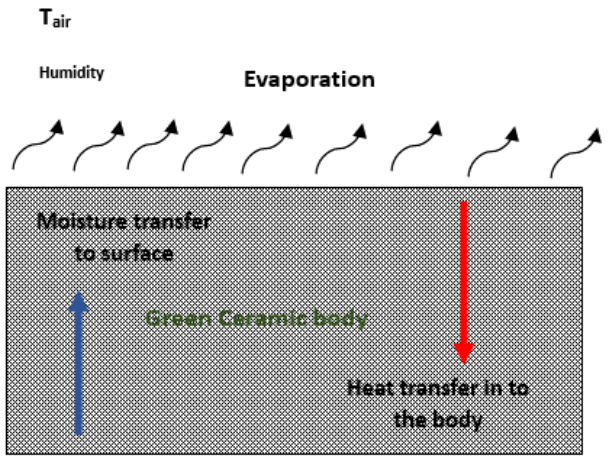

Figure 2.4: A schematic representation of the moisture and heat transport of the porous ceramic tile body [92]

2.1.3. Relation between Microstructure and Moisture Diffusion

The drying rate of a green ceramic tile body can either be constant or change over time. The ceramic tile body's surface is saturated with moisture throughout the constant rate drying period, and the drying rate is controlled by the rate of water evaporation. During the falling-rate drying period, the rate of drying is mainly regulated by the diffusion of moisture from the ceramic tile body's interior to its surface. The ability of moisture to

diffuse from the inside of a ceramic tile body to the surface of a ceramic tile body is defined as effective diffusivity or effective diffusion coefficient (D_m). The effective diffusion coefficient (D_m) is dependent on the internal microstructure and drying temperature of the green ceramic tile [13]-[15]. The internal microstructure of the ceramic tile is varied with bulk density (ρ_D) and moisture content of the green ceramic tile. Then the effective diffusion coefficient of the green ceramic tile was determined using an empirical equation (2.3). The D_0 is the variable parameter that depends on bulk density. The bulk density of green ceramic tile varies according to the particle size distribution and pressing pressure of the ceramic tile body. Therefore, an empirical equation was proposed to determine how D_0 varies with the bulk density of the green ceramic body [15]. The equation is the correlation between D_0 and the bulk density of the green ceramic tile body, as shown in equation (2.4). The internal microstructure of the ceramic tile body also changes as a result of drying shrinkage. Additionally, it is taken into account for empirical equation (2.3) by adding the green ceramic tile body's moisture content (m_D).

$$D_m = D_0\,(1 - b m_D^{\,r})\,Exp\left(-\frac{\theta_D}{T_D}\right) \quad \text{(2.3)}$$

$$\ln D_0 = a_D + b_D \ln \rho_D \quad \text{(2.4)}$$

2.2 An Analysis of the Sintering Process Literature

The firing process of ceramic tiles, referred to as the sintering process, is done in a furnace or kiln with a sintering cycle [39], [40]. Heat and mass transfer between the solid and firing media occur during the sintering process of ceramic tiles. The sintering process of ceramic tiles endures both endothermic and exothermic transformations [6]-[9]. Sintering needs to be done gradually and under supervision in order to prevent fatal defects in the sintered ceramic tiles. The key variables that affect the form of the sintering curve are temperature, time, body composition of ceramic tile and, tile properties, including bulk density [6], [8].

2.2.1. Sintering Kinetics

The body composition of ceramic tile has a significant impact on both the energy used and the environmental emissions during the sintering process. Table 2.1 lists the major physicochemical changes that occur throughout the sintering process of ceramic tiles,

together with the temperature ranges in which these changes occur [40], [111]. In general, the sintering cycle of ceramic tiles consists of mainly three steps, such as preheating, soaking, and cooling [18], [23], [24].

Table 2.1: MAIN REACTIONS TYPES CONSIDERED DURING THE CERAMIC TILES SINTERING PROCESS [40].

Stage		**Physicochemical changes**	**Chemical reaction**	**Temperature (°C)**
Preheating	1	Loss of free water	$H_2O(l) \rightarrow H_2O(g)$	100-120
	2	Combustion of organic matter	$C_xH_yO_z(s) + O_2(g) \rightarrow aCO_2(g) + bH_2O(g)$	200-400
	3	Clay mineral dehydration (Kaolinite)	$Al_2O_3.2SiO_2.2H_2O(s) \rightarrow Al_2O_3.2SiO_2(s) + 2H_2O(g)$	450-700
	4	Quartz (Alpha-beta) inversion	$\alpha - SiO_2(s) \rightarrow \beta - SiO_2(s)$	573
	5	Carbonate decomposition (Dolomite)	$CaMg(CO_3)_2(s) \rightarrow CaO(s) + MgO(s) + 2CO_2(g)$	720-750 900-950
Soaking	6	New crystalline phase formation	$Al_2O_3(s) + SiO_2(s) + CaSiO_2(s) \rightarrow CaO.Al_2O_3.2SiO_2(s)$ $CaO(s) + SiO_2(s) \rightarrow CaO.SiO_2(s)$ $2MgO(s) + 2SiO_2(s) \rightarrow 2MgO.SiO_2(s)$ $CaO(s) + MgO(s) + 2SiO_2(s) \rightarrow CaO.MgO.2SiO_2(s)$ $2CaO(s) + MgO(s) + 2SiO_2(s) \rightarrow 2CaO.MgO.2SiO_2(s)$ $2CaO(s) + Al_2O_3(s) + SiO_2(s) \rightarrow 2CaO.Al_2O_3(s).SiO_2(s)$ $Al_2O_3.2SiO_2(s) \rightarrow \left(\frac{1}{3}\right)3Al_2O_3.2SiO_2(s) + (\frac{4}{3})SiO_2(s)$	900-1200
	7	Glassy phase formation	$K_2O.Al_2O_3.6SiO_2(s) \rightarrow K_2O.Al_2O_3.6SiO_2(l)$ $Na_2O.Al_2O_3.6SiO_2(s) \rightarrow Na_2O.Al_2O_3.6SiO_2(l)$	1100-1200

1. Preheating

This stage involves heating the dried ceramic tile to a temperature of around 1100 °C, depending on the nature of the raw materials. Numerous transformations occur in ceramic tile during the preheating stage, as shown in Table 2.1, including the elimination of free water, the burning of organic materials, the allotropic conversion of α-quartz to β-quartz, the loss of OH^- groups in the clays, and the disintegration of carbonates if the composition contains carbonates [19], [20], [23]-[27]. A variety of internal stresses are sustained by the ceramic tile due to various reasons such as volume changes, gas release, and thermal gradient. Cracks will occur if these stresses are greater than the mechanical strength of the ceramic product that is still "unfired." [27], [29].

2. Soaking

The temperature range during the soaking stage is around 1100 °C to the peak temperature, which is typically between 1100 °C and 1200 °C [16], [21], [28]. The majority of the physicochemical changes occur in this stage, such as new crystalline and glassy phase formation. The main physical and mechanical properties of ceramic tile develop in this stage. In particular, ceramic tile shrinkage is increasing, and this shrinkage can regulate the mechanical and physical characteristics of sintered ceramic tile, including bulk density, water adsorption, linear shrinkage, modulus of rupture and, modulus of elasticity [4], [6]-[9], [23].

3. Cooling

At the completion of the heat input, the cooling process starts. The product temperature drops during the cooling phase from its peak temperature to almost room temperature. Due to the low thermal conductivity of ceramic materials, cooling rates in traditional ceramics are essentially limited by the quartz phase transformation at 573 °C [23]-[25]. This produces a volume change that can lead to product cracking if cooling occurs unevenly throughout the material.

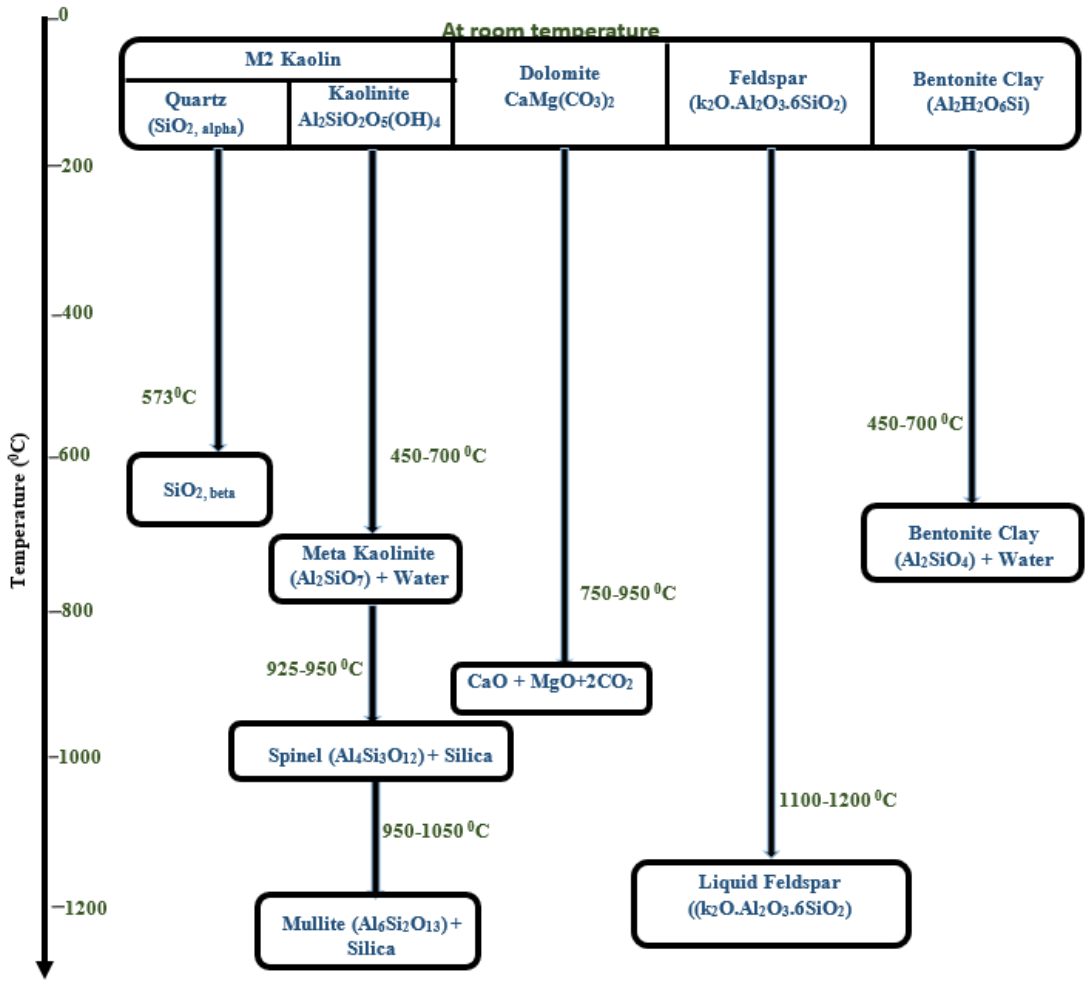

Figure 2.5: Physical and chemical transformation of ceramic tile during the sintering process [23], [24], [40]

In this study, the green ceramic tile body contains M2 Kaolin, feldspar, dolomite, and bentonite clay. The M2 Kaolin is a mix of quartz and kaolinite. Figure 2.5 shows the physical and chemical transformation of ceramic tile during the sintering process. Initially, the kaolinite and bentonite clays are dehydrated at temperatures between 450 and 700 °C [25]-[27]. The alpha phase of quartz transforms to beta quartz at temperatures at 573 °C, and the dolomite decomposes and forms CaO, MgO, and CO_2 at temperatures between 750 and 950 °C [20], [23], [24]. At temperatures between 925 and 950 °C, metakaolin converts to spinel and silicon. Then, after spinel converts to mullite and silicon at temperatures between 950 and 1050 °C [26], [27]. As the temperature increases between 1110 and 1200 °C, the solid feldspar converts to liquid form [23], [24].

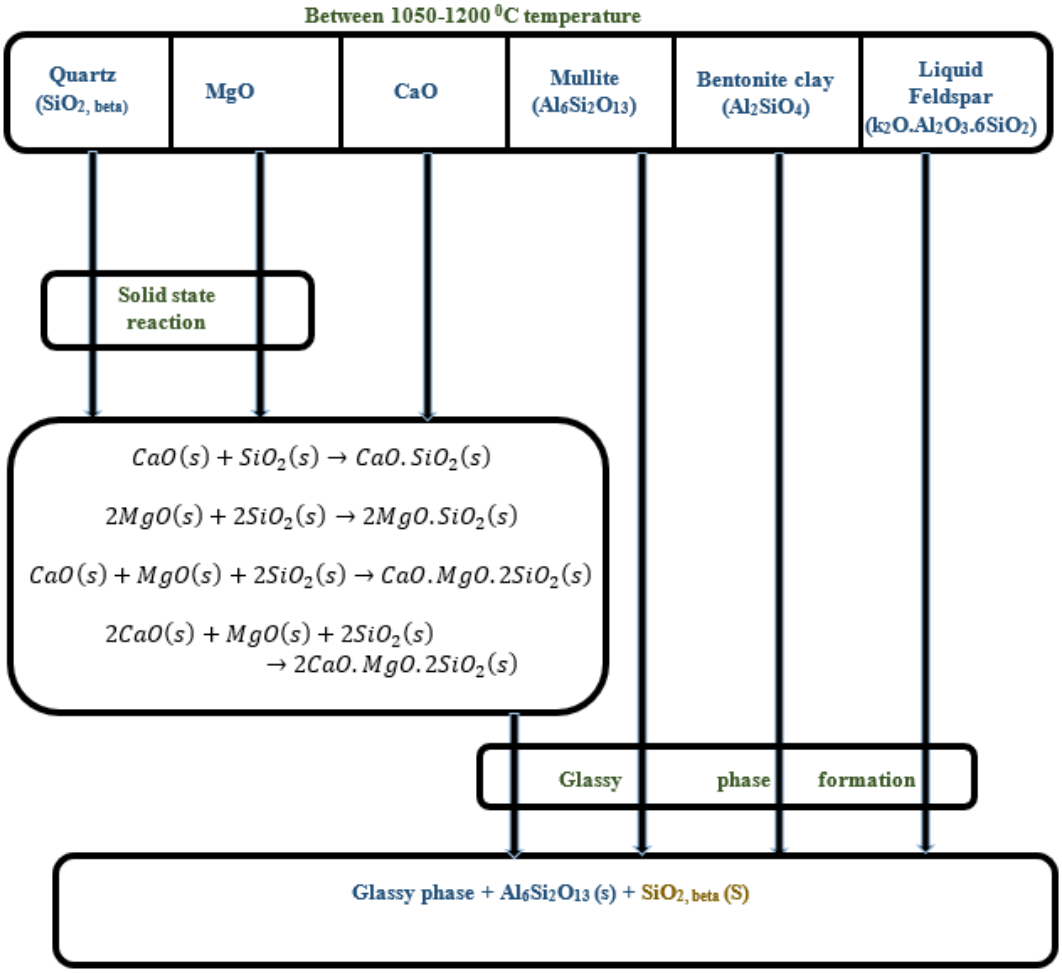

Figure 2.6: Ceramic tile sintering reaction between 1050-1200 ^{0}C temperatures [23], [24], [40]

As shown in Figure 2.6, four solid-state reactions can occur within the ceramic tile body between 1050 and 1200 °C and that form $CaO.SiO_2$, $2MgO.SiO_2$, $CaO.MgO.2SiO_2$, and $2CaO.MgO.2SiO_2$. The gassy phase is created with liquid feldspar, mullite, $CaO.SiO_2$, $2MgO.SiO_2$, $CaO.MgO.2SiO_2$, and $2CaO.MgO.2SiO_2$. The viscosity of the glassy phase decreases with sintering temperature [40]. Two reactions occur during the cooling process, as shown in Figure 2.7. The glassy phase transformation occurs at temperatures between 1200 and 1000 °C. The beta phase of quartz transforms into alpha quartz at a temperature 573 °C [21]-[23].

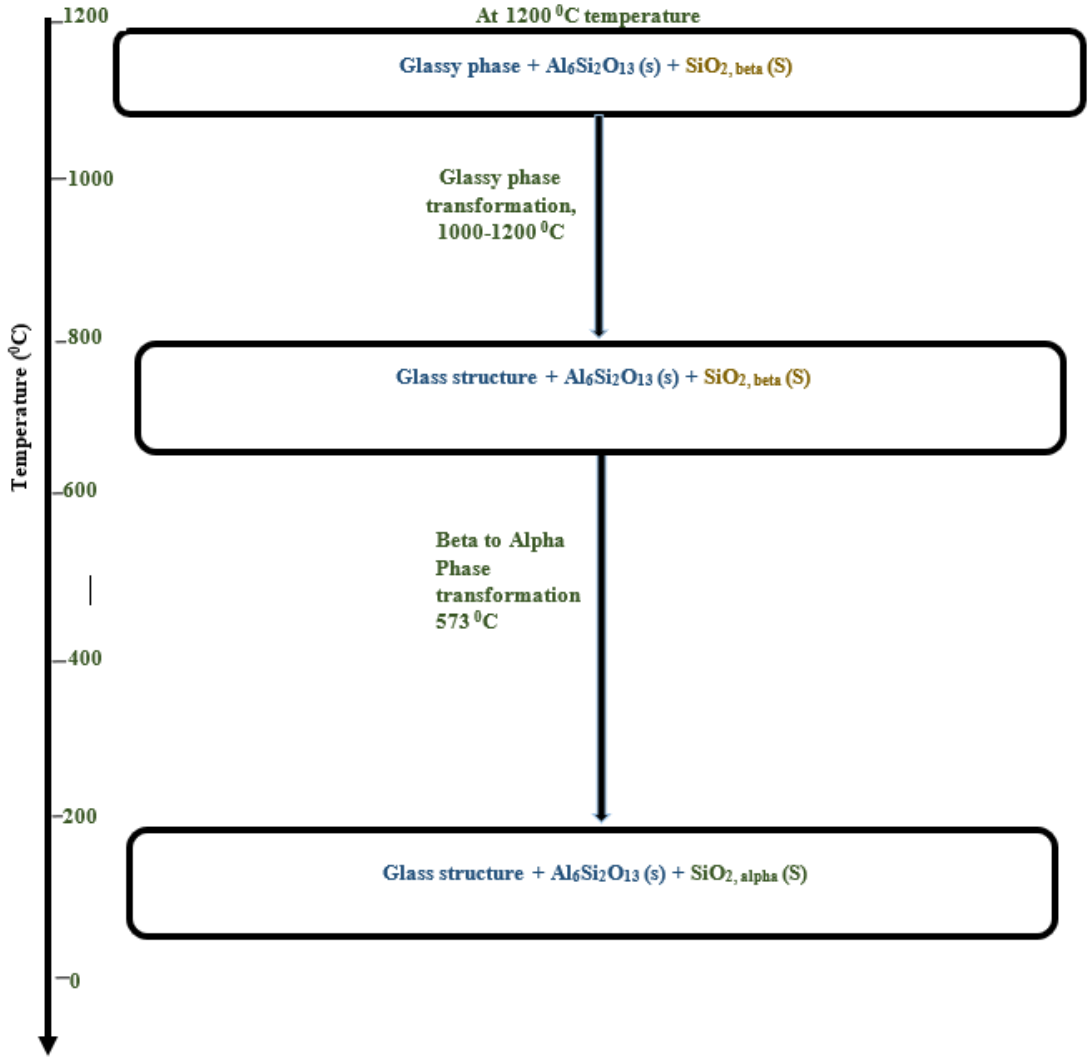

Figure 2.7: Ceramic tile cooing reaction [23], [24], [40]

2.2.2. Development of Physical and Mechanical Properties of Ceramic Tiles during Sintering

Numerous research studies have examined laboratory kinetic models for the sintering behaviour of different ceramic materials at varying sintering temperatures and times [28]-[36]. Orts *et al.* (1993) analysed the densification of low-porosity ceramic pieces and reduced the porosity of the ceramic pieces with sintering temperature and sintering profile through a kinetic model [28], [29]. Zheng *et al.* (1999) used a sintering model to investigate the sintering mechanisms of advanced ceramic materials, and Yürüyen *et al.* (2009) investigated the kinetics and behaviour of porcelain ceramic sintering, which was developed using glass and fly ash residue [30], [31]. Salem *et al.* (2009) investigated the densification of porcelain ceramic containing nepheline syenite using

a kinetics model [32]. Salem *et al.* (2010) used a kinetic model-based method to study the variation of linear shrinkage of porcelain ceramic containing nepheline syenite during the sintering process [33]. Cargnin *et al.* (2011) combined a heat transfer numerical model and a linear shrinkage model with the sintering behaviour of ceramic tiles, which was simulated by varying sintering times and temperatures. This model was used in both laboratory and industrial scales to produce ceramic tiles made by single-cycle sintering [34]. The kinetic model was studied for Predicting Viscosity and Surface Tension at High Temperatures of Porcelain Stoneware Bodies by S. Conte *et al.* (2018) [35]. Igor Stubna et al. (2011) investigated the variation of fracture strength of Kaolin base ceramic materials during the sintering process using a kinetic model [36].

Vitrification is the main mechanism for densification of ceramic tile [23], [24]. Feldspar melting facilitates the creation of a viscous melt during the sintering process at temperatures above 1100 °C. A liquid state of feldspar near the particles begins to form during the sintering process, and a process accelerating capillary pressure (*Pc*) develops at the interaction location [4], [5], [23], [24], [25], [27]. The melted feldspar filled up the pores of the tile body, and the particles moved nearer together by capillary pressure. While pore size and shape differ simultaneously, the body of the ceramic tile exhibits rising shrinkage and decreasing porosity. The amount of liquid phase changes with the sintering temperature. At approximately 1180 °C –1200 °C, the intermediate states commence to close their pores and eliminate interpore connections. Vitrification influences sintering shrinkage, reducing porosity, and the improvement of the physical and mechanical properties of the ceramic tile body [23], [24], [27].

2.3Research Gap

The research gap was identified for both the drying and sintering processes of ceramic tile. The previous researchers suggested kinetic models to determine the moisture exchange rate for ceramic tile during the drying process; however, prior studies do not support the finding of spatial variation of moisture exchange rate within the ceramic tile body. In the optimization of the drying process, spatial variation of the moisture exchange rate of the ceramic tile body needs to be analyzed, and it must be controlled below the critical moisture exchange rate. In this study, a CFD model was developed for the drying process, especially to examine the spatial variation of the moisture

exchange rate within the green ceramic tile body. This approach offers a significant advantage in determining the optimum drying temperature for minimum drying time by accounting for the spatial differences in moisture exchange across the ceramic tile.

Numerous research studies have examined kinetic models for the sintering behavior of different ceramic materials at varying sintering temperatures and times. The existing kinetics models do not facilitate finding temporal and spatial changes in the linear shrinkage, MOR, and thermal stress of ceramic tiles. In the sintering process, spatial and temporal variation of linear shrinkage, MOR, and thermal stress of the ceramic tile body associated with the sintering cycle are most important for controlling the quality of ceramic tile, and it is required for optimization of the ceramic tile sintering process. The CFD model developed in this study for the sintering process can predict the temporal and spatial changes in linear shrinkage, MOR, and thermal stress in ceramic tile during the sintering processes. The model is used to find the most appropriate sintering cycle for linear shrinkage and MOR. In the optimization of the sintering process, temporal and spatial changes in MOR and thermal stress of ceramic tile were obtained, and the optimum dynamic temperature profile for minimum sintering time was estimated using a developed sintering model.

As a result, the quality of the ceramic tile is enhanced, and the drying and sintering times are reduced. The developed CFD models for the drying and sintering processes improve ceramic tile productivity.

2.4Modelling Using Computational Fluid Dynamics

A computer-based technique for modelling the behaviour of systems involving fluid flow, heat transfer, and other associated physical processes is called computational fluid dynamics. It functions by using a specific form of equations for fluid flow to be solved over a region of interest with known boundary conditions. Momentum, heat, and mass transfer included in each process are described using the Navier-Stokes equations. These partial differential equations have no known general analytical solution but can be discretised and solved numerically [41], [42].

Five major numerical methods are used in CFD solutions, such as the finite difference method, finite volume method, finite element method, lattice Boltzmann method, and smoothed particle hydrodynamics [41]-[44], [113], [114]. Each nodal point of the grid

is used to describe the fluid flow domain in FDM. FDM approximations to the partial derivatives of the governing equations are produced using Taylor series expansions. Before the governing equations in FEM are integrated across the whole computational domain, they are initially tentatively calculated by multiplying them by the shape functions. LBM uses the Boltzmann equation to approximate macroscopic fluid phenomena as mesoscopic shock events of fictitious particles. The region of interest is segmented into tiny sub-regions known as control volumes in FVM. For every control volume, the equations are discretised and solved repeatedly. As a consequence, it is possible to approximate each variable's value at particular places within the domain. This makes it possible to identify the flow's behaviour [41]-[44]. The SPH is a Lagrangian particle-based discretisation scheme. Instead of using a mesh, particles are moving around based on them. The particles then simply follow the flow; they can detach from one another and may come together again later [113]-[114].

The ceramic tile drying and sintering process involved both heat and mass transformation. The finite-volume method’s strength is that it only needs to do flux evaluation for the cell boundaries. Then, the finite volume method is capable of modelling the drying and sintering processes of ceramic tiles. There are many commercial general-purpose CFD programs available, such as Fluent, ANSYS, OpenFOAM, and Flow 3D. OpenFOAM is a leading software that is available as open-source, and its programs can be customised according to the requirements of customers. In this research, OpenFOAM is used to develop and simulate the ceramic tile drying and firing processes.

Figure 2.8 shows the CFD simulation steps using any general-purpose CFD program available. A simulation problem using CFD starts with a three-dimensional drawing of the geometry of the system. A precise numerical solution of the equations requires appropriate discretisation of the computational volume due to the nonlinear equations. Precisely meshing the computational domain is just as essential as delineating the physical domain. A poorly conditioned model might produce wildly erroneous results; thus, before the simulation, the mesh's quality, such as aspect ratio and skewness, has to be assessed.

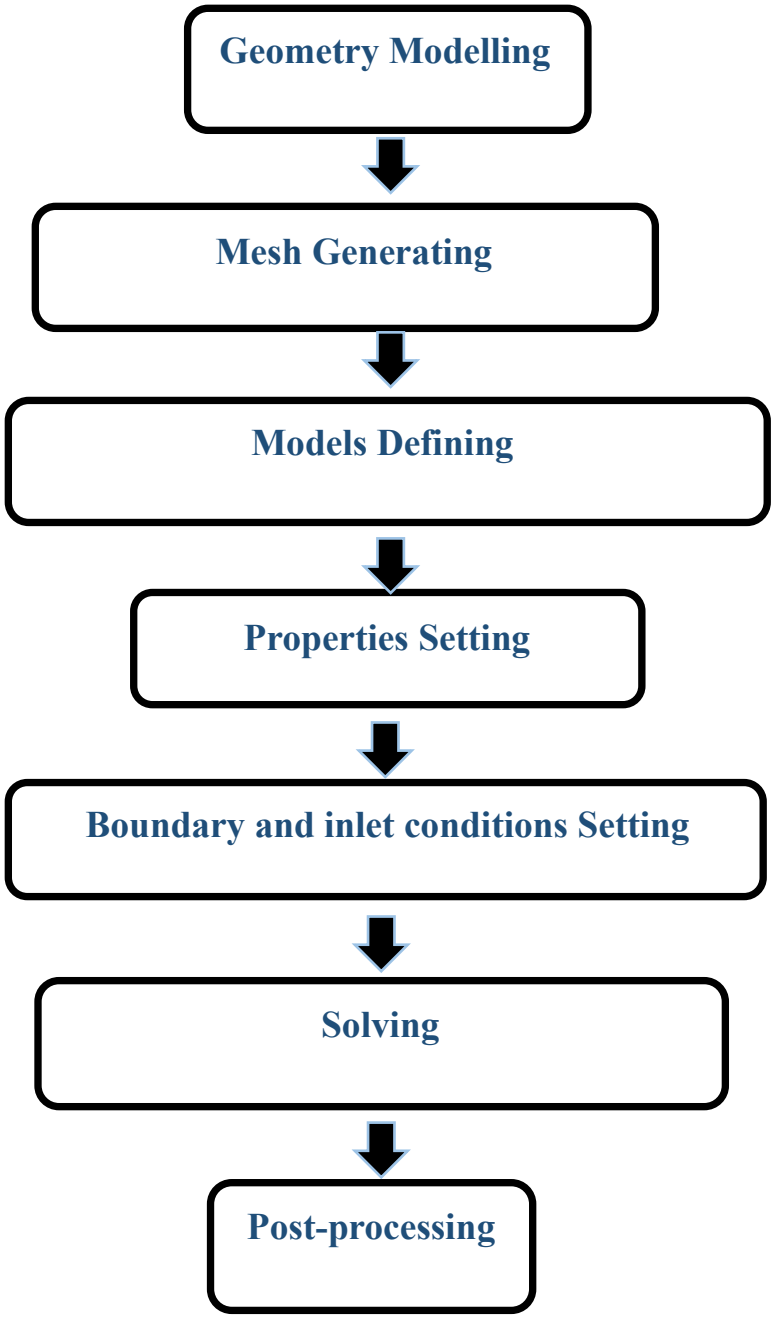

Figure 2.8: Flowchart of the simulation steps using CFD program [40], [43]

The drying and firing processes involved chemical reactions, radiation, and multiphase flows, and the most appropriate models were defined. Several parameters must be set for proper simulation of the model. The default choices are often the best option; however, depending on the situation, the user may be able to identify more appropriate options. It is also possible to write the user's own model as a user-defined

subroutine/function (UDS/UDF) in the majority of commercial CDF systems. In order to produce heat and emissions during the drying and sintering processes, this research uses incompressible, Navier’s stock, laminar flow. It is necessary to choose suitable models for simulation in this respect. All physical properties, such as thermal expansion, thermal conductivity, viscosity, and density, of the fluids must be defined according to their temperature and pressure distribution. To calculate the properties, one may alternatively write a UDS/UDF and apply it to the CFD program.

It is necessary to establish boundary conditions, including walls and other barriers such as air entry and exit temperatures, pressure, velocity, etc. Defined geometrical systems are also necessary. Defining symmetry guarantees a speedy outcome by requiring less processing. It is also necessary to supply beginning circumstances for transient simulations or a first estimate to begin iterations for steady-state simulations. The continuity, momentum, energy, radiation, and combustion equations are all solved concurrently in CFD.

In post-processing, evaluating the solution's quality is the primary goal. The question of whether the solution is independent of the convergence criterion or the grid size has to be answered. It is necessary to verify that the appropriate boundary conditions and model were selected. Local information regarding produced emissions, temperature distribution, and fluid movements may be obtained by analysing the final simulation results.

CHAPTER 3

3. METHODOLOGY

3.1 Numerical Model Development for Drying Process

3.1.1.Governing Equations for Drying Process

The developed mathematical model in this study was based on the below physical assumptions [10]-[15], [45], [46]:

- The solid phase consists of small, discrete grains, and the grain size is much smaller than the size of the ceramic tile. The liquid phase consists of a single component.
- The ceramic tile body's porosity has remained constant throughout time.
- The green ceramic tile body has homogeneous temperature distribution throughout the drying process due to the low drying temperature.
- Knowledge of the ceramic tile body's transport properties and microstructure is applied to determine effective transport coefficients.
- Heat and mass transfer at the surface of the ceramic tile body occur due to differences in temperature and partial pressure between the surface and the external medium.
- Viscous dissipation, body forces, and compressional work other than gravity are negligible.

In the CFD modelling approach, mass and heat transfer for green ceramic tile bodies are effectively described by the governing equations. The equation (3.1) describes the variation of moisture transfer for green ceramic tile bodies.

$$\frac{\partial m_D}{\partial t} = \nabla.(D_m \nabla m_D) \quad \text{----------} \quad (3.1)$$

As shown in equation (2.2), the effective diffusion coefficient (D_m) is varied with the temperature, packing density, and moisture content of the green ceramic tile. According to the reference [15], the effective diffusion coefficient is more dependent on temperature and packing density than on the moisture content of the green ceramic tile. Green ceramic tile shows extremely minimal drying shrinkage due to its low initial moisture content. Thus, equation (3.2) was used to calculate the green ceramic tile's effective moisture diffusion coefficient.

$$D_m = D_0 \, Exp\left(-\frac{\theta_D}{T_D}\right) \quad \text{----------} \quad (3.2)$$

The equation (3.3) describes the variation of heat transfer for green ceramic tile bodies. The green ceramic tile loses some heat during the moisture vaporisation process, which is incorporated in equation (3.3) as a source term G_E. The equation (3.4) can be used to determine the source term G_E.

$$\rho_D C_{p,D} \frac{\partial T_D}{\partial t} = k_D \nabla^2 T_D + G_E \quad \text{----------} \quad (3.3)$$

$$G_E = \gamma \frac{\partial m_v}{\partial t} \quad \text{----------} \quad (3.4)$$

3.1.2.Boundary Conditions for Drying Model

Two boundary conditions need to be applied to the model to solve energy and mass balance equations. The first boundary condition defines the surface temperature of the green ceramic tile body at a given time, as shown in equation (3.5).

$$T_{D,s} \approx T_a \quad \text{----------} \quad (3.5)$$

The second boundary condition defines the moisture content in the green ceramic tile body surface at a given time. The moisture content of green ceramic tile bodies surface is varied with time [10]-[13]. Therefore, an equation was proposed for the variation of surface moisture content with time as shown in equations (3.6) and (3.7).

$$-\frac{dm}{dt} = k_x(m_{surface} - m_{equilibrium}) \quad \text{----------} \quad (3.6)$$

$$k_x = k_0 \, Exp\left(-\frac{\theta_k}{T_D}\right) \quad \text{----------} \quad (3.7)$$

3.1.3.Theoretical Framework for Optimizing Drying Profile

The drying behaviour of the green ceramic tile body depends on the drying rate and homogeneous moisture distribution within the ceramic body during the drying process [47]-[49]. Initially, the moisture fills the pores of the ceramic body, and the pores are opened. The pores are closed when the moisture content reaches the critical moisture content of the tile body during the drying process. If pores are closed unevenly within

the ceramic body, drying cracks can appear due to the moisture-transferring path being closed.

In this research, the drying temperature is constant, and a constant drying temperature was used to define the boundaries of the drying model. It was assumed that the internal green ceramic tile body had homogeneous temperature distribution during the drying process due to the low drying temperature. So, the drying is considered an isothermal process. Moisture is transported through the pores to the ceramic tile surface throughout the drying process. Fick's law states that this diffusion can be correlated to the concentration gradient, as shown in equation (3.8) [50]. Moisture of the ceramic tile surface transports to the surrounding air, and it can be determined using equation (3.9).

$$J_D = -D_m \nabla C \quad \text{(3.8)}$$

$$J_D = \alpha(m - m_{D,e}) \quad \text{(3.9)}$$

The moisture exchange coefficient (α) is a critical factor to control the drying behaviour of ceramic tile bodies [49]. The rate of drying depends on the moisture exchange coefficient of the ceramic tile body. Then the drying was accelerated by increasing the moisture exchange coefficient [50]. Very slow drying of the ceramic tile body (Kaolin base) was considered if $\alpha = 0.000001$ m/s. The drying with the small moisture exchange coefficient between 0.000001-0.000003 m/s causes no cracks. It is possible to increase the drying temperature of the ceramic tile body until the moisture exchange coefficient approaches 0.000003 m/s.

3.2 Numerical Model Development for Sintering Process

Following the physical hypotheses, the mathematical model was constructed for this investigation [33], [39], [40], [51]-[55].

- The ceramic tile comprises only two phases: solid and liquid are collectively treated as one phase, alongside the gas phase.
- The shrinkage of ceramic tile is caused by the formation of viscous melt, and it is called the term "creeping flow liquid." The term "creeping flow liquid" refers to a viscous melt with a Reynolds number of less than 0.1 [53]. That melt's velocity is extremely low, and the liquid phase is not taken into account in this model [54, 55]. The impact of viscous melt flow on the structure of ceramic tiles was investigated using vitrification kinetic model equations [33].

- The separate, tiny grains that appear in the solid phase are far smaller in size than the ceramic tile.
- The thermophysical characteristics of the gas phase are correlated with the characteristics of air.

In the CFD modelling approach, mass and heat transfer are effectively described between two phases of gas and solid by the governing equations, and the source terms incorporate mass and heat interactions into the model. The shrinkage of ceramic tile is caused by the production of viscous melt and the porous filler in the ceramic tile body. The kinetics model was used to explain linear shrinkage, modulus of rupture and, thermal stress phenomena.

The shrinkage, MOR and thermal stress behaviour of ceramic tile vary with the sintering curve and there are many masses of transformation during the sintering. Sintering temperature affects the shrinkage, MOR and, thermal stress of ceramic tiles, and a special variation of temperature exists in ceramic tile bodies throughout the sintering. The strength of the finite-volume method is its ability to perform flux evaluation at cell boundaries, allowing for variable mesh shrinkage across the domain. The developed CFD model, based on the finite volume method, can simulate shrinkage, modulus of rupture (MOR), and thermal stress during the sintering process of ceramic tiles. The shrinkage of each volume concerning temperature and time is examined. Hence, CFD modelling is capable of capturing the temporal and spatial variation in shrinkage, MOR and, thermal stress within the ceramic body.

3.2.1.Kinetics Model for Physiochemical Reactions during Sintering

The external heat and mass interaction of this model is calculated by considering the main reactions of the sintering process, such as the dihydroxylation of clay minerals, quartz transformation, dolomite decompositions, the formation of mullite, and the melting of feldspar [3], [4], [17]-[21]. Initially, the body mix of tile contains kaolinite, quartz, bentonite clay, dolomite, and feldspar, and the mass of each component is given to model as initial conditions. The mass variation of each reaction ($S_{mass\ of\ reaction,\ i}$) was calculated by applying a mass balance to each chemical reaction [40]. The reaction rate of each transformation ($R_{,i}$) can be calculated by using Arrhenius equation 3.10.

$$R_i = m_i \times A_i \times exp\left(-\frac{E_i}{RT}\right) - - - - - \quad (3.10)$$

The heat of each transformation ($Q_{heat\ of\ reaction,i}$) can be calculated by using equation (3.11). Δh_i is the enthalpies of each component..

$$Q_{heat\ of\ reaction,i} = R_i \times \Delta h_i \quad -----(3.11)$$

External heat interactions inside a ceramic tile occur due to two mechanisms: convection and radiation [39], [51], [52]. According to H. Refaey *et al.* (2018) [52], convection heat interaction can be calculated using equations (3.12).

$$Q_{convection} = h_{con} A_s (T_s - T_g) \quad ------(3.12)$$

M. P. Gómez-Tena *et al*. (2011) investigated a specific area of material calculation using particle size distribution [57]. The specific surface area of the material is to be determined from the particle size distribution and density of ceramic tile, as shown in Equation (3.13) [57].

$$A_s = \frac{6 \sum \frac{V_i}{d_i}}{\rho \sum V_i} = \frac{6}{\rho D_s} \quad ------(3.13)$$

The convection heat transfer mostly affects below 800 °C, and D_S is calculated using the particle size distribution of ceramic tile green body mix data as shown in Table 4.2. D. Llorens *et al.* (2006) [58] studied the variation of heat transfer coefficients of convection with velocity during the sintering process. The velocity flux inside the tile is assumed to be zero at beginning conditions, and the convection process has a constant heat transfer coefficient value, which was determined using the nonlinear regression model for the data given in D. Llorens *et al*. (2006) [58].

Radiation heat interaction of ceramic body can be calculated using equations (3.14) [39], [51], [52], [57].

$$Q_{radiation} = h_{rad} (T_s - T_g) \quad ------(3.14)$$

h_{rad} is the coefficient of radiation heat transfer, and it can be calculated using equation (3.15) which is explained in D. Llorens, *et al.* (2006) [58].

$$h_{rad} = 4\sigma \varepsilon_m {T_s}^3 \quad ------(3.15)$$

$\mathcal{E}_m$ is the wall emissivity. The emissivity of the tile body was calculated using the data given in D. Llorens, *et al*. (2006) [58].

3.2.2.Governing Equations for Sintering Process

In the CFD modeling technique, the mass, momentum, and heat transfer are effectively described by the governing equations.

The momentum variation of the gas phase in the ceramic tile body during the sintering process is described in equation (3.16).

$$\frac{\delta \rho_g U_g}{\delta t} + \nabla \rho_g U_g U_g = -\nabla P + \nabla(\mu_g)\nabla(U_g) - S_R \quad ------(3.16)$$

$$S_R = (\frac{Y_{tile}}{K_{tile}})\mu_g U_g \quad -----(3.17)$$

The physical structure of the tile inhibits the gas flow within it. The gas flow resistance is indicated by S_R in the momentum equation. Tile permeability is the key factor influencing the movement of the gas through the ceramic tile body. The porosity of the ceramic tiles impacts the resistance against the flow field. The momentum resistance within the particle was calculated using equation (3.17).

The energy variation of both gas and solid phases in the ceramic tile body during the sintering process is described in equations (3.18) and (3.19).

$$\frac{\delta(\rho_g C_{p,g} T_g)}{\delta t} + \nabla \rho_g U C_{i,g} T_g = \nabla k_g \nabla T_g + Q_{convection} + Q_{heat\ of\ reactions} \quad ------(3.18)$$

$$\frac{\delta(\rho_s C_{p,s} T_s)}{\delta t} = \nabla k_s \nabla T_s + Q_{convection} + Q_{radiation} + Q_{heat\ of\ reactions} \quad --(3.19)$$

The instantaneous mass and volume of the solid phase were utilized to estimate the density of the solid phase (ρ_s) during model simulation.

Ján Ondruška *et al.* (2021) [59] investigated the variation in the thermophysical properties of ceramic samples with sintering temperature. The ceramic samples were produced with Kaolin and natural zeolite, and Kaolin was a major component of each sample of the research. Both the KZ50 sample and this research sample have the appropriate amounts of SiO_2, Al_2O_3, and RO (CaO+MgO). Consequently, the variation

in thermal conductivity (k_s) and specific heat capacity ($C_{p,s}$) of the solid phase of the ceramic tile body throughout the sintering process were evaluated using the thermophysical properties of the KZ50 sample.

The mass variation of gas and solid phases within the ceramic tile body during the sintering process is described in equations (3.20) and (3.21).

$$\frac{\delta m_{i,g}}{\delta t} + \nabla \mathrm{U} m_{i,g} = \nabla D_{i,g} \nabla m_{i,g} + S_{mass\ of\ reactions} \quad ------(3.20)$$

$$\frac{\delta m_{i,s}}{\delta t} = S_{mass\ of\ reactions,i} \quad ------(3.21)$$

$C_{p,g}$, ρ_g , k_g values were taken as similar with air. $D_{i;g}$ is the mass diffusion coefficient of the gas phase, which is determined by the following equation (3.22) [60].

$$D_{i,g} = 0.0018583 \times 10^{-4} \times T_g^{1.5} \left(\frac{1}{M_s} + \frac{1}{M_{air}}\right)^{0.5} \times \frac{10^5}{P\sigma_i^2 \Omega_i} \quad ------(3.22)$$

M_s are molecular weights of species of body mix. The molecular weight of the body mix is changed with the sintering profile, and it is calculated instantaneously during the simulation.

3.2.3.Theoretical Framework of Vitrification

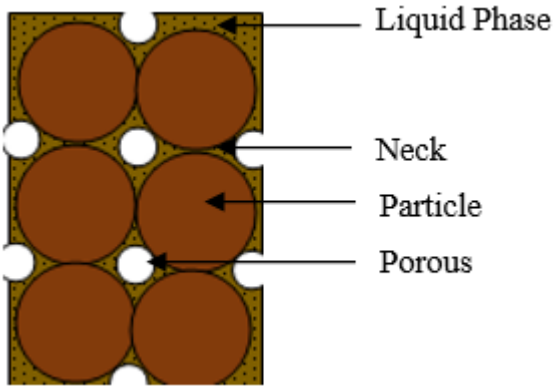

Figure 3.1: Viscous phase Distribution on the surface of the spherical particle

The vitrification of ceramic tile is complex since sintering occurs with the reaction of materials and the formation of new crystalline and amorphous phases. During the sintering process, the particles fuse together, and pores between the particles become more nearly spherical, and the porosity of the ceramic tile body decreases simultaneously [61].

Wetting and spreading activities during liquid phase sintering influence the microstructure of the ceramic tile body by modifying the pore shape. As seen in Figure 3.1, the liquid phase that wets the particle surface will spread throughout it and concentrate at the contact zone, creating necks [23], [24], [28], [33]. There is a compressive stress in the contact area and a negative pressure differential throughout the curved meniscus. The pressure differences across a curved meniscus can also cause the migration of liquid phase between the pores or the migration of liquid from a saturated region to a less saturated region as shown in Figure 3.2.

The formation of viscous melt in the firing process is accomplished by feldspar melting. During firing, at temperatures of about 1100 °C, an important quantity of liquid phase begins to form, surrounding the particles and producing a process-driving capillary pressure (*Pc*) at the contact points [33], [61]. Pores of the tile body are filled with moulted feldspar, and the capillary pressure brings the particles closer together, increasing shrinkage and lowering porosity while simultaneously altering pore size and shape. Raising the temperature increases the quantity of liquid phase and lowers porosity. In intermediate states, at around 1180 °C –1200 °C, pores start closing as interpore connections are eliminated [28], [29], [61].

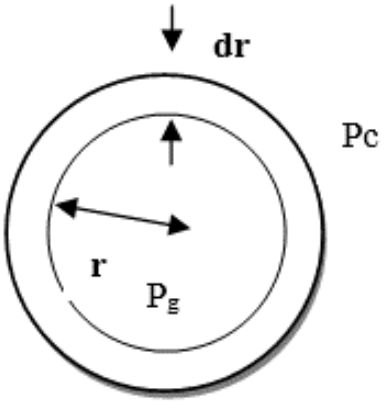

Figure 3.2: The pressure difference in pore produced by surface tension

Orts *et al.* (1993) studied the sintering behaviour of a ceramic and suggested a phenomenological model for the variation of the porous structure of the ceramic body with the sintering rate of ceramic materials as shown in equations (3.23) and (3.24).

$$If\ \ T \leq 1453\ K,$$

$$\frac{d\varepsilon}{dt} = -\frac{3\varepsilon}{4\eta_s}\left(P_c - P_g\right) \quad ------- \quad (3.23)$$

$$If\ 1453\ K < \ T \leq 1473\ K$$

$$\frac{d\varepsilon}{dt} = -\frac{3\varepsilon}{4\eta_s}(P_c) \ ------(3.24)$$

Capillary pressure (Pc) can be determined using equation (3.25)

$$P_c = \frac{2\gamma}{r} \ ------(3.25)$$

Surface tension (γ) is the tendency of liquid surfaces at rest to shrink into the minimum surface area possible in each of the pores of the ceramic tile body. Capillary pressure (*Pc*) is directly proportional to the surface tension [28], [61].

The chemical composition of the glassy phases calculated on the basis of bulk chemistry and mineralogical phases is presented in the tile body mix [29], [31], [32]. The effective viscosity of the system largely depends on the amount and viscosity of the liquid phase and the dissolution of quartz in the glassy phase. The viscosity of the glassy phase increases considerably as quartz dissolves into it [31], [60].

Glassy phase viscosity, surface tension, and radius of porous materials depend on material behaviour and sintering temperature. J. L. Amorós *et al*. (2007) studied variation in porous structure with firing temperature, and the average porous radius of the R1 sample was taken to represent the porous radius of this study [7]. C. Zanelli *et al.* (2004) investigated the viscosity variation of different porcelain materials with temperature, and the viscosity variation of the KB sample was employed in this study [54]. S. Conte *et al.* (2018) studied the viscosity and surface tension variation of different porcelain materials with temperature, and the average surface tension value related to this study was taken [35].

3.2.4.Kinetics Models for Physical and Mechanical Properties Variation during Sintering

a. Kinetics Model for Linear Shrinkage Variation

The change in the linear reduction of ceramic tiles (SL) during the sintering process was associated with sintering kinetics [62]-[64]. Orts *et al.* (1993) studied the effect of the firing temperature and time on the sintering kinetics of ceramic and suggested a

phenomenological model. Salem *et al.* (2010) were further studies models for variation in the linear retraction during the firing process. The sintering kinetics model for linear shrinkage in ceramic tiles was studied by M. Cargnin *et al.* (2015) [34]. The sintering behaviour and kinetics of ceramic tile depend on the sintering temperature (T), sintering time (t_s), and composition of ceramic tile.

Vitrification is the main mechanism for densification of ceramic tile, and Feldspar melting facilitates the creation of a viscous melt during the sintering process. The viscous melt formation rate depends on the sintering temperature and the material body composition. It can be determined using k'. The k' can be manipulated using Arrhenius-type equations (3.27).

$$K' = k_0 \exp\left(-\frac{E_A}{RT_s}\right) \quad ------(3.27)$$

Frequency factor (k_0) and activation energy (E_A) values depend on the composition of the ceramic tile body. The liquid phase formation ability is changed with the content of feldspar and quartz (CaO+MgO).

After the formation of the liquid phase, the viscous phase needs to flow throughout the body, filling and decreasing the porous structure. It varies with time and viscous phase properties. The change in the linear reduction (S_L) can be explained by equations (3.28).

$$S_L = \frac{L_i - L_f}{L_i} = K' t_s^n \quad ------(3.28)$$

t_s is the sintering time, and n is the sintering factor. The sintering time started at the glassy transition temperature of the body mix. The melted feldspar needs time to fill up the pores of the tile body, and the particles move closer together. While pore size and shape differ simultaneously, the body of the ceramic tile exhibits increasing shrinkage and decreasing porosity. The melted feldspar moving behaviour depends on the composition of the ceramic tile body, and the sintering factor (n) denotes ceramic tile body behaviour [4]-[13], [23], [24].

The linear reduction of ceramic tiles was calculated using equations (3.29) that can be obtained using equations (3.27) and (3.28). The equation (3.29) explains the linear reduction of ceramic tiles with a sintering profile. The sintering behaviour and kinetics of the ceramic tile influenced the sintering temperature and time.

$$S_L = k_0 \exp\left(-\frac{E_A}{RT}\right) t_s^n \quad ------(3.29)$$

The kinetic model of linear shrinkage variation of ceramic tile contains three main parameters, such as k_0 is frequency factor, E_A is activation energy, and n, a sintering factor. This value of these parameters is dependent on the composition of ceramic tile. A.J. Souza *et al.* (2013) investigated variation of linear shrinkage of different ceramic materials with firing temperature, and the MT3 sample composition is similar to this study sample composition [18]. So, the non-linear regression method was applied and the values of these parameters determined. The R^2 value was 0.9. Linear shrinkage model variables were selected based on the results of experiments conducted by A.J. Souza *et al.* (2013), which is similar to body composition using this study as presented in Table 4.2.

a.Kinetics Model for Modulus of Rupture Variation

In this study, the effect of temperature on Young's modulus is extremely important for the strength of ceramic tile during the sintering process. The thermal vibrations of atoms increase with temperature, and the lattice potential energy also increases. The potential energy curve's curvature will impact as a result, changing Young's modulus as well. The material will expand in volume when the temperature rises. Thus, it may be concluded that the atomic binding force and the material's volume are both involved in the change in Young's modulus with temperature. As a result, there is some complexity in a relationship between Young's modulus and sintering temperature.

According to references [65], [66], and [67], Young's modulus variation of ceramic with sintering temperature was investigated. Antoine Elimbi *et al.* (2014) investigated the variation in the Young's modulus of various ceramic samples with sintering temperature [68]. The ceramic samples were produced with Kaolin, ball clay, and feldspar, and Kaolin was a major component of each sample of the research. Both the SL5 sample and this research sample have the appropriate amounts of SiO_2, Al_2O_3, and RO (CaO+MgO). Consequently, the variation in Young's modulus with fired temperature of the ceramic body throughout the sintering process was evaluated using the SL5 sample. The effect of sintering temperature on the Young's modulus is shown in equation 3.30.

$$E_{fired} = 2.8580 \times 10^{-6} \times T_{s,max}^{3} - 8.61 \times 10^{-3} \times T_{s,max}^{2} + 8.62 \times T_{s,max} - 2{,}866.92 \quad (3.30)$$

Maximum breaking strength was calculated according to Parlevliet, P. P. *et al.* (2007) [69]. The equation (3.31) describes the variation of MOR of sintered ceramic tile.

$$\sigma_{max,fired} = E_{fired} \times k \times \frac{t}{2} \quad (3.31)$$

$\sigma_{max,fired}$ represents the maximum stress at the surface, thickness of the ceramic tile , t can be obtained from simulation results. k is the curvature. The k can be determine using below equation (3.32)

$$k = \frac{8h}{L^2 + 4h^2} \quad (3.32)$$

Deflection in the centre of the ceramic tile, h and the length of the ceramic tile L. The deflection in the centre of the ceramic tile is taken from "The TCNA Handbook for Ceramic, Glass and Stone Tile Installation," [70].

3.2.5.Initial and Boundary Conditions for Sintering Model

Table 3.1: INITIAL AND BOUNDARY CONDITIONS OF CFD MODEL

Properties	**Initial Condition**	**Boundary Condition (wall)**	**Reference**
Temperature	300K	Dynamic (Refer Figure 3.3)	
Pressure	1 atm	(fixed Value) 1 atm	[115]
Velocity	0 m/s	zeroGradient	[115]

The initial and boundary conditions of the CFD model are shown in Table 3.1, and these boundary conditions are applied to every surface of the tile (wall). Two phases are considered in this model, such as solid and gas phases. The initial temperatures for both phases are assumed to be 300 K for the entire tile and the boundaries of the ceramic tile

body at t = 0. The dynamic temperature boundary condition is applied in the CFD model to represent the sintering cycle, ensuring compliance with the experiment. Temperature variation in the boundaries of the ceramic tile body refers to the sintering cycle in Figure 3.3. The initial conditions of the pressure and velocity of the gas phase are assumed to be 1 atm and zero, respectively. In this research, the boundary conditions of the pressure for the gas phase are 1 atm. There is no pressure difference built up within the tile and furnace during the sintering process, and the boundary condition for the velocity is taken as zero gradient [115].

3.2.6.Importance of Dynamic Mesh for Sintering Model

Ceramic tile shrinkage behaviour varies with the sintering curve. Shrinkage depends on temperature, and a special variation of temperature exists in ceramic tile bodies during the sintering process. Then, the finite volume method is capable of modelling shrinkage during the sintering process of ceramic tiles. The shrinkage of each volume concerning temperature and time is examined. Hence, CFD modelling is capable of capturing the temporal and spatial variation in shrinkage within the ceramic tile. The volume of the domain is changed during the simulation process due to linear shrinkage. The ceramic tile sample generated 48000 cells; the number of cells in the mesh and the volume of each mesh changed with the sintering process. The properties of each mesh of the ceramic tile body vary with the sintering cycle and dynamic mesh concept to be applied for this model, which allows the mesh to change during a simulation [56], [117], [118]. After the simulation process, the model that was created with the addition of the dynamic mesh concept can produce more accurate results.

3.2.7.Theoretical Framework for Sintering Profile Optimization

It is preferable to conduct the sintering as fast as possible without causing damage to the sintered ceramic tile body in order to save time and energy. The maximum heating and cooling rates of the ceramic tile body are to be found, and the optimum sintering cycle can be found. During the heating, the interior of the ceramic tile remains at a lower temperature than the surface due to the low thermal conductivity of the ceramic tile body. The interior of the ceramic tile expands less than the surface. Therefore, the interior experiences tensile stress. The surface experiences tensile stress while the interior experiences compressive stress during the cooling process. The temperature

differences and thermal stresses change with time rapidly during the process of offset heating or cooling.

Thermal shock, or sudden temperature changes, and thermal fatigue, or frequent temperature cycling, are two conditions that cause ceramic tiles to fail. The ceramic body endures thermal stress as a result of a sudden change in the surrounding temperature, which creates a temperature gradient. When the thermal stress in that manner of stressing beyond the material's strength, failure occurs [66], [71].

The MOR of ceramic tile bodies varies with heating and is sensitive to both the heati ng rate and factors related to body composition. Quartz is the predominant material in the body mix, and the amount of thermal stress that appears is mostly determined by the behaviour of the quartz particles. When alpha quartz transforms into beta quartz, which occurs at 573 °C, there is a significant thermal expansion. Compared to the other ceramic tile body component, the quartz particle's thermal stress is greater. The thermal stress caused by quartz particles during the heating stage should be less than the MOR of the ceramic tile. Otherwise, the development of microcracks during the heating step has an impact on it [66], [102].

After heating, quartz particles and a glassy phase are present in ceramic tile. During the cooling stage, the transition of beta quartz to alpha quartz occurs around 573 °C. There is a significant thermal expansion for quartz particles than glassy phases [66], [102]. Therefore, the stress of the glassy phase of the ceramic tile body is smaller than the thermal stress created by the quartz particles. MOR of the glassy phase of ceramic tiles needs to be greater than the thermal stress resulting from quartz particles, and the cooling rate must be controlled. It assists in preventing microcracks in the body of the ceramic tile.

The thermal stress encountered by a material depends on the rate of heating or cooling and thermomechanical properties of the ceramic body. I. Stubna et al. (2013) suggested a kinetic model for fracture strength variation of Kaolin-base ceramics during the sintering process and MOR variation of ceramic tile during the heating and cooling process shown in equations (3.33) and (3.34) [66].

$$\sigma_{F\_C\_heating} = \frac{H_r \times A \times E_{C\_heating} \times \alpha_{C\_heating} \times C_{C\_heating} \times \rho \times r^2}{\lambda_{C\_heating}\left(1 - \mu_{C\_heating}\right)} \quad --(3.33)$$

$$\sigma_{F\_C\_cooling} = \frac{C_r \times A \times E_{C\_cooling} \times \alpha_{C\_cooling} \times C_{C\_cooling} \times \rho \times r^2}{\lambda_{C\_cooling}\left(1 - \mu_{C\_cooling}\right)} \quad ---(3.34)$$

Poisson ratio, thermal expansion, thermal conductivity, and Young's modulus of materials depend on material behaviour and sintering temperature. Ján Ondruška *et al.* (2021) investigated the variation in the thermophysical properties of ceramic samples with sintering temperature [59]. The ceramic samples were produced with Kaolin and natural zeolite, and Kaolin was a major component of each sample of the research. Both the KZ50 sample and this research sample have the appropriate amounts of SiO_2, Al_2O_3, and RO (CaO+MgO). Consequently, the variation in thermal conductivity and specific heat capacity of the ceramic tile throughout the heating stage of the sintering process were evaluated using the thermophysical properties of the KZ50 sample. The body composition of ceramic tile is not changed during the cooling stage. Thus, constant thermal conductivity and specific heat capacity values were used for the cooling stage, which appropriated the final value of thermal conductivity and specific heat capacity during the heating stage.

A. Vojtko *et al*. (2011) studied the variation Poisson ratio of Kaolin base ceramic materials with temperature in a porous structure with firing temperature, and this sample data was taken to represent the poison ration of this study during the heating stage [76]. T. Húlan *et al.* (2020) investigated the thermal expansion and young's modulus variation of different ceramic materials during the heating and cooling stages of the sintering process, and thermal expansion and Young's modulus variation of the Liepa sample were employed with this study [62].

The sudden change in the surrounding temperature generates a temperature gradient; thereby, the ceramic body experiences thermal stress. P. K. Panda *et al*. (2002) studied the generation of thermal stress inside ceramic bodies due to thermal shock. In this study, the thermal stress variation of quartz particles during the sintering process needs to be determined, and it can be calculated as shown in equations (3.35) and (3.36) [71].

$$\sigma_{thermal,heating} = \frac{E_{Q\_heating} \times \alpha_{Q\_heating} \times \Delta T}{\left(1 - \mu_{Q\_heating}\right)} \quad ----(3.35)$$

$$\sigma_{thermal,cooling} = \frac{E_{Q\_cooling} \times \alpha_{Q\_cooling} \times \Delta T}{\left(1 - \mu_{Q\_cooling}\right)} \quad ----(3.36)$$

According to Equation (3.37), the MOR of the ceramic body must be higher than the thermal stress of quartz particles during the heating process of ceramic tile. According to the references, the sintered ceramic body contained 70–75% of the glassy phase, including mullite, and 30–25% of quartz [23], [24], [80]. Thus, the characteristics of the ceramic tile boy altered with cooling in a manner that was nearly identical to the properties of the glassy phase. Ultimately, as the ceramic tile cools, the MOR of the tile body needs to be greater than the thermal stress of the quartz particle.

Heating stage

$$\sigma_{thermal,heating} < \sigma_{F\_C\_heating} \quad ------(3.37)$$

Cooling stage

$$\sigma_{thermal,cooling} < \sigma_{F\_C\_cooling} \quad ------(3.38)$$

If thermal stress is higher than the fracture strength, the tile is cracked during the sintering process. The heating and cooling rates can be optimized by considering equations (3.37) and (3.38).

There are six main reactions of the sintering process, such as the dihydroxylation of clay minerals, dolomite decompositions, the formation of mullite, the melting of feldspar, and glassy phase conversion to solid form [3], [4], [17]-[21]. These main reactions need to be completed properly within the sintering process to form a proper sintered ceramic tile body. So, this condition is also to be satisfied during the sintering process.

Table 3.2: PARAMETERS USED IN SIMULATION

Property		**Unit**	**Value**	**Ref.**
Thermal diffusion coefficients	K_D	W/(m.K)	0.8	[92]
Heat capacities of green ceramic	$C_{p,D}$	J/(kg.K)	938	[92]
Constant	k_0	1/s	100	[15]
	$\theta_{k,}$	K	3150	[15]
	θ_D	K	3800	[15]
Pre-exponential factor	A_i	1/s	$A_{Dwater\ evaporation}= 5.13\times10^{6}$	[100]
			$A_{Dihydroxylation}= 1.32\times10^{6}$	[93]
			$A_{Quatz\ inversion}= 115.7$	[94]
			$A_{Dolomite\ decomposition}= 1.045\times10^{6}$	[97]
			$A_{Sinel\ formation}= 5.22\times10^{25}$	[95]
			$A_{Mullite\ formation}= 8.202\times10^{22}$	[96]
			$A_{Glassy\ formation}= 0.71\times10^{21}$	[98]
			$A_{new\ crystalline\ formation}= 8.6\times10^{29}$	[98]
Activation energy	E_i	kJ /mol	$E_{Dwater\ evaporation}= 87.9$	[100]
			$E_{Dihydroxylation}= 140$	[93]
			$E_{Quatz\ inversion}= 181$	[94]
			$E_{Dolomite\ decomposition}= 184.69$	[97]
			$E_{Sinel\ formation}= 562$	[95]
			$E_{Mullite\ formation}= 631$	[96]
			$E_{Glassy\ formation}= 632$	[98]
			$E_{new\ crystalline\ formation} = 700$	[99]
Enthalphy	Δh_i	kJ/kg	$\Delta h_{Dihydroxylation}= 1158$	[40]
			$\Delta h_{Quatz\ inversion,\ heating}= 1.56$	[80]
			$\Delta h_{Quatz\ inversion,\ coolong}= 1.26$	[80]
			$\Delta h_{Dolomite\ decomposition}= 1646$	[40]
			$\Delta h_{Mullite\ formation}= -280$	[40]
			$\Delta h_{Glazzy\ phase}= 226$	[40]
			$\Delta h_{new\ crystalline\ formation} = -543$	[40]
Specific heat capacity, solid	$C_{p;s}$	J/(kg.K)	$1\times10^{-6}\ T^2-0.001T+1.1508$	[59]
Specific heat capacity, gas	$C_{p;g}$	J/kg	1000	
Thermal conductivity, solid	k_s	W/(m.K)	$7\times10^{-7}\ T^2-0.001T+0.5894$	[59]
Thermal conductivity, gas	k_g	J/(kg.K)	$2\times10^{-5}\ T+0.0013$	
Convection coefficient	h_{con}	kJ/kg	1.41	[58]
Emissivity	ε_m		0.85	[58]
Average collision diameter of air	σ_i	Å	3.617	[60]
Diffusion collision integral of air	Ω_i		0.7422	[60]
Glassy phase viscosity	$\prod_s$	MPa.s	-0.2T+248	[54]
Glassy phase surface tension	γ	mN/m	344	[35]
Radius of porous	r	μm	2.43	[7]
Sintering Factor	n		0.12	[18]
Frequency Factor	K_0	1/s	11461	[18]
Activation Energy Shrinkage	E_A	kJ/mol	154.372	[18]
Young's modulus of tile during	$E_{Cheating}$	N/m^2	$8.53\times10^{-8}T^3-1.05226\times10^{-}$	[68]
Young's modulus of tile during	$E_{Ccooling}$	N/m^2	$2.24\times10^{-8}T^3-1.57651\times10^{-}$	[68]

Young's modulus of quartz during heating	$E_{Qheating}$	N/m^2	$30^0C \leq T \leq 573^0C$ $-6.55\times10^{-7}T^3+0.00041T^2-0.0853T+89.90$ $573^0C < T \leq 1200^0C$ 95	[102]
Young's modulus of quartz during cooling	$E_{Qcooling}$			
Thermal Expansion of tile during heating (relative %)	$\alpha_{Cheating}$	1/K	$30^0C \leq T \leq 573^0C$ $1.49\times10^{-14}T^6-2.52\times10^{-11}T^5+1.62\times10^{-8}T^4-4.99\times10^{-6}T^3+0.0007T^2-0.0448T+0.808$ $573^0C < T \leq 900^0C$ 2.2 $900^0C < T \leq 1200^0C$ $7.33\times10^{-9}T^4-3.06\times10^{-5}T^3+0.04776T^2-33.0625T+8567.5$	[68]
Thermal Expansion of tile during cooling (relative%)	$\alpha_{Ccooling}$	1/K	$1200^0C \leq T \leq 30^0C$ $2.395\times10^{-17}T^6-5.068\times10^{-14}T^5+2.75\times10^{-11}T^4-3.495\times10^{-}$	[68]
Thermal Expansion of quartz during heating	$\alpha_{Qheating}$	1/K	$30^0C \leq T \leq 400^0C$ $-7.657\times10^{-17}T^5+8.33\times10^{-14}T^4-3.19\times10^{-11}T^3+5.20\times10^{-9}T^2-3.40\times10^{-7}T+1.63\times10^{-5}$ $400^0C < T \leq 550^0C$ $1.6\times10^{-11}T^3-2.12\times10^{-8}T^2+9.42\times10^{-6}T-0.00138$ $550^0C < T \leq 573^0C$ $5.33\times10^{-5}T-0.030319$ $573^0C < T \leq 1200^0C$ -0.000001	[102]
Thermal Expansion of quartz during cooling	$\alpha_{Qcooling}$			

Poisson's ratio of tile during heating	$\mu_{Cheating}$		$-2.26\times10^{-12}T^4+4.83\times10^{-9}T^3-3.256\times10^{-6}T^2+7.38\times10^{-}$	[76]
Poisson's ratio of tile during cooling	$\mu_{Ccooling}$		$1200^0C\geq T\geq900^0C$ $1.067\times10^{-7}T^3-3.56\times10^{-4}T^2+0.3967T-147.51$ $T\leq900^0C$ 0.45	[101]
Poisson's ratio of quartz during heating	$\mu_{Qheating}$		$27^0C<T\leq600^0C$ $-1.53\times10^{-11}T^4+1.36\times10^{-8}T^3-4.10\times10^{-6}T^2+2.938\times10^{-4}T+0.043409$ $T\geq600^0C$	[102]
Poisson's ratio of quartz during cooling	$\mu_{Qcooling}$			

3.3 Experimental Procedure

3.3.1.Raw Materials Selection and Body Composition Preparation

In general, quartz, feldspar, ball clay, and dolomite are the main raw materials used in the ceramic tile industry. The availability of quality ball clay for the tile manufacturing industry has decreased over the years in Sri Lanka, and the tile industry intends to substitute ball clay with another suitable clay. The ceramic tile industry depends heavily on the quality of clay minerals; new sources of clay have to be identified for the sustainability this industry. In this investigation, a brand-new natural Kaolin clay type was identified from a novel clay mine in Sri Lanka, which is entitled M2 Kaolin. M2 Kaolin was used as the main raw material for this study, and it was extracted from Meetiyagoda, a southern province of Sri Lanka. The area of Meetiyagoda is located between the coordinates 6°11′23″ N; 80°5′43″ E and 6°11′15″ N; 80°5′36″ E.

Two batches of M2 Kaolin samples with different particle size distributions were prepared using wet ball mill grinding process. Then M2 Kaolin was prepared in the form of dry powder. Further, M2 Kaolin was investigated for the ceramic tile industry as the main clay mineral with Feldspar, Dolomite, and Bentonite Clay [37], [38], [112]. The body mix, which is composed of 45% M2 Kaolin, 45% Feldspar, 5% Dolomite,

and 5% Bentonite Clay, was prepared using the raw components in dry powder form [37], [38], [40].

3.3.2.Determination of Moisture Content Variation for M2 Kaolin

The plug mill technique was used to prepare cylindrical shapes samples with 76 mm diameter and 65 mm height. The samples were dried in the oven at a constant temperature of 60 ^{o}C. Variation of moisture content of the samples with time was determined.

3.3.3.Ceramic Tile Preparation and Determination of Physical Properties

The ceramic tile samples were shaped by a powder pressing technique on a laboratory scale. The size of the tile was determined by the objectives of the study as well as the availability of machinery, tools, and laboratory-scale processing methods. Further, the muffle furnace configuration and the minimum length required for MOR testing are also taken into account for selection of ceramic tile size. The length, width, and thickness of the tile are 80 mm, 60 mm, and 10 mm, respectively, and the specific pressure applied was 400 Mpa. The tile samples were dried in an oven at a constant temperature of 80 ^{o}C. Variations of moisture content and dimension of the green ceramic samples with time were determined.

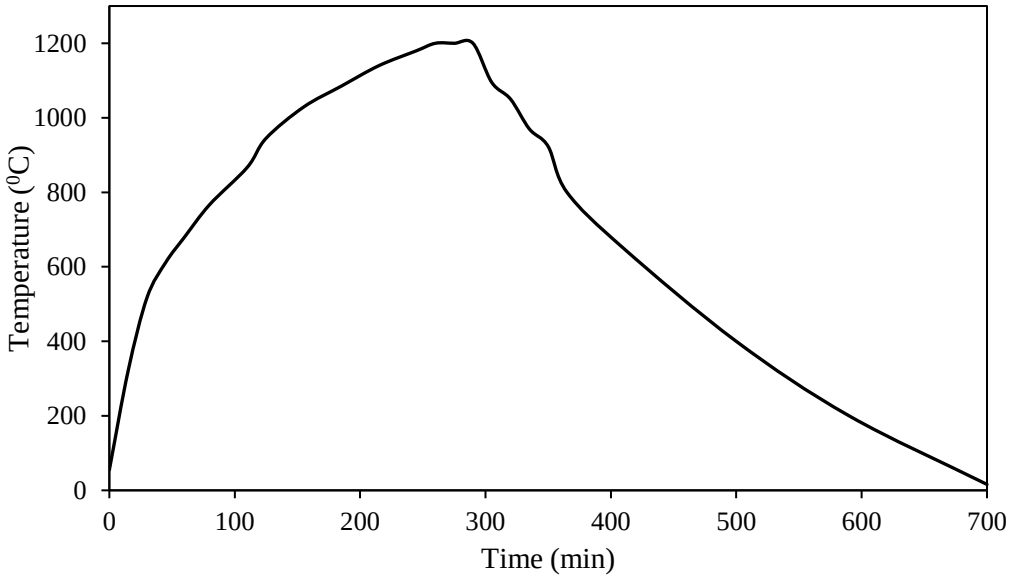

Figure 3.3: Sintering cycle of ceramic tiles-maximum sintering temperature 1200 ^{0}C

The dried tile samples were fired in a muffle furnace at 1100 ºC, 1050 ºC, 1080 ºC, and 1200 ºC. The sintering cycle at the maximum sintering temperature of 1200°C is shown in Figure 3.3.

Physical and mechanical characteristics of the sintered ceramic tiles, including water absorption, modulus of rupture (MOR), linear shrinkage, and volume reduction, were measured and gathered in this experiment. The volume reduction and linear shrinkage were calculated using equations (3.39) and (3.40).

$$S_l = \frac{L_i - L_f}{L_i} \times 100 \quad ------(3.39)$$

$$\Delta V = \frac{V_i - V_f}{V_i} \times 100 \quad ------(3.40)$$

The modulus of rupture (MOR) and water absorption of the samples were measured as per the ISO 13006 standard. Loss on ignition (LOI) and bulk density of the samples with sintering temperature were also determined.

3.3.4. Characterization of Raw Materials, Green and Sintered Ceramic Tiles

a. Chemical Structure Analysis of M2 Kaolin, Green Body Mix, and Sintered Ceramic Tile

X-ray diffraction techniques were used to analyze the structure of M2 Kaolin, green ceramic tile body mix, and sintered ceramic tile using the 'Rigaku Ultima IV' X-ray diffractometer (CuKα1:1.5406 Å).

b. Chemical Elements Analysis of M2 Kaolin and Green Body Mix

The quantities of SiO_2, Al_2O_3, Fe_2O_3, CaO, MgO, Na_2O, K_2O, MnO, and ignition ingredients in the M2 Kaolin and green ceramic tile body mix were measured by wet chemical analysis.

- A mixture consisting of 0.5 g of a finely ground sample and 2.5 g of Na_2CO_3 was added together, and the mixer was heated up in a laboratory furnace at 950 ◦C. The melted bulk and dilute hydrochloric acid blended. The SiO_2 precipitation was extracted on filter paper after the solution completely evaporated. The SiO_2 precipitate was determined after burning the filter paper. After that, hydrofluoric acid was applied to

the precipitated SiO_2. The percentage of SiO_2 is computed using the weight loss after hydrofluoric acid treatment.

- 0.5 g of finely milled sample material was treated with 15 ml of HF and 5 ml of HNO_3. The bulk solution was then entirely dissolved by heating it on a hot plate. Then the extra HF is evaporated. 250 ml of transparent solution was prepared using 2 % nitric acid. An atomic absorption spectrophotometer (GBC 33AA) was utilised to examine $Al2O_3$, Fe_2O_3, CaO, MgO, Na_2O, K_2O and MnO, while a UV–visible spectrometer was utilised to identify P and Ti.
- In a platinum crucible, 1 g of finely ground material was burnt up to 950 ◦C and the amount of mass loss due to ignition (LOI)% was calculated.

c. Particle Size Analysis of Raw Materials and Green Body Mix

Particle size testing was conducted for raw materials and green body mix using the 'Chengdu Jingxin Powder Analyse Instrument Co., (JL-1177)' Laser Particle Size analyser.

d. Thermal Behaviour Analysis of Raw Materials and Green Body Mix

Differential thermal analysis and thermogravimetric analysis were utilized to examine the thermal response of M2 Kaolin and the green ceramic tile body mix. The instrument that was used for this analysis was the "(SDT Q-600, USA)" under a nitrogen environment, heating at a rate of 10 ^{0}C per minute from ambient temperature to 1100 ^{0}C.

e. Chemical Elements, Microstructure and Dispersion Analysis of Sintered Ceramic

A scanning electron microscopy analyser was employed for structural characterisation of the sintered ceramic samples to determine the chemical elements, microstructure, dispersion, morphology, and grain size. The untreated sample was analysed by scanning electron microscopy (EVO 18, Germany) and an energy dispersive X-ray (EDX) analyser (EVO 18, Germany).

CHAPTER 4

4. EXPERIMENTS RESULTS

4.1 Characterization Results of Raw Materials, Green and Sintered Ceramic Tiles

4.1.1 X-ray Diffraction Analysis of M2 Kaolin, Green Body Mix, and Sintered Ceramic Tile

Figure 4.1 and Figure 4.2 represent the X-ray diffraction data of the M2 kaolin and green ceramic tile body mix. The XRD analysis of M2 Kaolin revealed that the two phases are quartz alpha and kaolinite [$Al_2Si_2O_5(OH)_4$]. The primary framework of the ceramic tile body is built from quartz, and its plasticity is enhanced by kaolinite. Consequently, the utilisation of M2 Kaolin as a raw material may provide greater advantages for ceramic tile bodies within the industry.

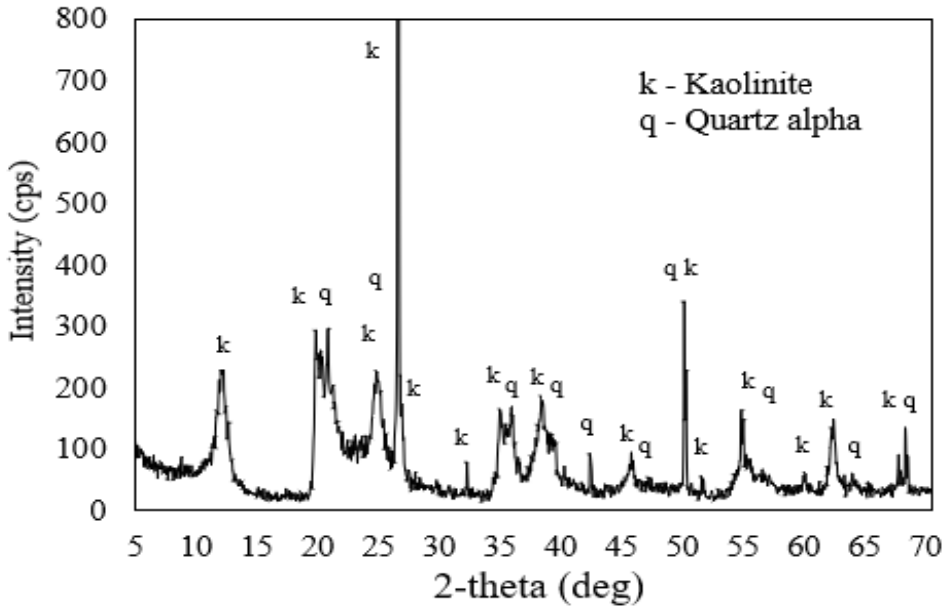

Figure 4.1: X-ray diffraction of the M2 Kaolin.

According to XRD analysis, the green ceramic tile body mix contains quartz, kaolinite, feldspar, and dolomite. The main component of the body mix is 20% quartz, 30% clay with kaolinite and bentonite, 45% feldspar, and 5% dolomite. The X-ray diffraction patterns of the sintered body mix at 1100 °C, 1150 °C, 1200 °C, and 1180 °C are

presented in Figures 4.3, 4.4, 4.5 and, 4.6. An analysis of the XRD revealed that mullite and quartz phases in the sintered body mix. There is no discernible difference in the quantity of quartz in the sintered products, and mullite is the result of kaolinite conversion. Quartz contains green body mix in alpha form, and it converts to beta form during the sintering process [78], [79]. The proportion of quartz, mullite, and glassy phases in the sintered ceramic tiles varies with temperature [4], [78], [79]. Feldspar phases were identified by XRD in the sintered ceramic tiles at 1100 °C and 1150 °C. The ceramic body vitrification process and formation of glassy phase occur after 1100 °C, and the amount of solid feldspar in the ceramic tile body decreases with sintering temperature [29]-[31].

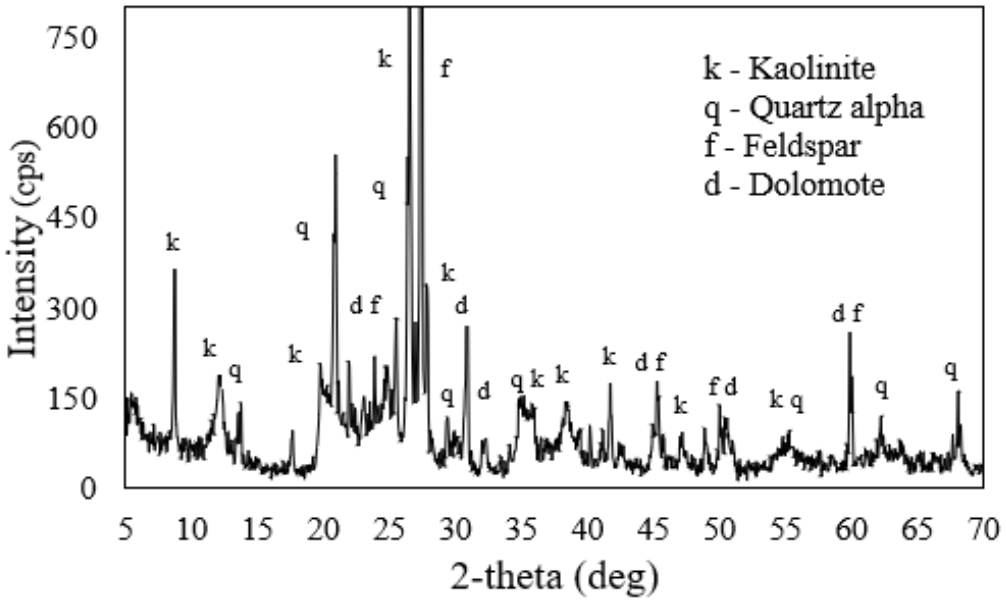

Figure 4.2: X-ray diffraction of the green ceramic tile body mix

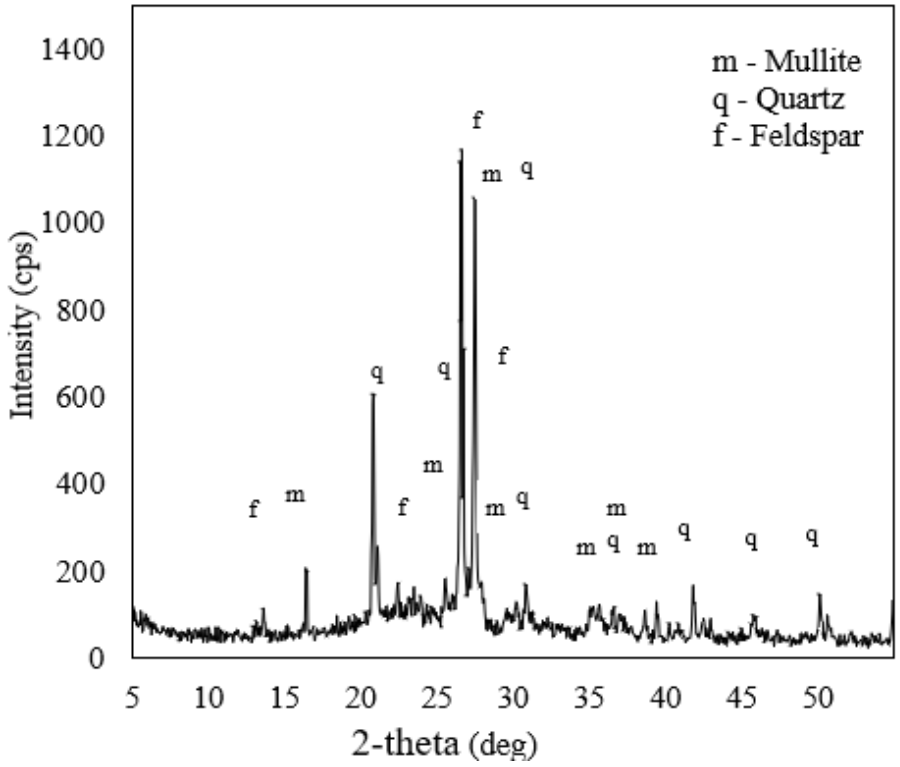

Figure 4.3: X-ray diffraction of the ceramic tile bodies sintered at 1100 ^{0}C

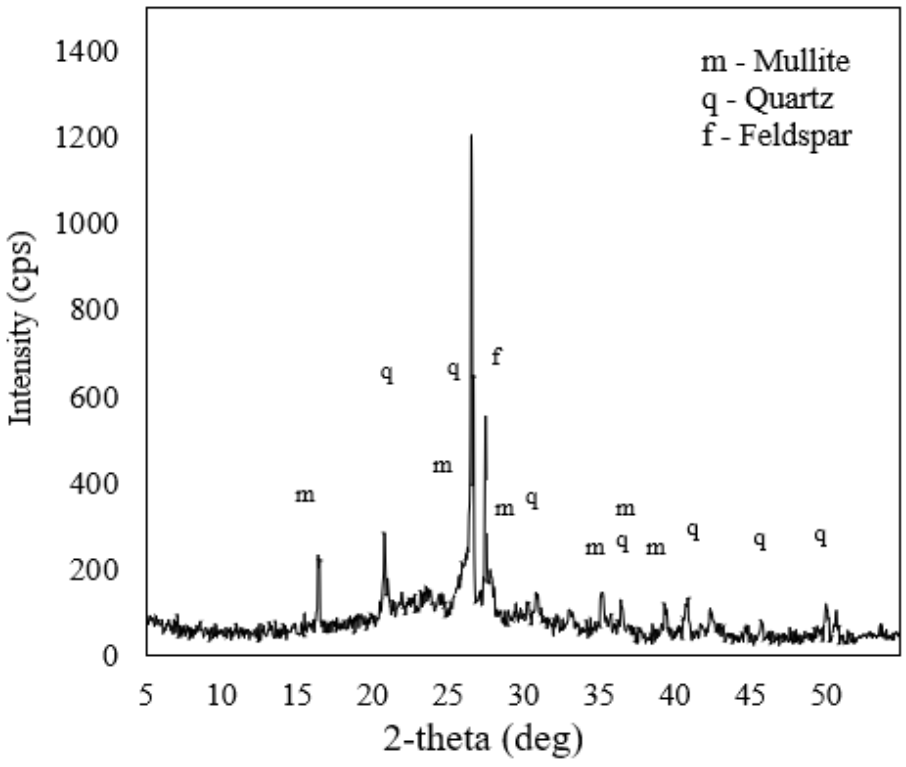

Figure 4.4: X-ray diffraction of the ceramic tile bodies sintered at 1150 ^{0}C

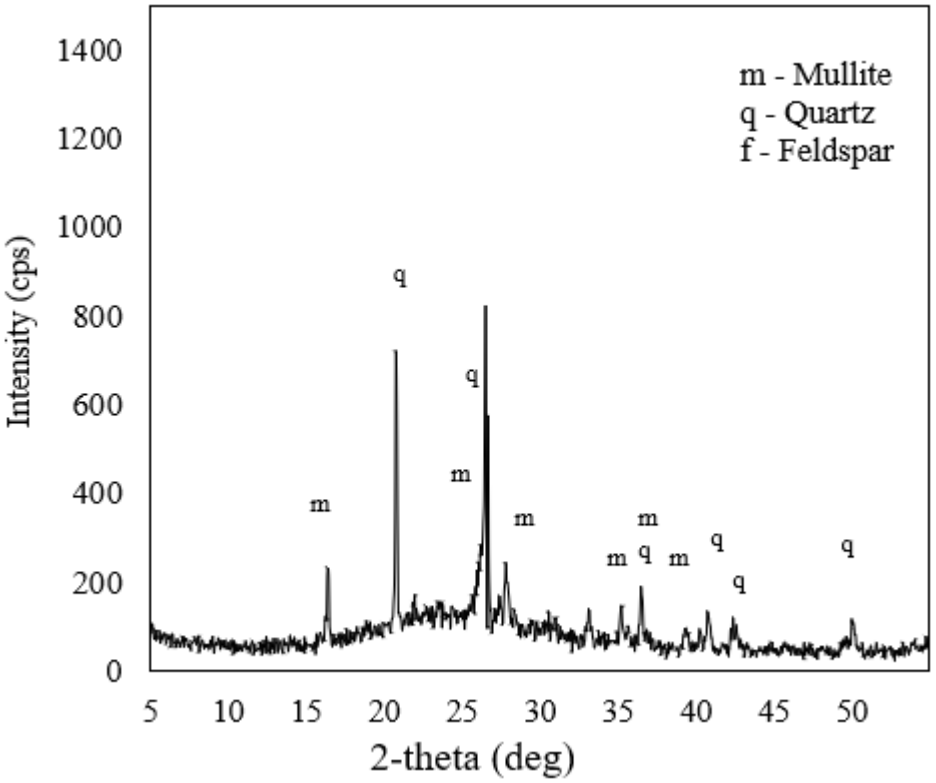

Figure 4.5: X-ray diffraction of the ceramic tile bodies sintered at 1200 ^{0}C

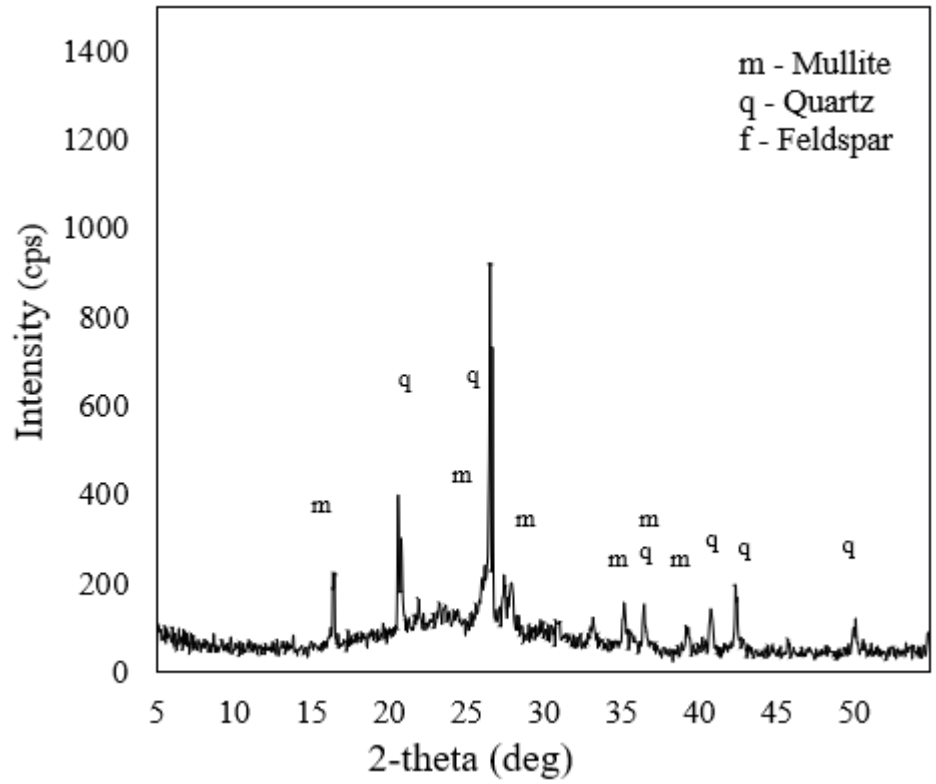

Figure 4.6: X-ray diffraction of the ceramic tile bodies sintered at 1180 ^{0}C

4.1.2 Chemical Analysis of M2 Kaolin and Green Body Mix

Table 4.1 represents the quantities of SiO_2, Al_2O_3, Fe_2O_3, CaO, MgO, Na_2O, K_2O, MnO, and mass loss due to ignition in the M2 Kaolin and green ceramic tile body mix. Table 4.1 shows that the chemical analysis M2 kaolin has an alumina and silica amount of 27.27% and 56.78%, respectively, and a loss on ignition of 13.47%. According to the XRD analysis of M2 Kaolin, it contains quartz and kaolinite structures, and these both structures contain Si and Al. Chemical analysis results were given for a combination of both phases of M2 Kaolin. The chemical analysis of green ceramic tile body mix contains 4.53% of K_2O, and it confirmed that the K-feldspar is used for body mix preparation. The total R_2O (K_2O + Na_2O) contained in the green ceramic tile body mix is 5.59%. Dolomite was added to the body mix, and the total RO (CaO + MgO) contained in the body mix was 3.75%.

Table 4.1: CHEMICAL COMPOSITION OF THE M2 KAOLIN AND GREEN CERAMIC TILE BODY MIX

Constituents	**Contents % w/w**	
	M2 Kaolin	**Body Mix**
SiO_2	56.78	56.20
Al_2O_3	27.27	22.30
Fe_2O_3	0.84	0.83
K_2O	0.78	4.53
Na_2O	0.25	1.06
MgO	0.16	1.63
CaO	0.07	2.12
TiO_2	0.31	0.70
MnO	0.01	0.01
P_2O_5	0.01	0.39
LOI	13.47	10.14

4.1.3Particle Size Analysis of M2 Kaolin (Plug Milled Samples)

Figures 4.7 and 4.8 represent the size distribution of particles in relation to particle diameter vs. percentage of total particle volume percentage of M2 kaolin samples, as evaluated by dimensions of low-angle laser light scattering (LALLS) technique. The average particle size (D50) of the kaolin clay was 4.07 µm and 3.57 µm, respectively. 90% of the particles in batches 1 and 2 are less than 52.56 µm and 32.42 µm, respectively.

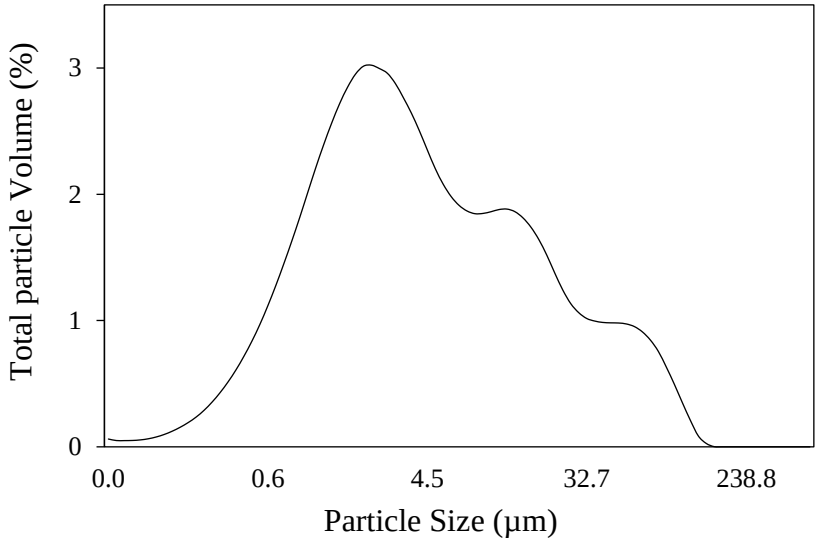

Figure 4.7: Particle size distribution of M2 Kaolin -Batch 01

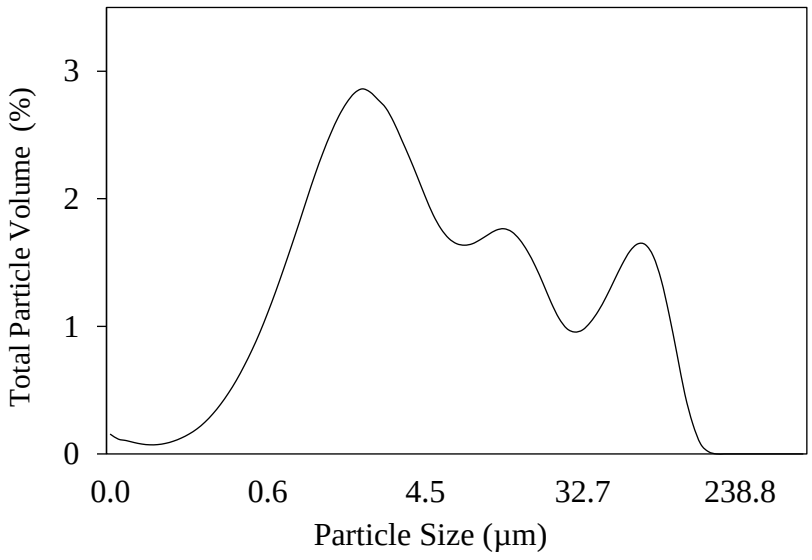

Figure 4.8: Particle size distribution of M2 Kaolin -Batch 02

4.1.4 Particle Size Analysis of Raw Materials and Green Body Mix of Ceramic Tile

Figure 4.9 exhibits the variation of particle size of M2 Kaolin with particle volume percentage. M2 Kaolin particles spread between 0.05 and 16.32 µm, and the average particle size is 0.971 µm. Table 4.2 displays the average particle sizes of feldspar, dolomite, bentonite, M2 Kaolin, and body mix. The average size of the green body mix particle was 24.012 µm. M2 Kaolin consists of finer particles than other raw material particle sizes, while dolomite and feldspar have larger particles. The appropriate particle distribution within the ceramic body mix can be observed. Therefore, the body mix provides the tile body with an exceptional compact density of 1.8 g/cm^3 during the pressing process [3], [5], [6].

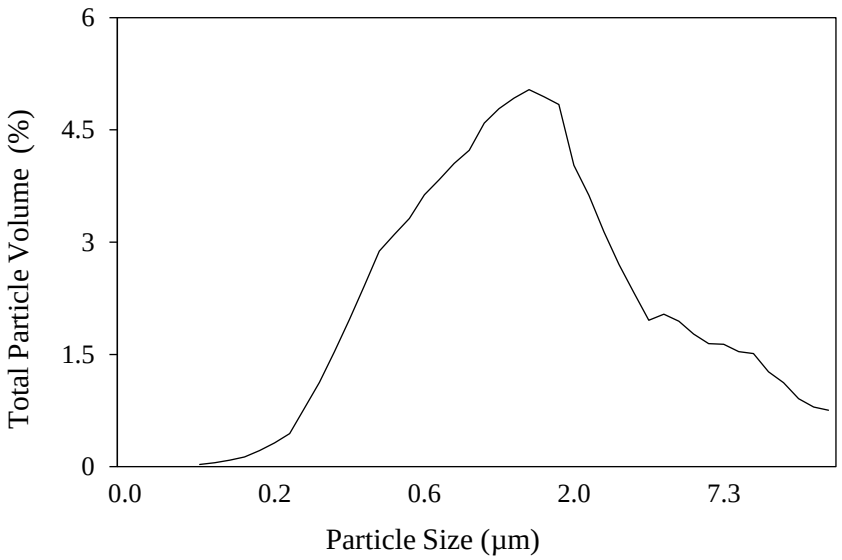

Figure 4.9: Particle size distribution of M2 Kaolin

Table 4.2: AVERAGE PARTICLE SIZE OF RAW MATERIALS AND GREEN CERAMIC TILE BODY MIX

Type of Raw	Particle Size (µm)		
	Average (D3)	**Average (D50)**	**Average (D90)**
Body Mix	0.239	24.012	63.340
Bentonite	0.226	2.444	17.758
M2 Kaolin	0.176	0.971	5.278
Feldspar	0.295	28.208	65.458
Dolomite	0.301	29.121	65.590

4.1.5 Differential Thermal and Thermogravimetric Analysis of Raw Materials and Green Body Mix

TGA and DTA curves for M2 Kaolin and green body mix appear in Figures 4.10 and 4.11, respectively. When the sample is heated to 1100 ^{0}C, the differential thermal pattern reveals a variety of reaction peaks, both endothermic and exothermic. The elimination of physically incorporated water from the M2 Kaolin and green body mix is the result of the first endothermic peak, which appears in the range of 70 and 100 ^{0}C. The process of combustion of biomass occurred while it was being heated, and it appeared to have an exothermic peak between 200 and 450 °C [110], [111]. The dihydroxylation process completely converted Kaolin into metakaolin, as evidenced by the endothermic peak, which appeared between the temperatures of 490 and 600 ^{0}C [7], [11], [78]-[85]. The conversion from α-quartz to β-quartz was shown by the endothermic peak in the temperatures of 573 ^{0}C, appropriately [7], [11], [86]. Metakaolin is converted to spinel, which accounts for the exothermic peak in the 980–1000 ^{0}C range [7], [11], [78]-[85].

According to Figure 4.8, the decomposition of calcium and magnesium carbonate in the body mix leads the endothermic peak to occur between 720-750 ^{0}C and 910-940 ^{0}C [87]-[90]. The mass elimination rate of M2 Kaolin and green body mix at temperatures

of 30–1000 ^{0}C is represented in Figures 4.10 and 4.11, and it is around 11.3% and 10.1%, respectively.

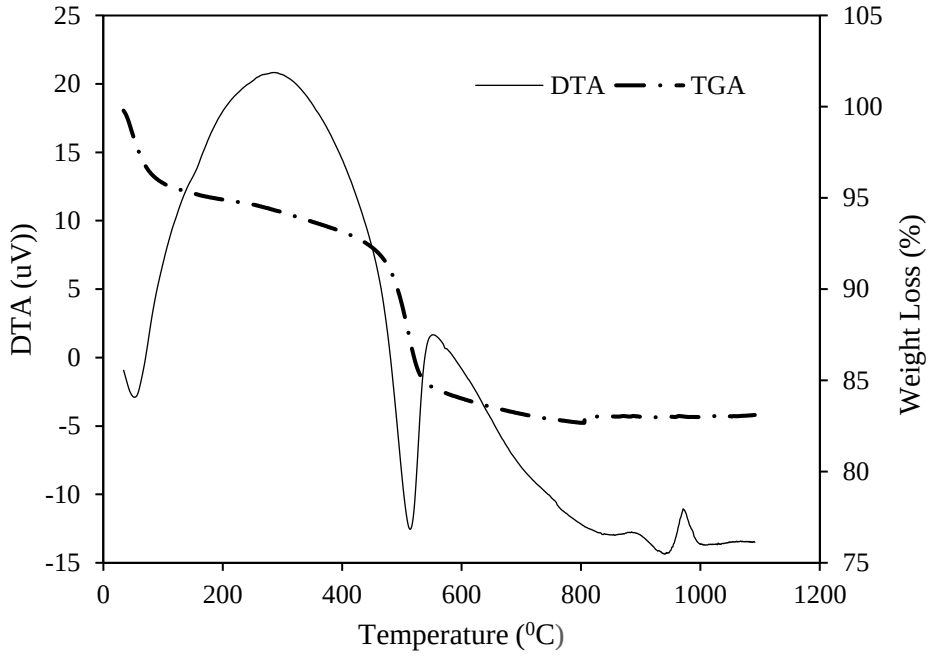

Figure 4.10: DTA and TGA curves for M2 kaolin

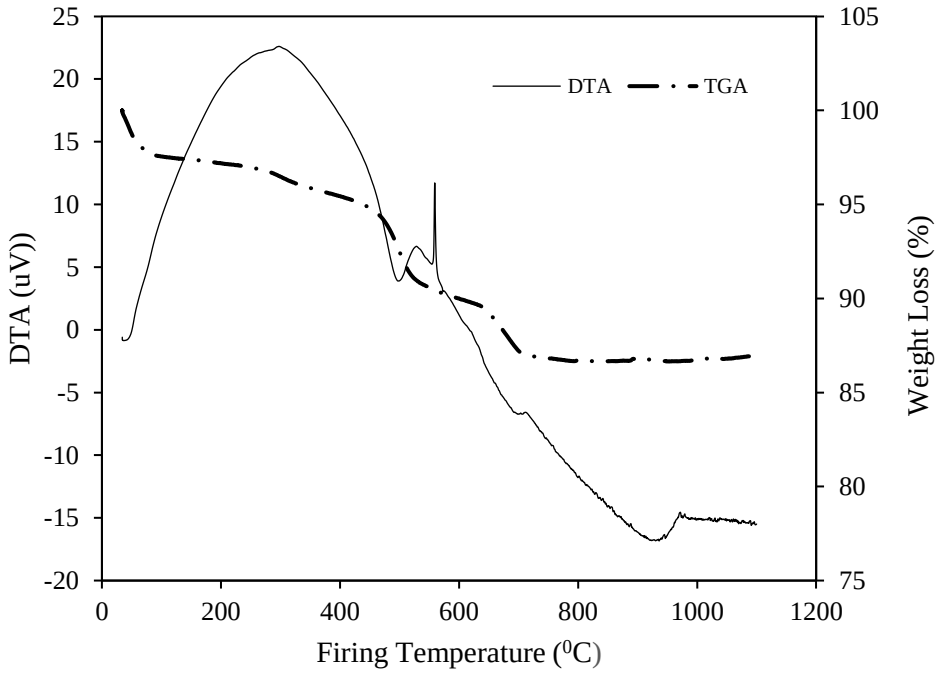

Figure 4.11: DTA and TGA curves for green ceramic tile body mix

4.1.6 Scanning Electron Microscopy and Energy Dispersive X-ray Spectroscopy Analysis of Sintered Ceramic

Figures 4.12 and 4.13 show SEM images of sintered ceramic tiles at 1200 °C. The ceramic samples depict the ordinary characteristics of a well-sintered ceramic tile body, and the existence of numerous areas, including mullite, quartz, and the glassy phase, is evident [4], [79], [89]. The XRD analysis also confirmed that the sintered ceramic tile has mullite, quartz, and glassy phases. The EDS data was used to analysis position of quartz and mullite particle in the SEM analysis.

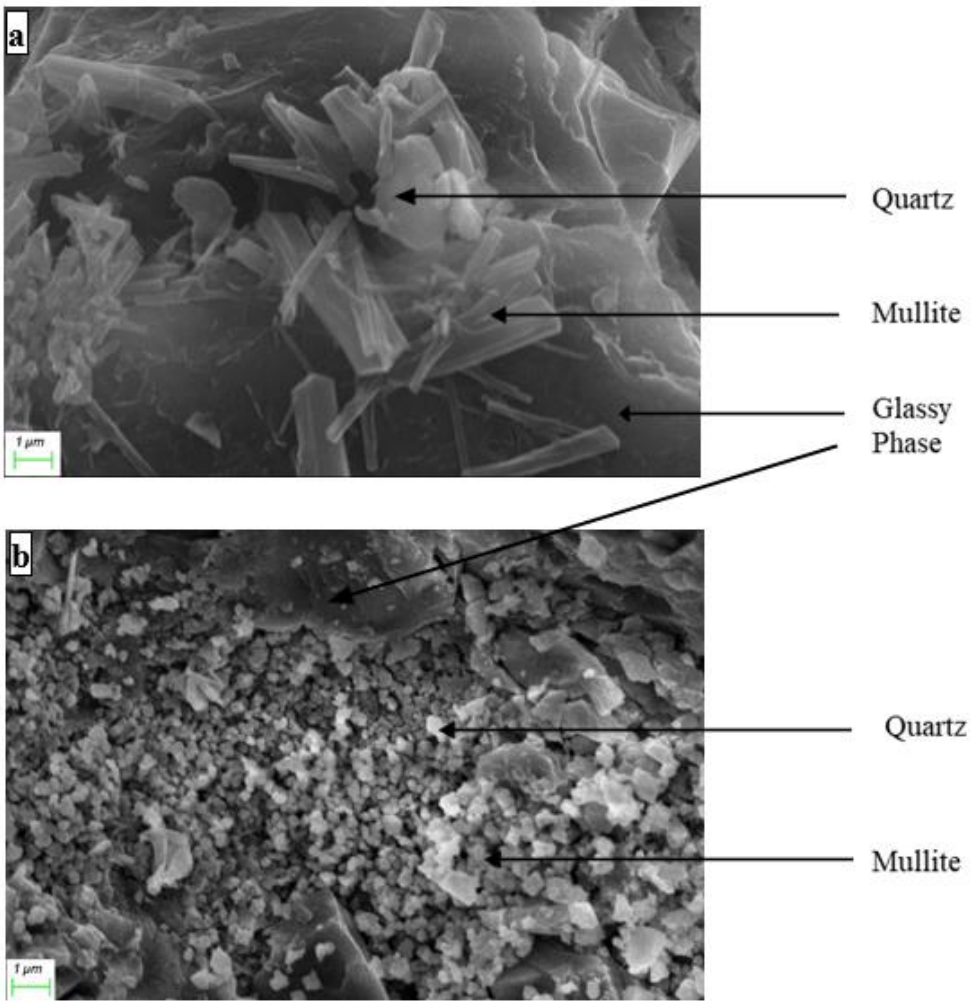

Figure 4.12: SEM images at 15000 x magnification, sintered ceramic tile at 1200 ^{0}C- a and b are two places in tile body

The EDS data is given elemental analysis for each phase. The ratio of Si and O was determined using EDS analysis. If it is similar to the quartz composition, that point is

identified as the quartz phase. A similar method was applied for the identification of mullite phase also, and the Al, Si, H, and O element ratios were compared with EDS data results. The results of Table 4.3 and 4.4 revealed that the mullite phase was rich in silicon (Si), aluminium (Al), and oxygen (O), and the quartz phase observed typically silicon (Si) and oxygen (O). In this research, the exact elements ratio was difficult to obtained due the mix of glassy phase. Therefore, the location of the mullite and quartz particles was determined by integrating the study of EDS data, SEM data, and references. The SEM and EDS analyses confirmed that the original raw materials have undergone all of the chemical and physical transformations during the sintering process.

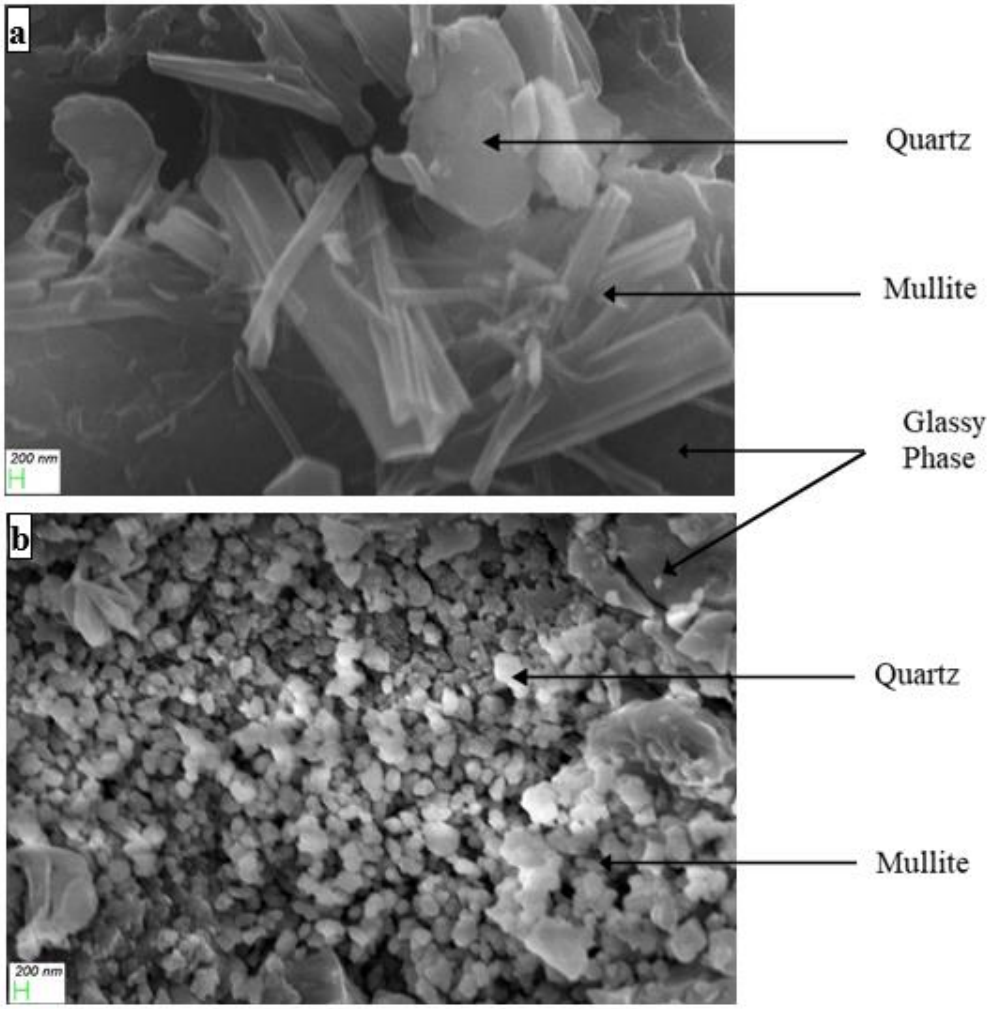

Figure 4.13: SEM images at 25000 x magnification, sintered ceramic tile at 1200 ^{0}C- a and b are two places in tile body

Table 4.3: EDX OF MULLITE PHASE OF SINTERED CERAMIC TILE - MAXIMUM SINTERING TEMPERATURE AT 1200 ^{0}C

Element	Weight (%)	Atomic (%)
O	43.75	58.32
Na	1.66	1.54
Mg	1.48	1.30
Al	13.40	10.60
Si	30.98	23.53
K	4.83	2.64
Ca	3.89	2.07

Table 4.4: EDX OF QUARTZ PHASE OF SINTERED CERAMIC TILE - MAXIMUM SINTERING TEMPERATURE AT 1200 ^{0}C

Element	Weight (%)	Atomic (%)
O	66.86	74.76
Na	1.97	1.53
Mg	1.69	1.25
Al	7.15	4.74
Si	16.74	10.66
K	1.22	0.56

4.2Determination of Moisture Variation of M2 Kaolin

Moisture variation of the M2 Kaolin samples (plug milled) with time was determined, and the critical moisture content of the M2 Kaolin was 1.50%. Total moisture content of each batch of samples with time was plotted as shown in Figure 4.14. Drying time and rate of two batches of samples were analyzed. Accordingly, the drying rate of batch 01 is higher than batch 02 up to fifteen (15) hours of drying time. The bulk density of two batches of samples was measured as 1950kg/m3 and 2000kg/m3 respectively. Drying time and rate of the M2 Kaolin were varied with bulk density (ρ) of samples

because bulk density (ρ) varies with particle size distribution and it affects the microstructure of the samples.

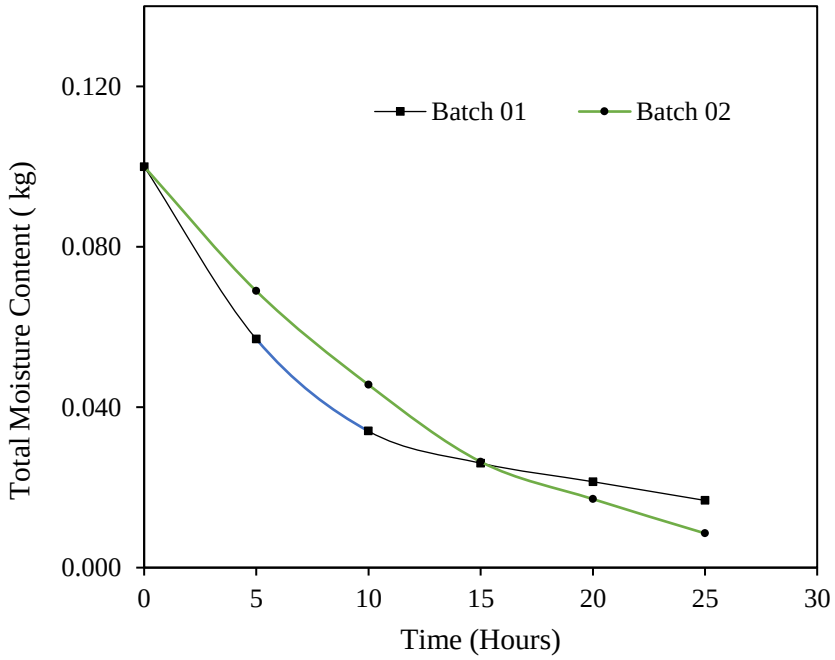

Figure 4.14: Comparison of total moisture content variation of M2 Kaolin sample

4.3 Determination of Physical and Mechanical Properties of Ceramic Tiles

Figures 4.15 and 4.16 show a variation in linear shrinkage and moisture content during the drying process. The moisture content of the ceramic tile body decreases with time, and the drying rate also decreases with time. The maximum liner shrinkage of the green ceramic tiles is 0.75%.

Variation in water absorption percentage and MOR values for sintered ceramic tiles with sintering temperature is shown in Figure 4.17. The MOR of ceramic tile is increased, and the water absorption is decreased with sintering temperature. The highest MOR is 20.7 N/mm^2 at 1200 ^{0}C and comparatively, the lowest value of water absorption is 3.5%. Figure 4.18 shows variation of linear shrinkage and volume reduction of ceramic tile with sintering temperature. The volume reduction and linear shrinkage of sintered ceramic tiles increased with sintering temperature. The maximum volume reduction and linear shrinkage of ceramic tiles are 7.5% and 24.0 %, respectively, which is given temperature at 1200 ^{0}C. The packing density of ceramic

tile varied with sintering temperature, as shown in Figure 4.19. The maximum value of packing density is 2.0 g/cm^3 which is given at a temperature of 1200 ^{0}C

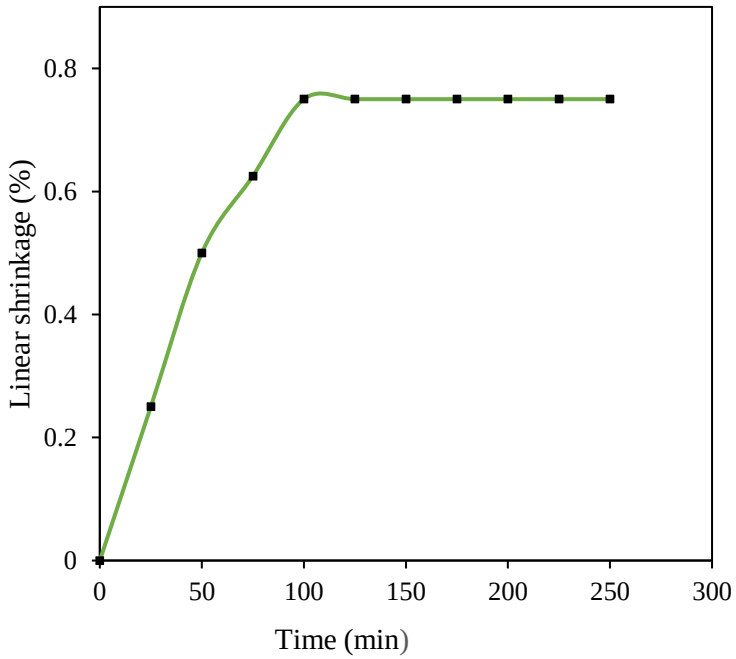

Figure 4.15: Linear Shrinkage variation of green ceramic tile sample

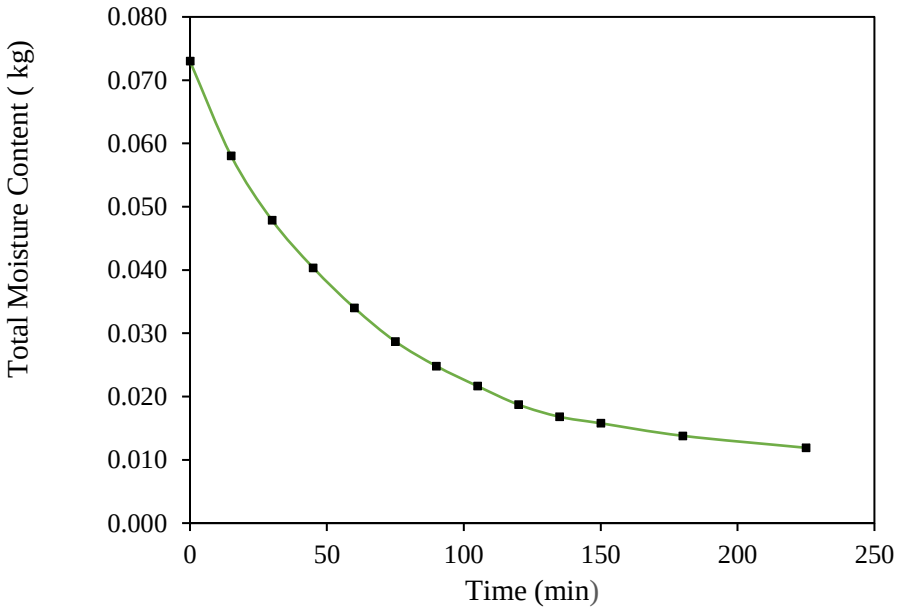

Figure 4.16: Experiment total moisture content variation of green ceramic tile sample

During the sintering process, the particles fuse together, and pores between the particles of the ceramic body become more nearly spherical, and the porosity of the ceramic tile body decreases simultaneously [61]. Wetting and spreading activities during liquid phase sintering influence the microstructure of the ceramic body by modifying the pore shape.

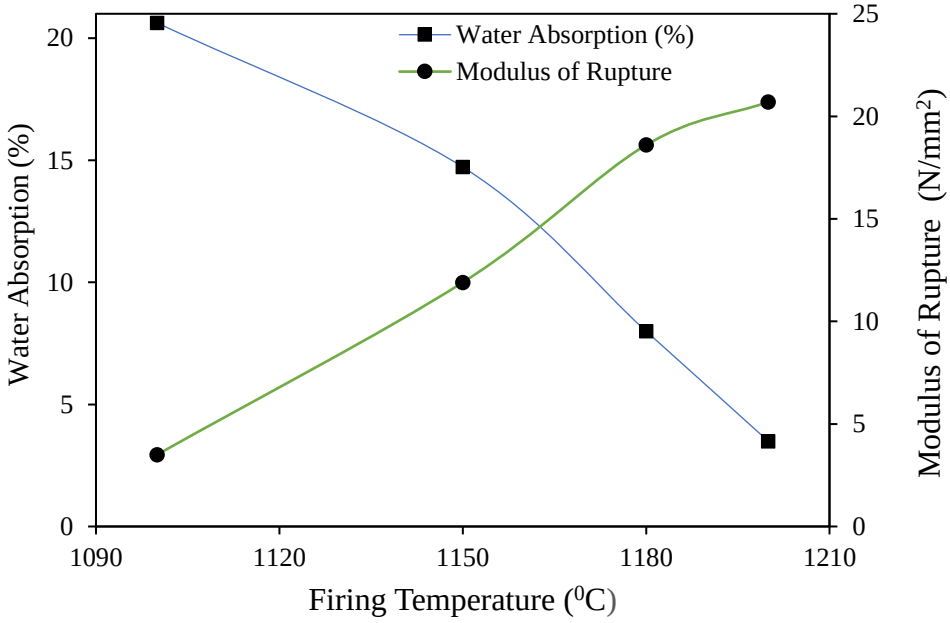

Figure 4.17: Water absorption and MOR variation of ceramic tiles with different sintering temperature

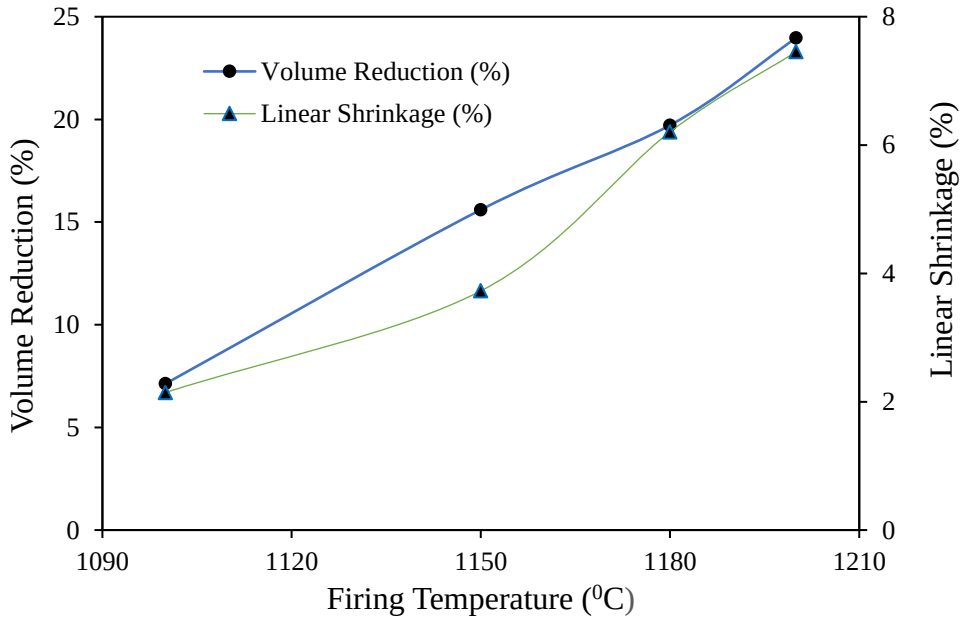

Figure 4.18: Volume reduction and linear shrinkage variation of ceramic tiles with different sintering temperature

The formation of viscous melt in the sintering process is accomplished by feldspar melting. During firing, at temperatures of about 1100 °C, an important quantity of liquid phase begins to form, surrounding the particles and producing a process-driving capillary pressure (Pc) at the contact points [33], [51], [52]. Pores of the tile body are filled with melted feldspar, and the capillary pressure brings the particles closer together, increasing shrinkage and lowering porosity while simultaneously altering pore size and shape. Raising the temperature increases the quantity of liquid phase and lowers porosity. In intermediate states, at around 1180 ^{0}C –1200 ^{0}C, pores start closing as interpore connections are eliminated [52], [60]. As a result, while water absorption reduced with sintering temperature, the MOR, packing density, linear shrinkage, and volume reduction increased concurrently. The best physical properties of tiles can be obtained by controlling the formation of a vitreous phase of the tile body. Therefore, sintering temperature is a critical factor controlling the formation of a vitreous phase.

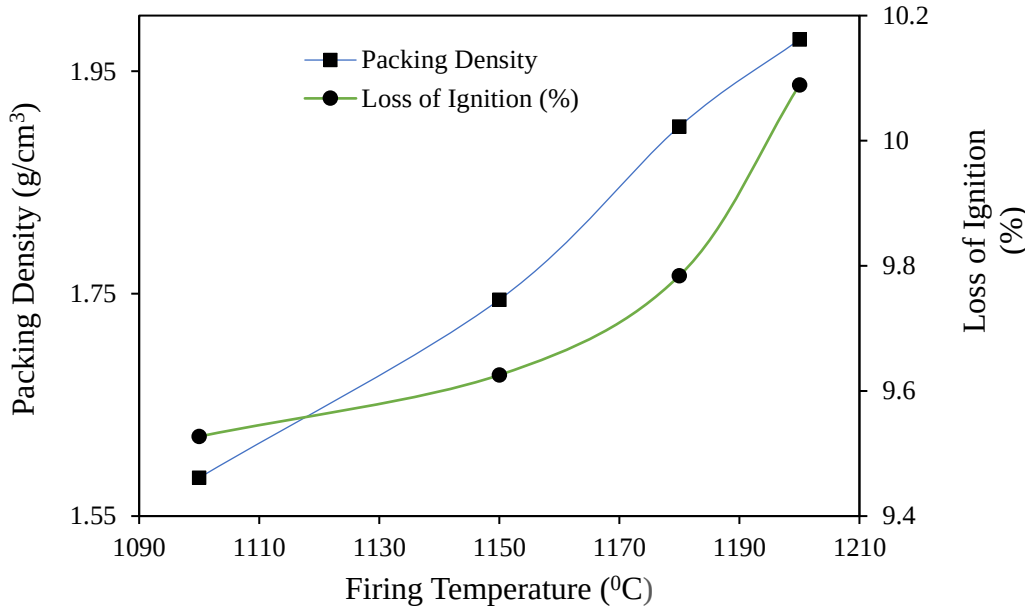

Figure 4.19: Packing density and loss of ignition variation of ceramic tiles with different sintering temperature

Figure 4.19 shows that the loss on ignition of ceramic tiles does not significantly vary with sintering temperature, with a minor fluctuation of 0.6% at temperatures between 1100 and 1200 °C. Mass variation-related physical and chemical transformations of ceramic tiles occur below 1000 °C. Therefore, the significant LOI variation can't be observed after 1000 °C.

CHAPTER 5

5. MODEL VALIDATION

5.1Drying Model Validation

5.1.1M2 Kaolin Sample Drying Model Validation

The D_0 value of each batch, which was explained in equation (3.2) formula, was determined using experiment bulk densities and equation (2.4) formula. The values of a_D and b_D constants of equation (2.4) formula were taken from reference [15]. Calculated D_0 values were shown in Table 5.1, and the effective diffusion coefficient of the M2 Kaolin sample is reduced with bulk density. The diffusion coefficient of moisture is a highly critical factor for the drying curve of the ceramic body, and the accuracy of the diffusion coefficient has to be maintained properly. Therefore, a mathematical model was developed using the effective diffusion coefficient that was determined using calculated D_0 values as shown in Table 5.1, and Θ_D was taken from the reference [15], which was related to the bulk density and temperature.

Table 5.1: D_0 VALUE VARIATION OF M2 KAOLIN SAMPLE WITH BULK DENSITY

Batch No	**Bulk Density (kg/m^3)**	**D_0 (10^{-6})**
01	1950	369.23
02	2000	309.26

To be certain that the outcomes of the drying model are unaffected by cell size, the mesh was improved and evaluated using the drying model. Simulation results developed by the drying CFD model and experiments results of total moisture content variation of M2 Kaolin sample with time plotted as shown in Figures 5.1 and 5.2. According to the model, the total moisture content variation of the samples was reduced with time, and the drying time of batch 01 is lower than batch 02. Simulation results developed by the model were compared and analysed with data obtained by

experiments conducted using M2 Kaolin. The model results were validated and comply with experiments results. R^2 value was 0.9 for both batches.

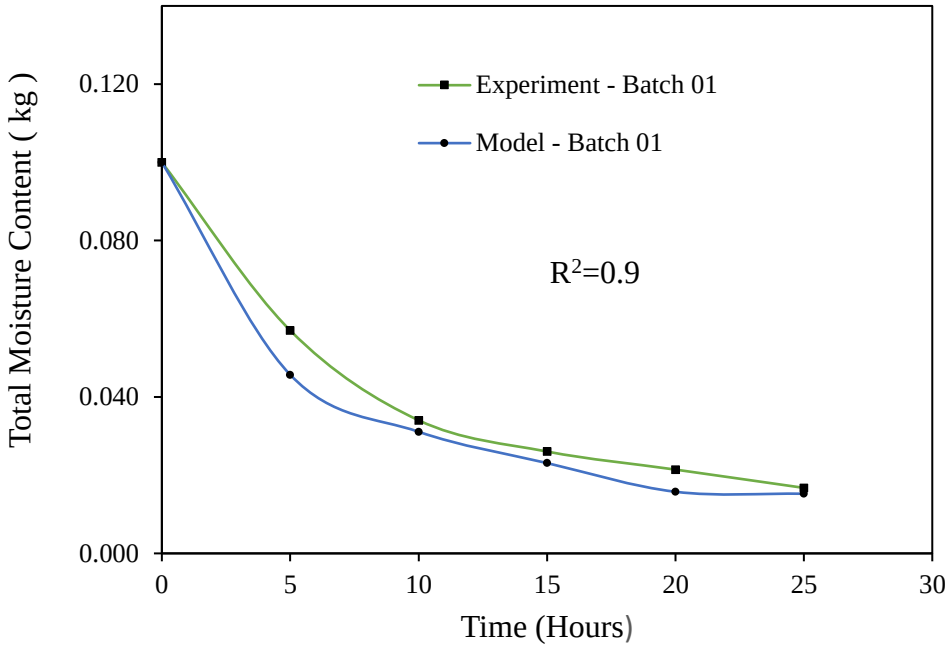

Figure 5.1: Comparison of model with experiment total moisture content variation of M2 Kaolin sample - Batch 01

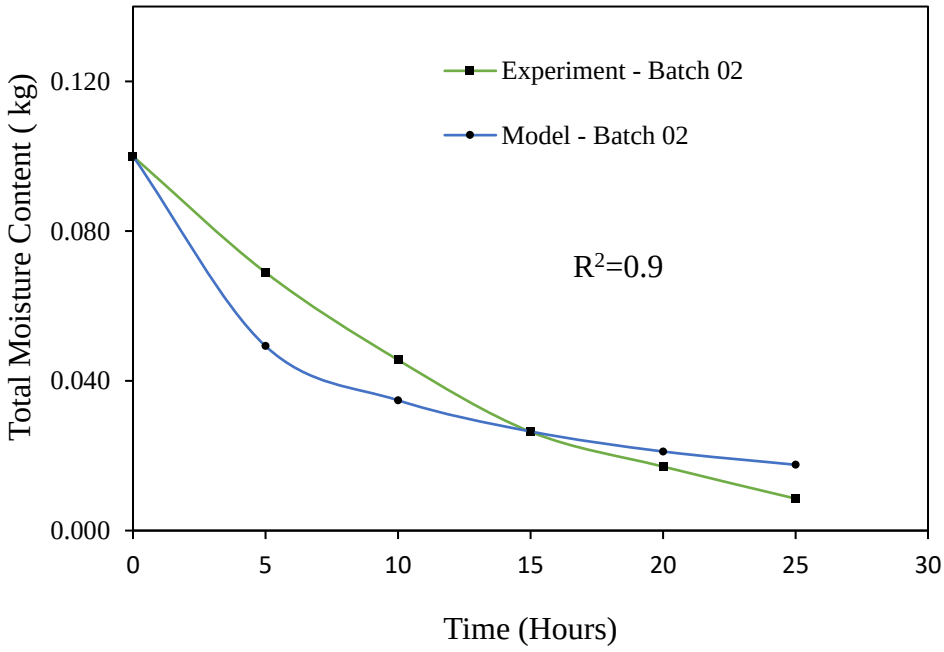

Figure 5.2: Comparison of model with experiment total moisture content variation of M2 Kaolin sample - Batch 02

5.1.2Drying Model Validation for Ceramic Tile

Moisture and dimension variation of the green ceramic tile samples with time were measured, and the critical moisture content of the green ceramic tile was 0.760%. The total moisture content variation of green ceramic tile with time was plotted as shown in Figure 5.3. The D_0 value of green ceramic tile, which was explained in equation (3.2), is calculated using bulk density and the equation (2.4) formula. The values of a_D and b_D constants in equation (2.4) were taken from reference [15].

The effective diffusion coefficient (D_m) of the green ceramic tile is varied with the temperature and D_0 value of the samples. The diffusion coefficient of green ceramic tile is a highly critical factor for the drying process of the ceramic body. The drying rate depends on the diffusion coefficient of the ceramic tile. Therefore, a mathematical model was developed using the effective diffusion coefficient (D_m). The effective diffusion coefficient (D_m) of ceramic tile was determined using calculated D_0 value, which is 778×10^{-6}, and Θ_D was taken from the reference [15], which was related to the bulk density and temperature.

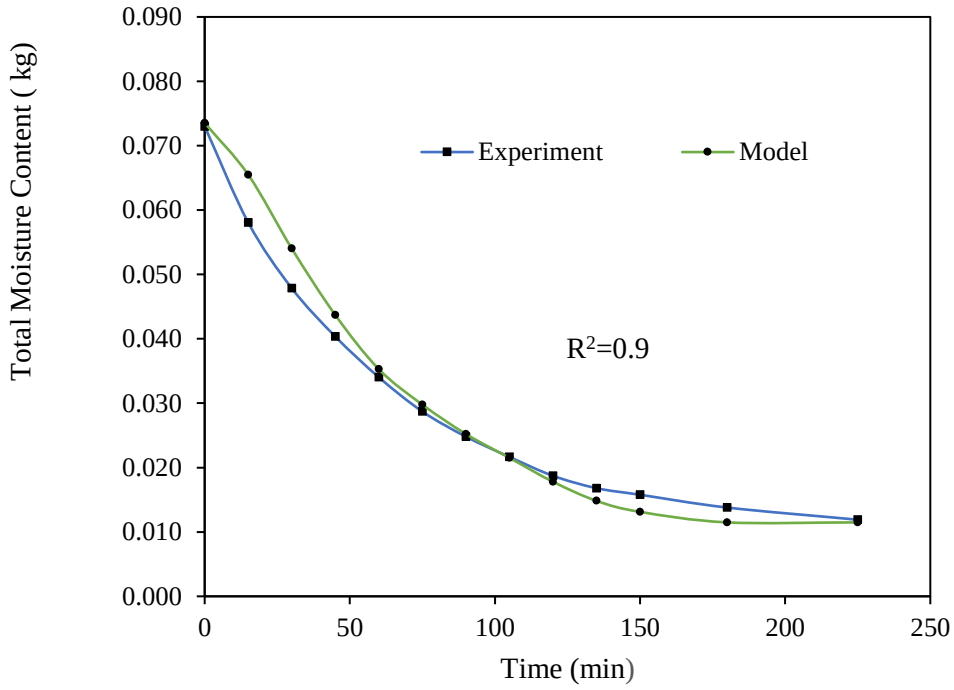

Figure 5.3: Comparison of model with experiment total moisture content variation of green ceramic tile sample

Table 5.2: COMPARISON OF MODEL WITH EXPERIMENT TOTAL MOISTURE CONTENT VARIATION OF GREEN CERAMIC TILE

Time (min)	Total Moisture Content (kg)	
	Experiment	Model
0	0.073	0.074
5	0.058	0.065
15	0.048	0.054
30	0.040	0.044
45	0.034	0.035
60	0.029	0.030
75	0.025	0.025
90	0.022	0.022
105	0.019	0.018
120	0.017	0.015
135	0.016	0.013
150	0.014	0.011
180	0.012	0.011
255	0.011	0.011
300	0.011	0.011

The mesh was enhanced and assessed using the drying model to ensure that the results are independent of cell size. Figure 5.3 is shown in the simulation results developed by the model and the experiment results of the total moisture content variation of the ceramic tile with time. Table 5. Shows the experimental and model results of the total moisture content variation of the ceramic tile with time. According to the model, the total moisture content variation of the samples was reduced with time. Simulation results developed by the model were compared and analysed with data obtained by

experiments conducted using green ceramic tiles. The model results were validated and complied with the results of the experiment. R^2 value was 0.9.

In Figure 5.3, there is some discrepancy between the experimental and model predictions against experimental findings. In the developed drying model, porosity variation with time of the ceramic tile body is neglected, and that may be the main reason for this deviation in Figure 5.3. However, the drying shrinkage of ceramic tile is very low, as shown in Figure 4.16. The impact of drying shrinkage can be added to the drying model, and this deviation of experiment and model findings can be minimized.

It was assumed that the internal green ceramic tile body had homogeneous temperature distribution during the drying process due to the low drying temperature and the drying is considered as isothermal process. The constant state parameters of the drying model were selected for drying model such as constant specific heat capacity, constant thermal conductivity, and constant diffusion coefficient. However, these values can be a deviation during the drying process, and it was not including the model. So, the results of the model can be deviated from the experiment findings. The experimental errors also can be added. it is difficult to obtain homogeneous, isotropic condition during the experiment. Therefore, the model and experiment curves can be deviated.

The effective moisture diffusion coefficient (D_m) was determined with the correlation of $D_{0,}$ Θ_D and drying temperature. The internal microstructure and bulk density of the sample were varied with the particle size distribution of clay. D_0 and Θ_D values were estimated with the correlation of bulk density and temperature of the samples. Therefore, the microstructure of the samples had an effect on drying curves for ceramic materials.

5.2Sintering Model Validation

5.2.1Mesh Refinement of Sintering Model

To be certain that the outcomes are unaffected by cell size, the mesh was improved and evaluated using the sample model. The number of mesh cells created for the example tile was initially 24000. After that, it increased to 48000, but there was no discernible difference in the outcomes after 48000.

5.2.2Simulation Results-Linear Shrinkage Variation

The primary source of data for this CFD model is the experiment's sintering cycle. Figure 3.3 displays the experiment sintering cycles, which were given as boundary conditions of temperature. The main output of the model is linear shrinkage. The results presented by the mathematical model show that there are temporal and spatial changes in the linear shrinkage of ceramic tiles. The highest and lowest linear shrinkage can be observed on the surface and centre point of ceramic tile, respectively. Figure 5.4 shows the model results of linear shrinkage variation with different mesh sizes, and Mesh-1 and Mesh-2 represent 42000 and 36000 number of cells, respectively. Model represents the refining mesh results of linear shrinkage. The average linear shrinkage value related to the sintering cycle was taken from the refining model results, and it was compared with the experimental results.

The model-generated simulation results and the experimental data of the sample's linear shrinkage variation with sintering temperature are shown in Figure 5.5. The characteristics of linear shrinkage increased because of the sintering cycle. Low linear shrinkage is observed in the 600–950 ºC range, where surface diffusion is the major

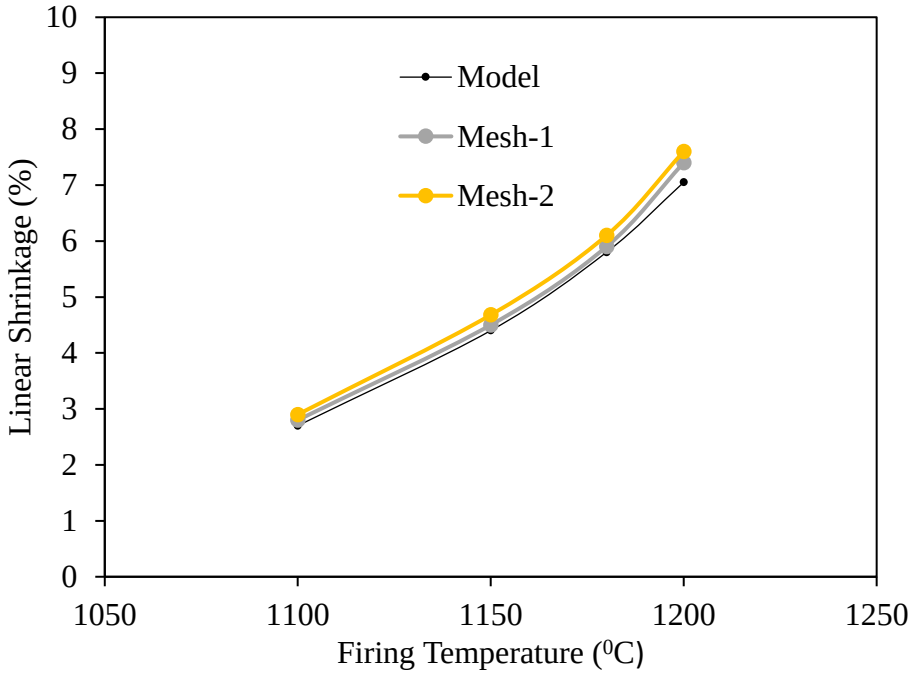

Figure 5.4: Linear shrinkage variation of fired ceramic tile with maximum sintering temperature -Model

sintering mechanism. Because of the production of mullite and liquid phases, linear shrinkage increases between 1000 and 1100 ºC. However, a high degree of

densification occurred in the ceramic tile body above 1100 ºC, and the linear shrinkage increased in the ceramic tile body [18], [20], [23], [24]. At this point, ceramic tile body densification coincides with the production of a substantial quantity of liquid. The process referred to as liquid phase sintering densifies the structure.

According to Table 5.3, a slight variation is observed between the model simulation and the experiment's linear shrinkage results. In this research, the linear shrinkage kinetic model parameters were chosen from reference data that fitted the study's current body compositions, oxide composition, and LOI. But exact kinetic model parameters related to this body composition can't be found from the reference data. Variations in a few chosen model parameter values and experimental errors can lead to different results. However, the outcomes of the linear shrinkage numerical model simulation exhibited a strong correlation with the experimental laboratory data. The results obtained from the CFD simulation were validated and concurred with experimental outcomes, and the R^2 value of the results was 0.9. The simulation results were analysed by changing the mesh size. The number of mesh cells created for the example tile was initially 24000. After that, it increased to 48000, but there was no discernible difference in the outcomes.

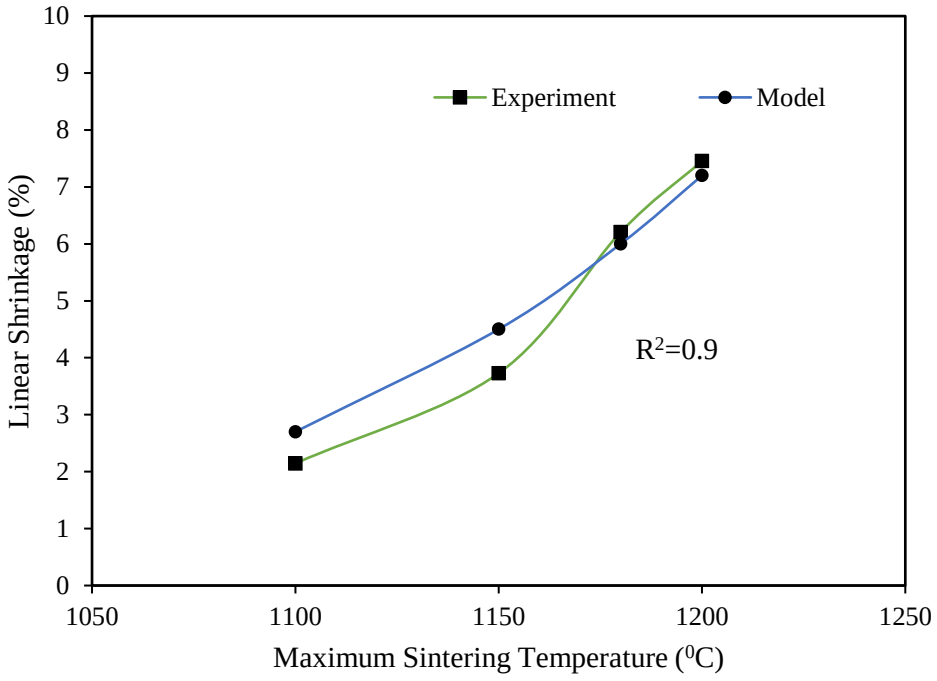

Figure 5.5: Linear shrinkage variation of fired ceramic tile with maximum sintering temperature

Table 5.3: LINEAR SHRINKAGE VARIATION OF SINTERED CERAMIC TILE WITH MAXIMUM SINTERING TEMPERATURE

Maximum Sintering	Linear Shrinkage (%)	
	Experiment	Model
1100	2.14	2.73
1150	3.73	4.52
1180	6.20	6.00
1200	7.45	7.25

5.2.3Simulation Results-Modulus of Rupture (MOR) Variation

Figure 5.6 shows the MOR model results variation with different mesh sizes, and Mesh-1 represent 42000 number of cells. Model represents the refining mesh results of MOR. The model-generated simulation results and the experimental data of the sample's MOR variation with sintering temperature are shown in Figure 5.7. According to the model simulation results, the MOR value of the ceramic tile body varies from location to location, and the average MOR value was used to graph Figure 5.7. The sintering cycle resulted in an increase in MOR's features. The capacity to create glassy phases improved with temperature and sintering time, providing adequate support for densifying the body of the ceramic tile. Ceramic tile body bonding strength between glassy phase and particles increased during the cooling stage [73]-[77]. So, the modulus of rupture increases with sintering temperature.

According to Table 5.7, a slight variation is observed between the model simulation and the experiment's MOR results. In this research, deflection in the center of the ceramic tile (h) for the MOR variation kinetic model for fired ceramic tiles was chosen from reference data that fitted the study's initial body compositions and final dimension. However, the sintering temperature affects the ceramic tile's center deflection (h) characteristic, and it was not present in the reference data. Constant value variations in a few chosen model parameter and experimental errors can lead to different results. However, the outcomes of the MOR numerical model simulation exhibited a strong correlation with the experimental laboratory data. The results

obtained from the CFD simulation were validated and concurred with experimental outcomes, and the R^2 value of the results was 0.9.

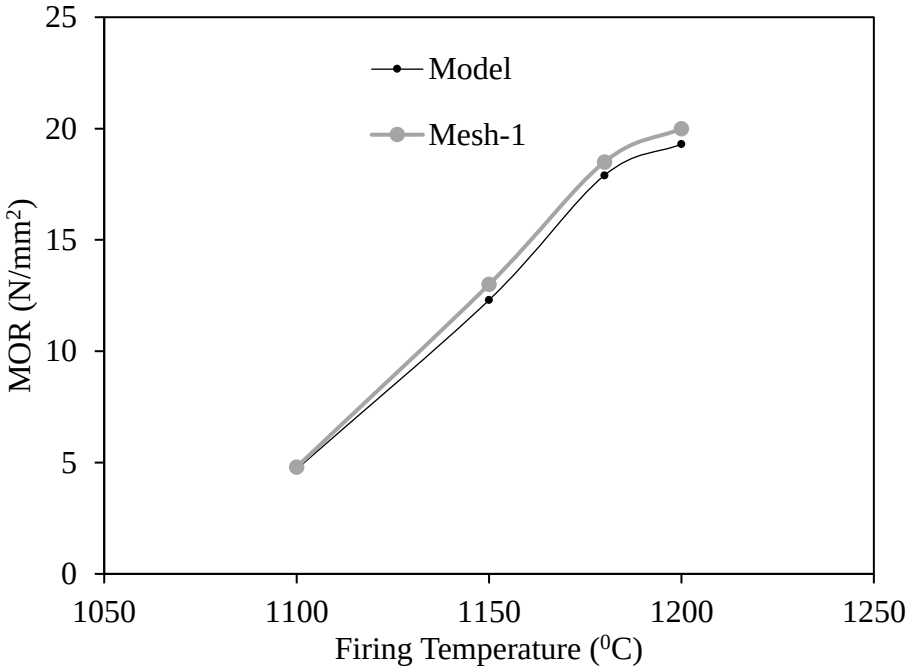

Figure 5.6: MOR variation of fired ceramic tile with maximum sintering temperature-Model

Table 5.4: MOR VARIATION OF SINTERED CERAMIC TILE WITH MAXIMUM SINTERING TEMPERATURE

Maximum Sintering Temperature (^{0}C)	**MOR (Nmm^{-2})**	
	Experiment	**Model**
1100	3.5	5.06
1150	11.9	11.8
1180	18.6	19.1
1200	20.7	21.9

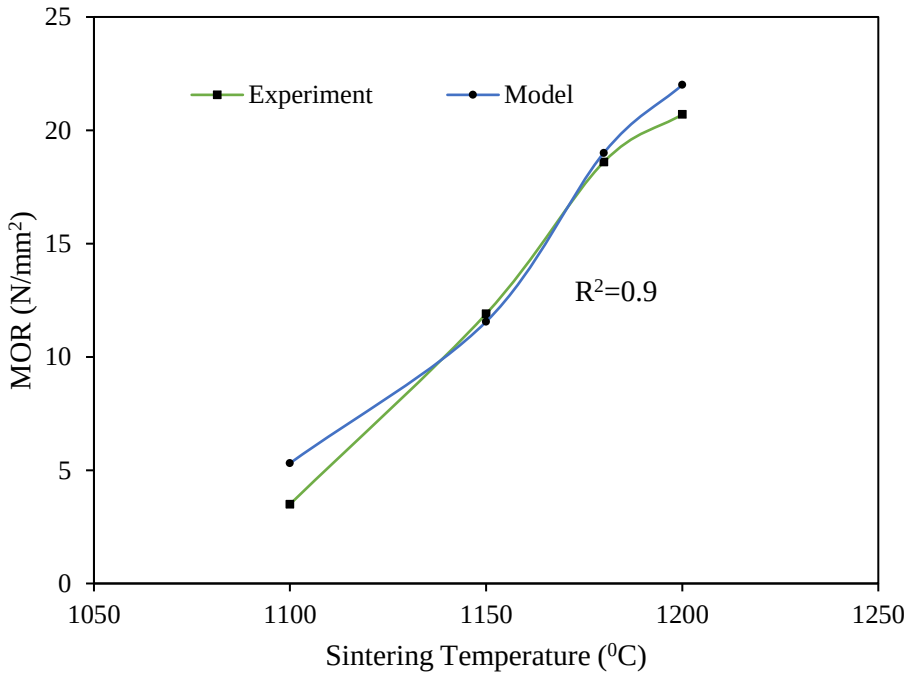

Figure 5.7: MOR variation of fired ceramic tile with maximum sintering temperature

CHAPTER 6

6. RESULTS AND DISCUSSION

6.1.Main Features and Importance of Drying Model

Figure 6.1 shows moisture evolution along the diagonal of the ceramic tile at 80 °C. In the beginning of the drying process, the moisture content is homogeneous within the green ceramic tile body. The moisture content of the ceramic tile is progressively raised from the surface to the central point with drying time. Finally, the moisture content of the whole ceramic tile body achieved equilibrium moisture content. A developed drying model gets used to calculate the temperature and moisture fluctuation in the green ceramic tile body both spatially and temporally throughout the drying process. This model is a great help to predict the drying time for green ceramic tile in relation to drying temperature. Any tile dimension can possibly be used with this model, and drying times can be estimated.

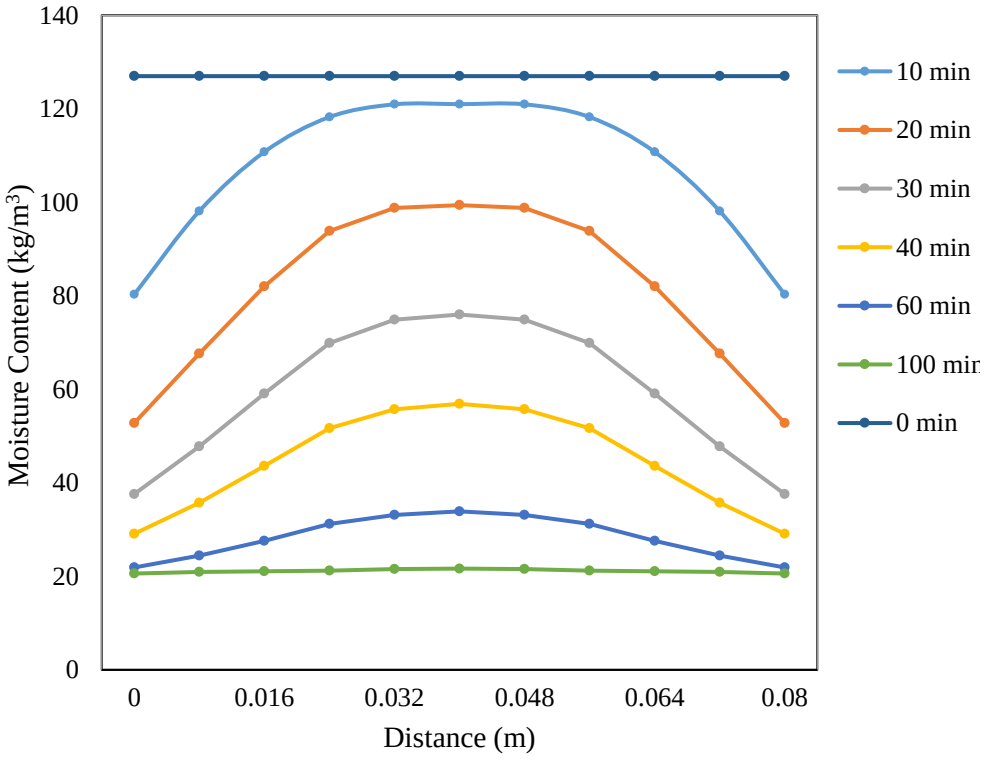

Figure 6.1: Moisture evolution along the diagonal of the ceramic tile at 80 ^{0}C and 7% of initial moisture content

The specific heat capacity, thermal conductivity, is the most important material behavior-related property, which depends on the body composition of ceramic tiles. The moisture diffusion coefficient is dependent on the drying temperature and packing density of the green ceramic tile body. This model can be applied to any composition of ceramic tiles by changing materials and process-related parameters. The moisture evaluation throughout the ceramic body with drying time obtained from the drying model and the optimum drying cycle related to green ceramic tiles can be analysed using the developed drying model.

6.2.Drying Profile Optimization

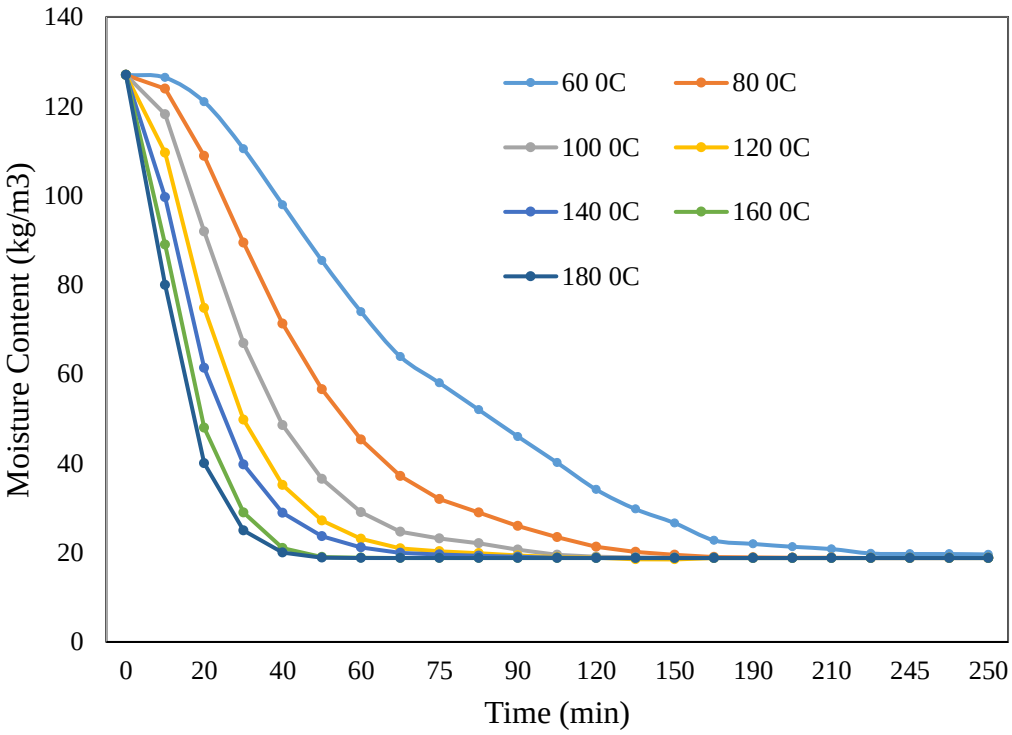

Figure 6.2: Drying cycle variation of green ceramic tile with drying temperature-initial moisture content 7%

The ignition of organic compounds in the ceramic body mixer occurs if the temperature reaches 200 °C [110]. Removing physically bound water from the ceramic tile body is the main objective of the drying process. So, the drying temperature of the ceramic tile body needs to be lower than 200 °C. However, optimum drying rate is changed with

body composition and ceramic body shape, and it needs to be found using optimisation theory. Therefore, the drying temperature of ceramic tile was increased up to 180 °C during the drying profile optimisation, and simulation results of the drying profile and maximum moisture exchange rate were analysed. Figure 6.2 represents the variation of the moisture content of the ceramic tile with drying temperature, which contains 7% of the initial moisture content. The drying cycle of the ceramic tile is reduced with an increase in drying temperature. The highest and lowest drying times are 255 min and 60 min at 60 °C and 180 °C, respectively. Figures 6.3 show moisture evolution along the diagonal of the ceramic tile at 180 °C.

The gradient of moisture content along the diagonal of ceramic tile decreases with time. According to Table 6.1, the moisture exchange rates of ceramic tiles by varying drying temperature are between 2.5×10^{-8} and 8.4×10^{-8} ms^{-1}. Homogeneous moisture distribution through the ceramic tile body with critical moisture content (CMC) appears during drying, and the moisture exchange rate is lower than 0.000001 ms^{-1}. It was confirmed that the maximum drying temperature of this ceramic tile is 180 °C without cracks. The optimum drying time of the ceramic tile is 60 min, representing a 76.4% reduction compared to the reference drying time. This reduction contributes to lower production costs in the drying process. Additionally, energy costs are minimized, as heat loss decreases with shorter drying times.

Table 6.1: MAXIMUM MOISTURE EXCHANGE RATES OF CERAMIC TILES BY VARYING DRYING TEMPERATURE

Drying temperature (^{0}C)	60	80	100	120	140	160	180
Maximum Moisture exchange rate, α (m/s) $\times10^{-8}$	2.5	3.0	3.3	4.0	4.9	7.8	8.4

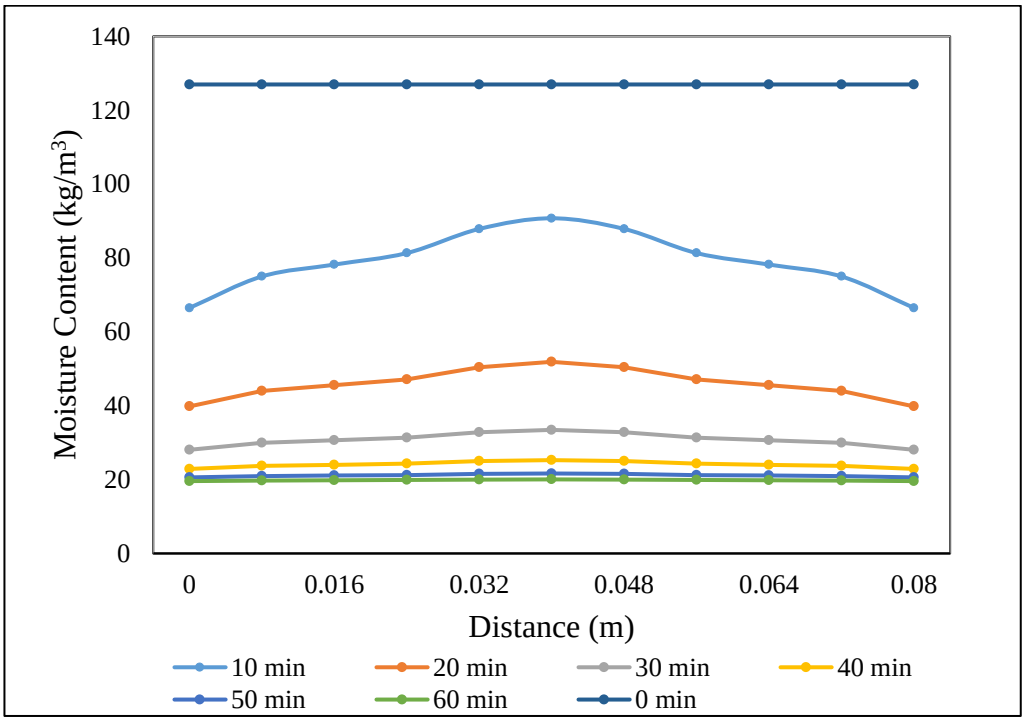

Figure 6.3: Moisture evolution along the diagonal of the ceramic tile at 180 ^{0}C and 7% of initial moisture content

6.3.Main Features and the Importance of Sintering Model

The spatial and temporal variation of temperature in the ceramic tile body during the sintering process can be determined using the sintering model. The density of the tile, the linear shrinkage, MOR, and the thermal stress variation related to the sintering cycle can be obtained using the sintering model. The maximum sintering temperature of ceramic tiles is 1200 °C, which was achieved at 260 min. Spatial variation of temperature in ceramic tile during the sintering process is shown in Figures 6.4 and 6.5. The outside surface of the ceramic tile achieves the maximum temperature compared to the inside of the body throughout the sinter. It is verified that the radiation heat is delivered uniformly over the body surface of the ceramic tile on the outside surface that is immediately exposed to heat loss from the furnace walls. Therefore, the temperature decreased progressively from the outer layers into the core of the ceramic tile body.

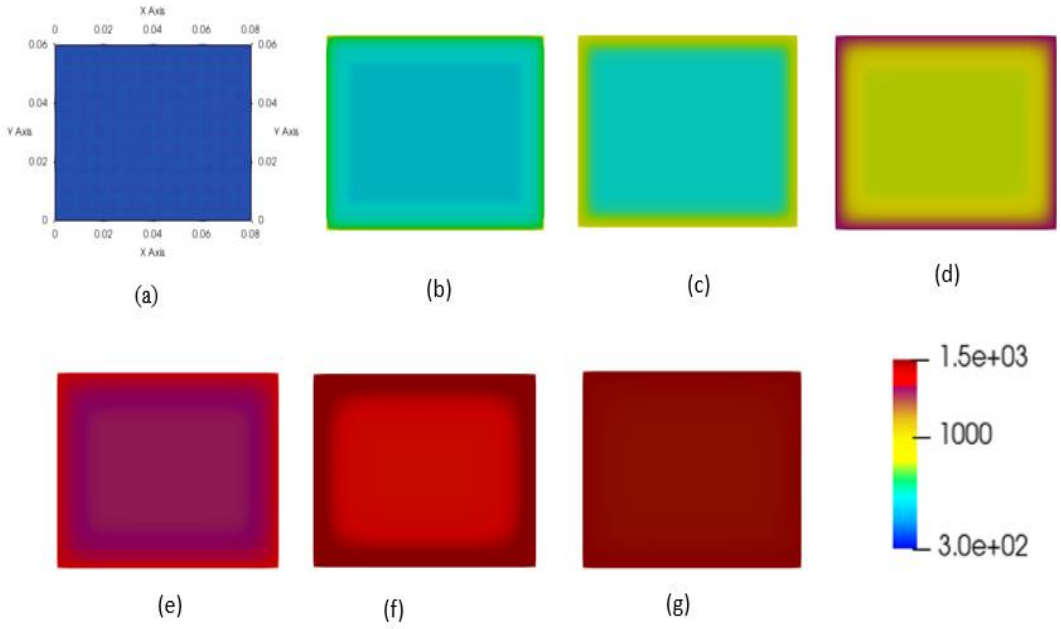

Figure 6.4: Spatial variation of temperature along middle axis of x-y plane in ceramic tile body during the sintering process- maximum sintering temperature 1200 ^{0}C (a) 0min, (b) 20min (c) 45min (d) 120min (e) 200min (f) 260min (g) 290min

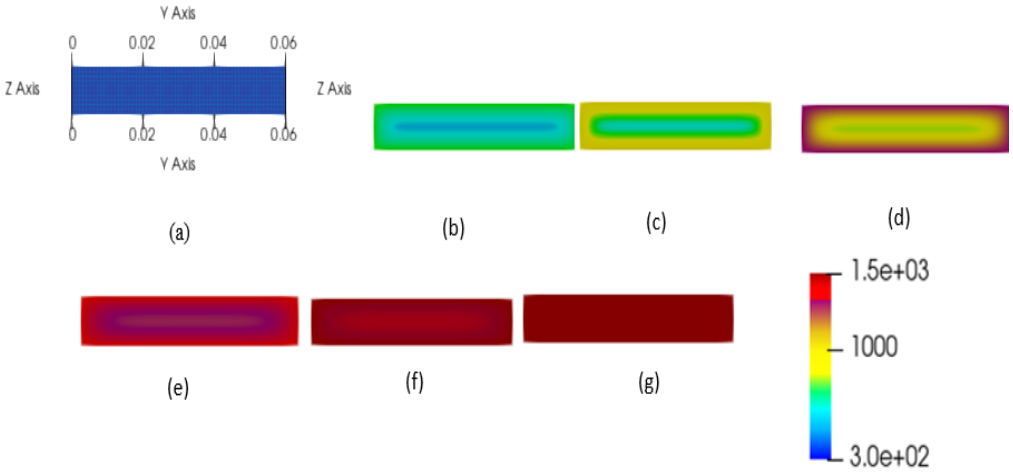

Figure 6.5: Spatial variation of temperature along middle axis of z-y plane in ceramic tile body during the sintering process- maximum sintering temperature 1200 ^{0}C (a) 0min, (b) 20min (c) 45min (d) 120min (e) 200min (f) 260min (g) 290min

Figures 6.6, 6.7, and 6.8 illustrate the comparison of spatial temperature and linear shrinkage of the ceramic tile at 260 min and 290 min from the middle point of the ceramic body to the surface along the x, y, and z axes in the ceramic tile body for different sintering times. According to the sintering cycle in Figure 3.3, the maximum sintering temperature of ceramic tiles is 1200 °C, which was achieved at 260 min. A significant amount of spatial variation in temperature and linear shrinkage is observed from the middle point of the ceramic body to the surface along the x, y, and z axes in the ceramic tile body. After the ceramic tile was soaked for 30 minutes, a spatial variation of linear shrinkage was observed from the middle point of the ceramic body to the surface along the x, y, and z axes in the ceramic tile body. Eventually, the body temperature reaches an equilibrium value of 1200 °C after 290 minutes of sintering. The highest shrinkage was observed at the surface of the tile, and it is 7.39%. The lowest value of linear shrinkage is 7.19% at the middle point of the ceramic tile body. The linear shrinkage of the ceramic tile body varies with sintering time and location of the ceramic tile body.

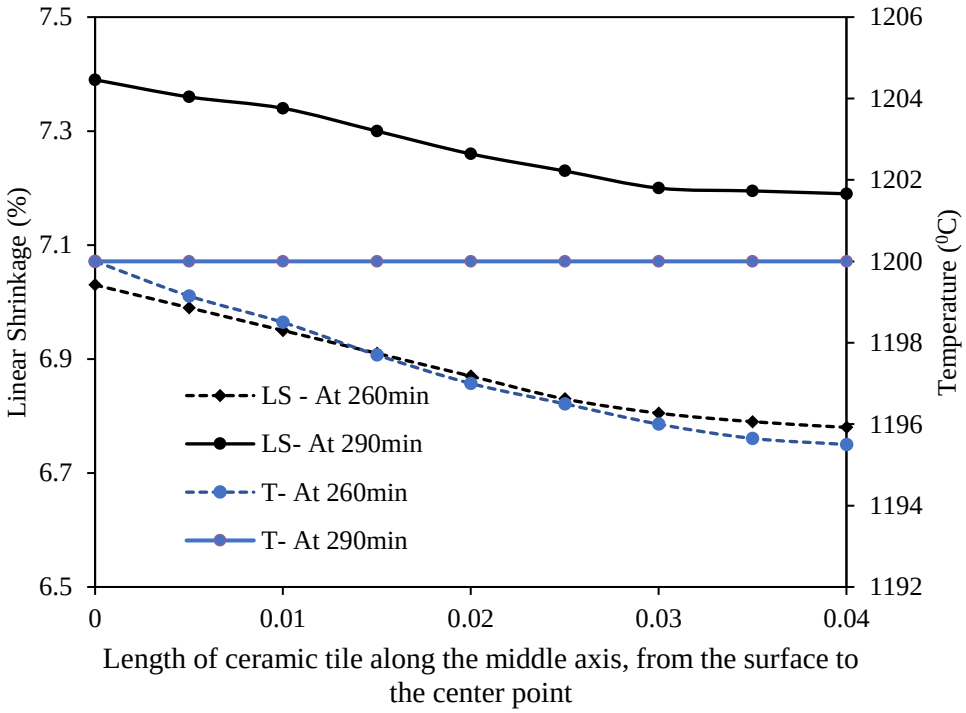

Figure 6.6: Comparison of the spatial variation between the temperature profile and shrinkage from the middle point of ceramic body to along the x axis in ceramic tile body for different sintering times

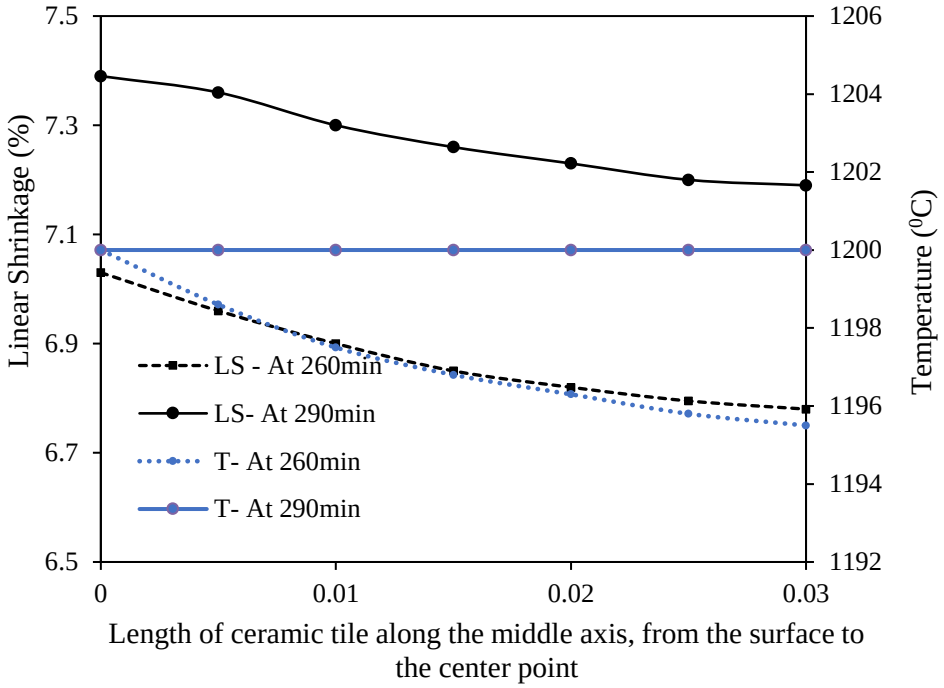

Figure 6.7: Comparison of the spatial variation between the temperature profile and shrinkage from the middle point of ceramic body to along the y axis in ceramic tile body for different sintering times

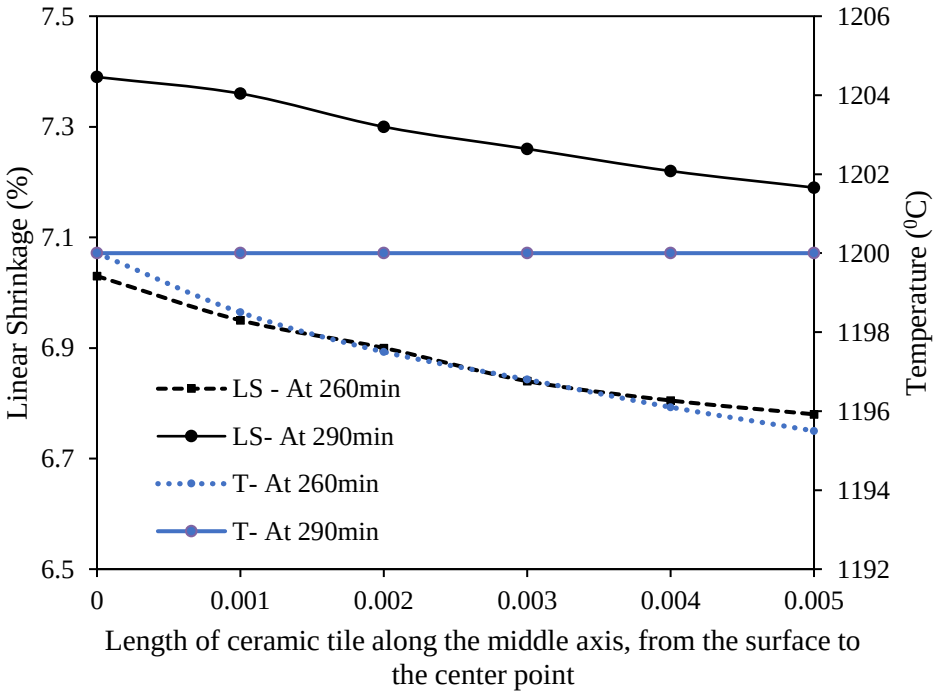

Figure 6.8: Comparison of the spatial variation between the temperature profile and shrinkage from the middle point of ceramic body to along the z axis in ceramic tile body for different sintering times

In this research, the body composition is not varied, and n, k_0, and E_A is the same for every sintering profile. The linear shrinkage in this research is most sensitive to the sintering profile. The kinetic model was used to calculate the linear shrinkage variation of ceramic tile, and the kinetic model parameters (n, E_A, K_0) of linear shrinkage depended only on the body composition of ceramic tile. In this research, the linear shrinkage kinetic model parameters were chosen from reference data that fitted the study's initial body compositions, oxide composition, and LOI. But exact kinetic model parameters related to this body composition can't be found from the reference data. This can be resolved; experimental measurements of the ceramic tile's linear shrinkage variation with sintering temperature will be made for this study. It is possible to determine the precise linear shrinkage parameters, and the model can be improved. According to the model simulation results, the temperature of the ceramic tile body varies from location to location. The viscous phase formation and moving ability of ceramic tile depend on temperature and retention time [32], [72]. Temperature retention time also changed spatially and temporally. After the soaking period, the whole tile body achieved maximum temperature, but the sintering profile is dissimilar from location to location. Therefore, the results presented by the mathematical model show that there are temporal and spatial changes in the linear shrinkage of ceramic tiles due to the differences in their sintering profiles.

In this research, deflection in the center of the ceramic tile (h) for the MOR variation kinetic model for fired ceramic tiles was chosen from reference data that fitted the study's initial body compositions and final dimension. However, the sintering temperature affects the ceramic tile's center deflection (h) characteristic, and it was not present in the reference data. This can be resolved; experimental measurements of the deflection of the ceramic tile variation with sintering temperature will be made for this study. It is possible to determine the precise deflection of the ceramic tile, and the model can be improved.

Figure 6.9 shows the density fluctuation of the ceramic tile body during the sintering process. The volume of the ceramic tile is constant up to 900 ^{0}C, and the mass of the ceramic tile body is decreased due to the formation of metakaolin and the decomposition of dolomite. So, the ceramic tile's initial density of 1853 kgm^{-3} decreases with time. The volume of the tile is decreased after 900 ^{0}C, and the density of the tile is increased. After 1110 ^{0}C, the volume reduction rate is high due to the

shrinkage, and density also increased gradually up to 2000 kgm^{-3}. Specially, the soaking time of the sintering cycle has a major role in controlling the density of ceramic tile. Sintering cycle optimization can be done by using this model. The temperature evaluation throughout the ceramic tile body with sintering time obtained from the sintering model and the optimum sintering cycle related to physical and mechanical properties can be analyzed using the developed sintering model.

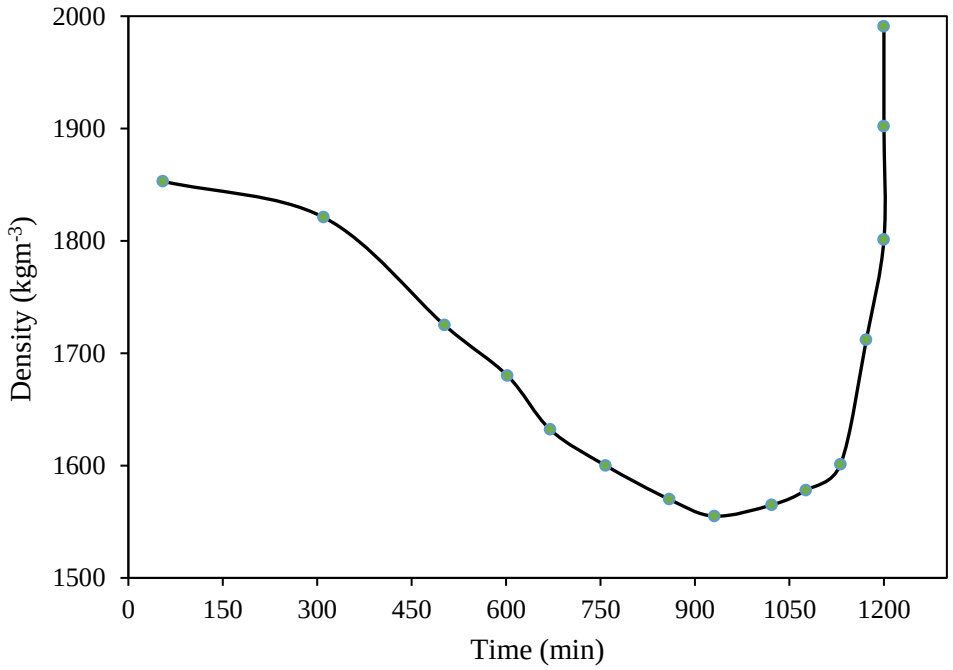

Figure 6.9 Density variation of ceramic tile body during sintering -maximum sintering temperature 1200 ^0C

6.4. Sintering Profile Optimization

The CFD simulation results associated with thermal stress and mechanical stress variations of ceramic tile for different sintering profiles were obtained. The mechanical properties of ceramic tile varied through sintering. The ceramic body loses its elastic properties and becomes plastic during glassy phase formation. The plastic behaviour of ceramic tiles increased during the cooling stage. Thermal stresses develop inside a material due to sudden temperature changes, which are related to the sintering profile. The thermal conductivity of the ceramic tile body directly affects the variation of thermal stress on the body. Quartz plays a major role in the fracture strength of ceramic tile bodies. Because of the thermal expansion mismatch with quartz, other phases can occur during the sintering cycle. It leads to appearing cracks. The fracture strength and

thermal stress developed in a ceramic tile body changed with the sintering profile. Figures 6.10, 6.11, 6.12 and, 6.13 show the variation of thermal stress and mechanical stress of the ceramic tile body during the heating stages. The mechanical breaking strength of the ceramic tile body and thermal stress is increased with the heating rate. Thermal expansion significantly increased between 550-573 °C due to quartz alpha conversion to quartz beta. Therefore, the thermal stress of ceramic body is suddenly increased after 550 ^{0}C. the heating rate of ceramic body need to be controlled without getting high thermal stress rather than mechanical stress. In this study, Thermal stress is greater than mechanical stress on the ceramic body when the heating rate is increased by 30.0 °C/min. Then microcracks can appear during the heating process above 30.0 °C/min. So most optimum heating rate for ceramic tile is 27.6 °C/min.

When the mechanical stress and thermal stress values are compared up to 550 °C, there is a possibility to increase the heating rate of ceramic tile to more than 27.6 °C/min. According to Figure 6.14and 6.15 the thermal stress of the ceramic body is higher than the modulus of rupture value during hearing rate above 54.0 °C/min. Thus, the data indicates that the maximum heating rate in the range of 30 to 550 °C is 51.6 °C/min.

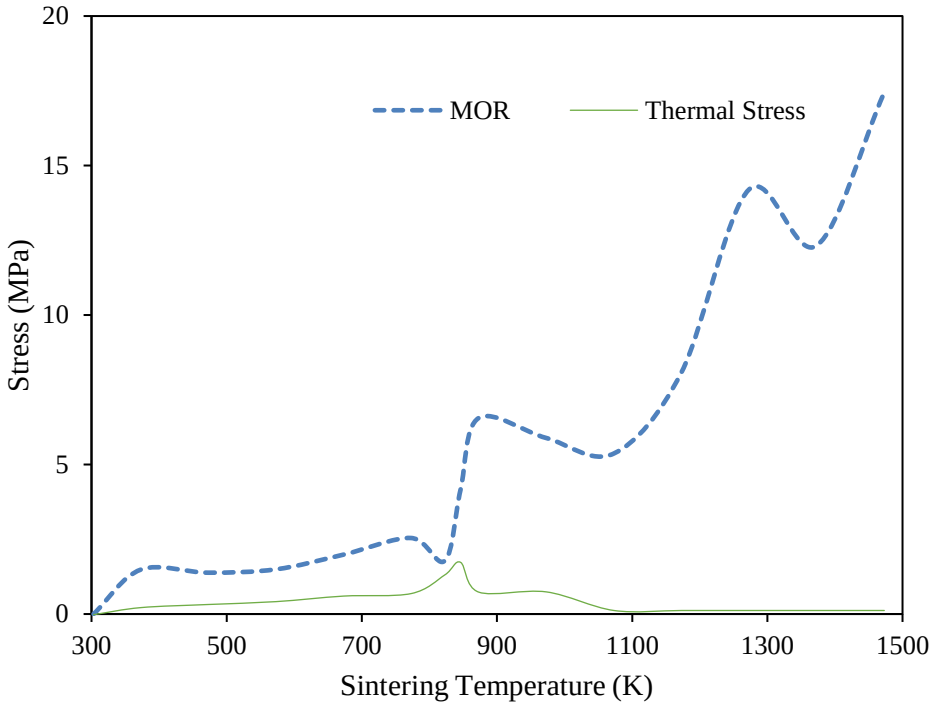

Figure 6.10: MOR and thermal stress variation of ceramic tile during heating stage. heating rate is 9.2 ^{0}C/min

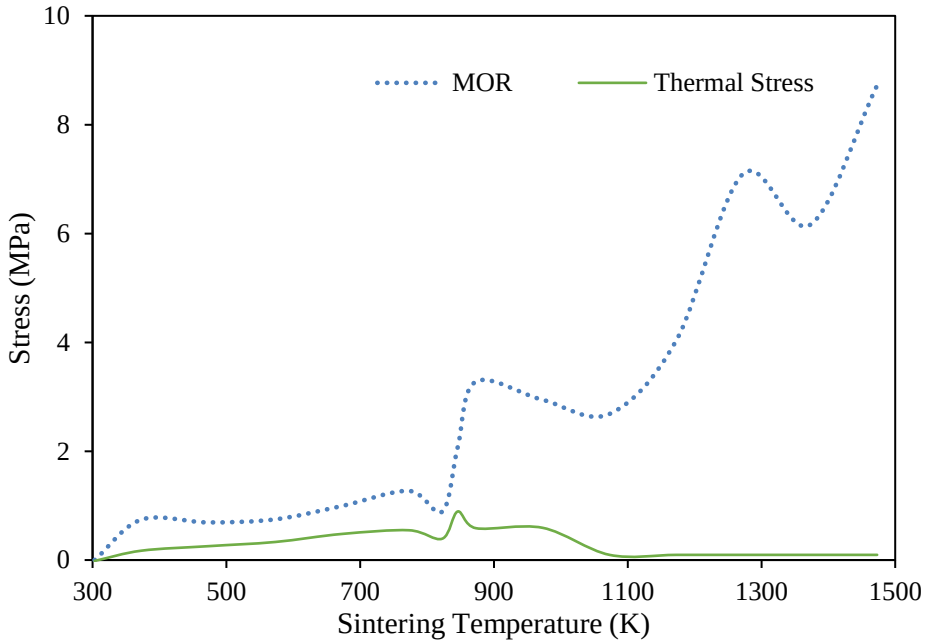

Figure 6.11: MOR and thermal stress variation of ceramic tile during heating stage. heating rate is 4.6 ^{0}C/min

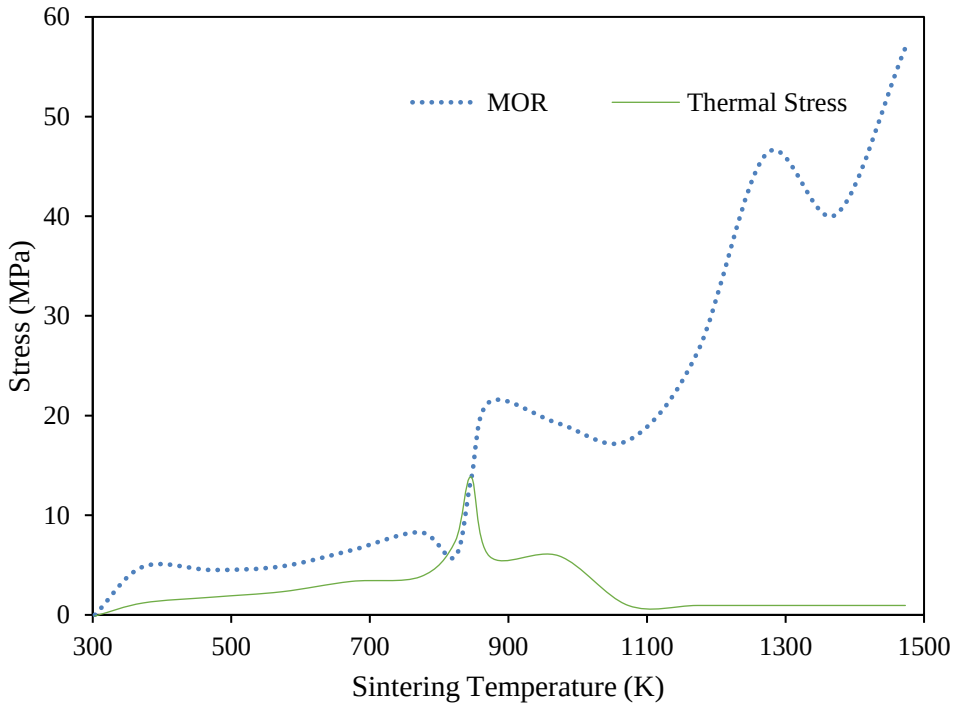

Figure 6.12: MOR and thermal stress variation of ceramic tile during heating stage. heating rate is 30.0 ^{0}C/min

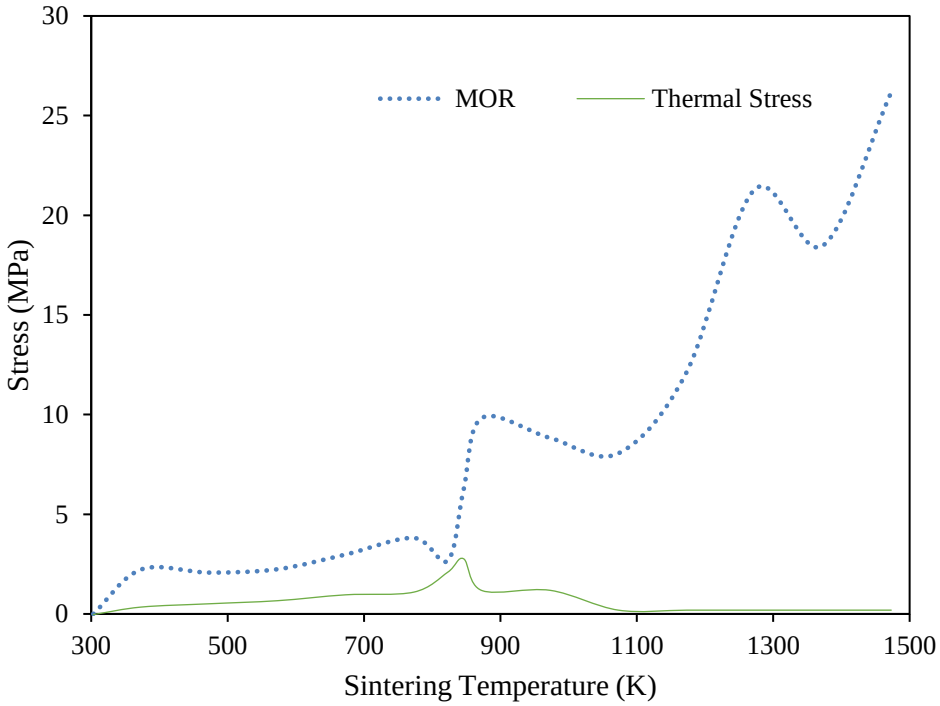

Figure 6.13: MOR and thermal stress variation of ceramic tile during heating stage. heating rate is 19.8 ^{0}C/min

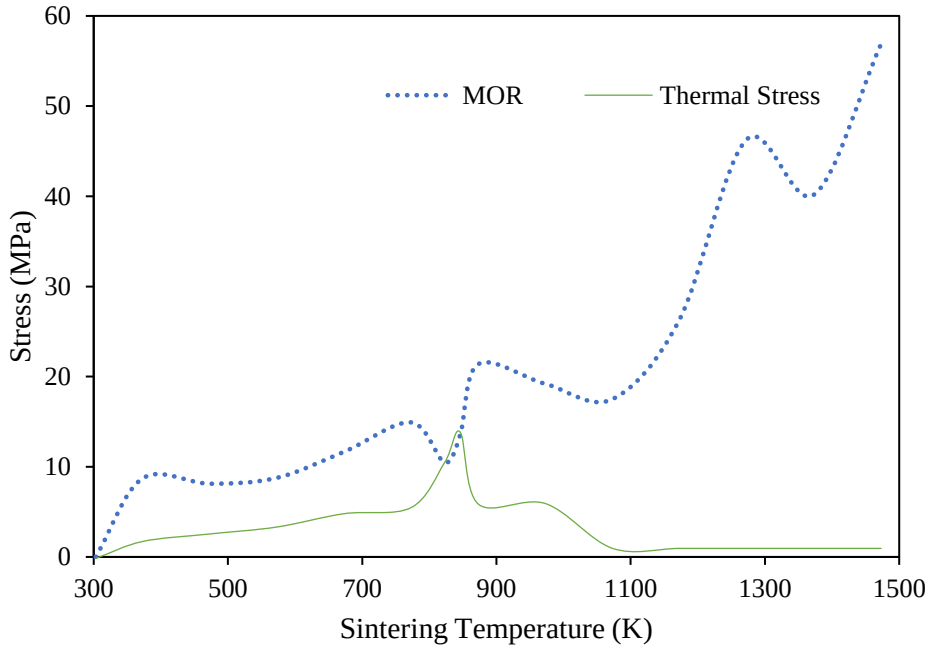

Figure 6.14: MOR and thermal stress variation of ceramic tile during heating stage. (a) heating rates are 54 ^{0}C/min between 30-550 ^{0}C, 30 ^{0}C/min between 550-1200 ^{0}C

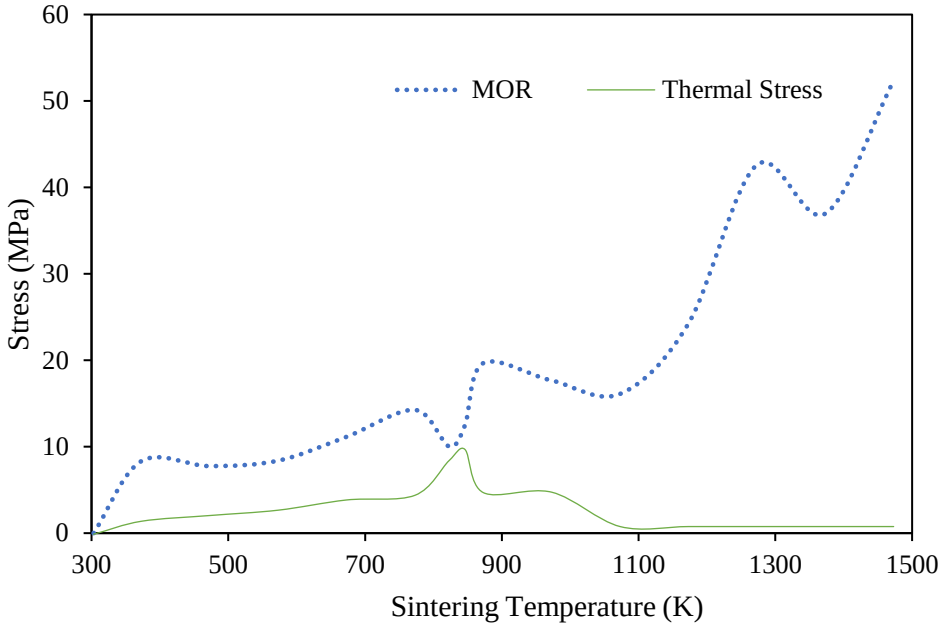

Figure 6.15: MOR and thermal stress variation of ceramic tile during heating stage. heating rates are 51.6 ^{0}C/min between 30-550 ^{0}C, 27.6 ^{0}C/min between 550-1200 ^{0}C

Figure 6.16, 6.17, 6.18 and, 6.19 show the variation of thermal stress and mechanical stress of the ceramic tile body during the cooling stage. The mechanical breaking strength and thermal stress are changed with the cooling rate. Elastic characteristics gradually return when the ceramic body cools down. In this time, the glassy phase's viscosity increases. The ceramic material becomes porcelain. The cooling period can be divided into two parts. The volume of the quartz grain is nearly constant between 1200- 575 °C, but the glassy cladding begins to lose volume. The relatively large volume change accompanying the $\beta \rightarrow \alpha$ transformation of the unsolved quartz grains is the basic source of microcracking of ceramic tile bodies during the cooling period.

Thermal stress is increased more than mechanical stress of the ceramic body when the cooling rate is increased by 21 ^{0}C/min. Then micro-cracks can appear during the cooling process above 21 ^{0}C/min. So, the optimum cooling rate of the ceramic tile body is 19.8 ^{0}C/min. Figure 6.20 shows the variation of thermal stress and MOR of ceramic tile for dynamic cooing rates.

When the mechanical stress and thermal stress values are compared up to 800 °C, there is a possibility to increase the cooling rate of ceramic tile to more than 19.8 °C/min.

The glassy phase must be transformed throughout the glassy phase transition procedure without experiencing internal softening or surface hardening. The midway temperature of the ceramic body was less than 1118 °C when the surface temperature reached 1000 °C. As a result, the temperature change of the ceramic tile body with cooling rates is shown in Figure 6.21. The data indicates that the maximum cooling rate in the range of 1200 to 1000 °C is 57 °C/min.

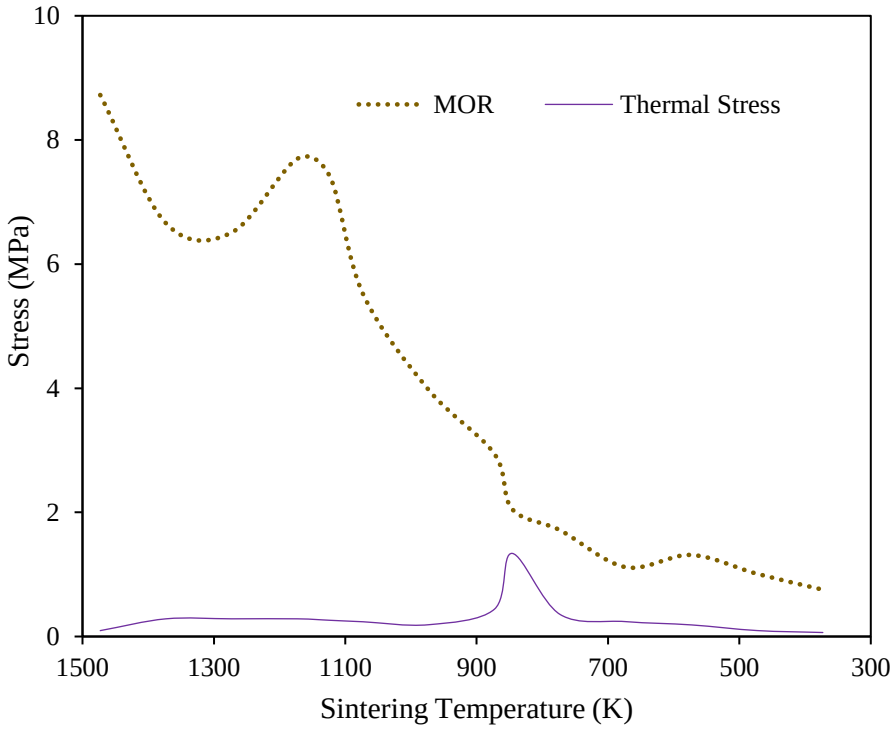

Figure 6.16: MOR and thermal stress variation of ceramic tile during cooling stage. cooling rate is 3.6 ^{0}C/min

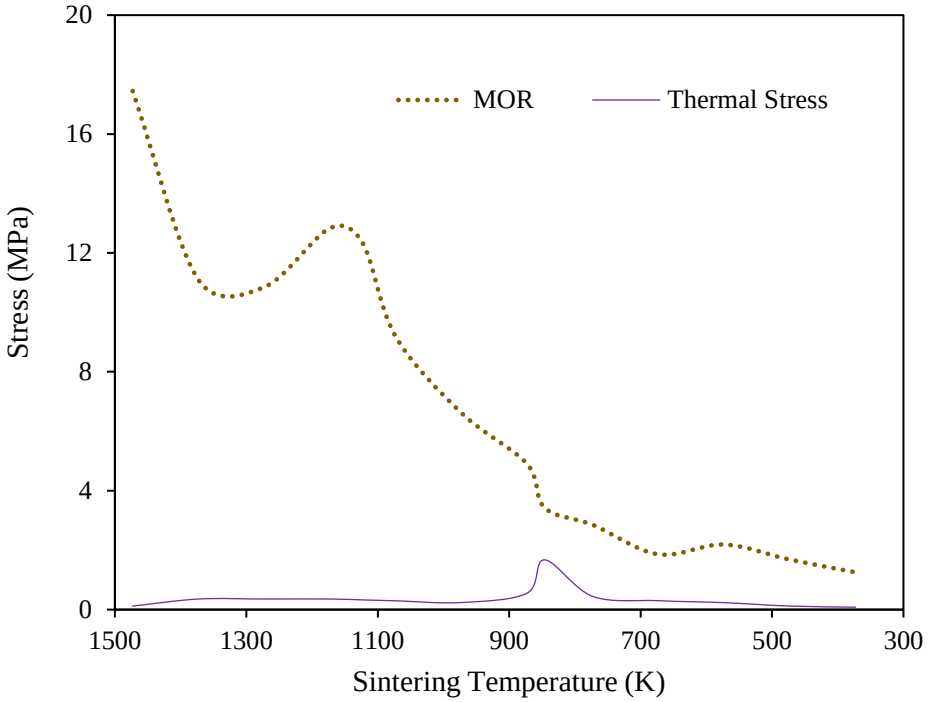

Figure 6.17: MOR and thermal stress variation of ceramic tile during cooling stage. cooling rate is 6.0 ^{0}C/min

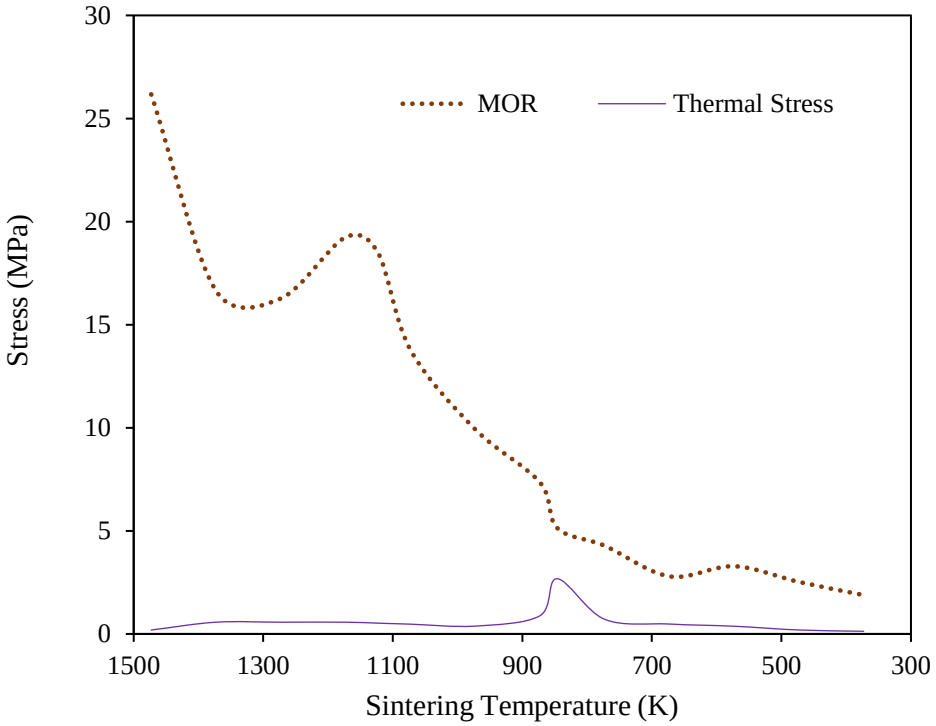

Figure 6.18: MOR and thermal stress variation of ceramic tile during cooling stage. cooling rate is 18.0 ^{0}C /min

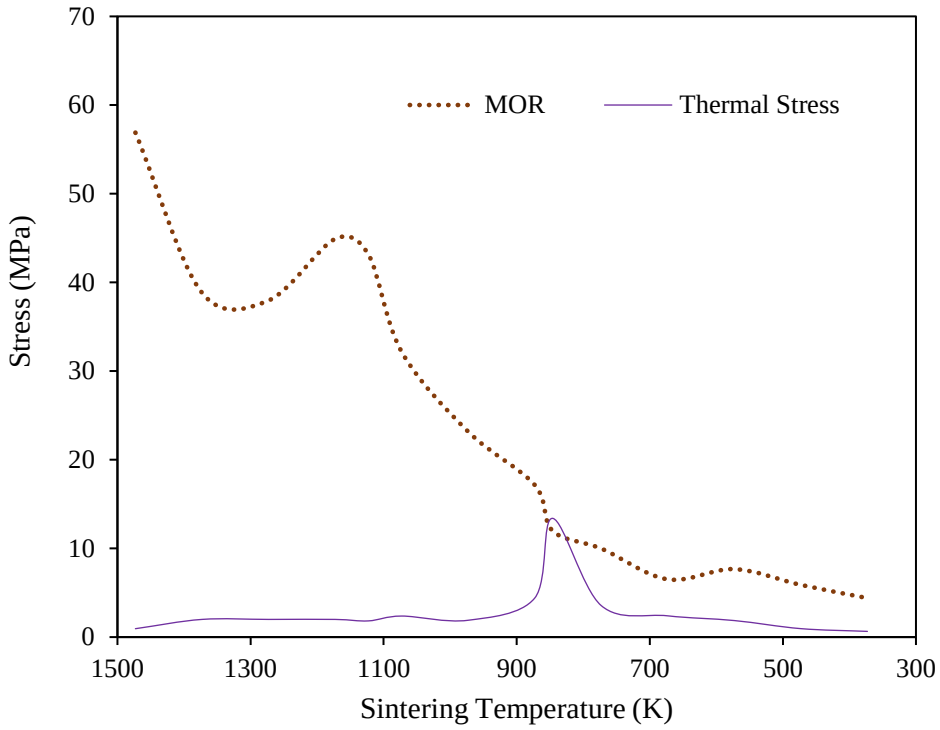

Figure 6.19: MOR and thermal stress variation of ceramic tile during cooling stage. cooling rate is 21.0 ^{0}C/min

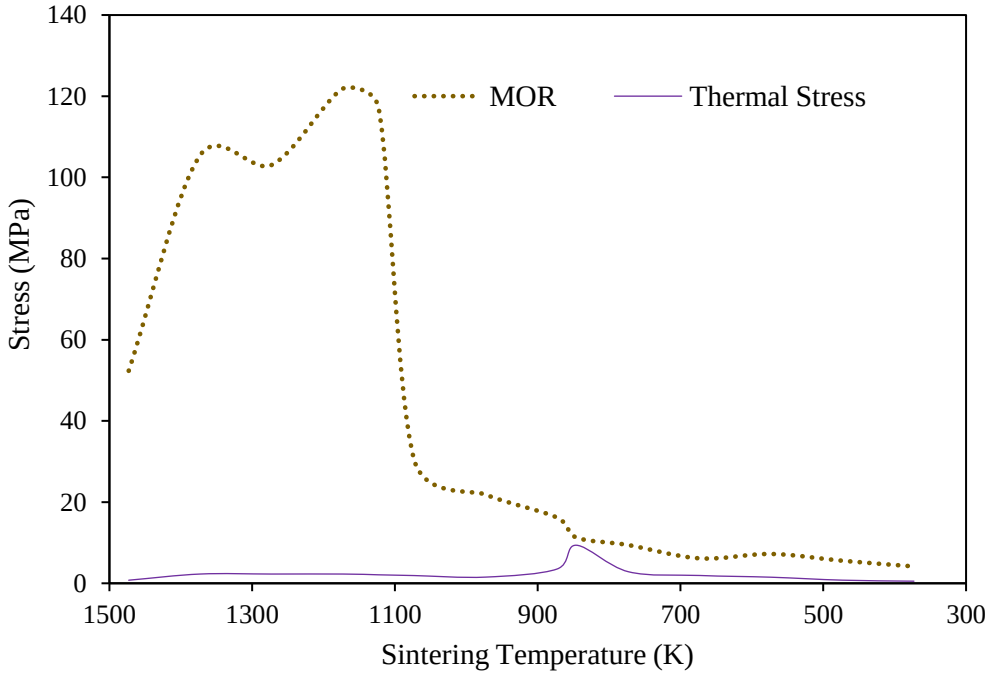

Figure 6.20: MOR and thermal stress variation of ceramic tile during cooling stage. cooling rates are 57 ^{0}C/min between 1200-1000 ^{0}C, 19.8 ^{0}C /min between 1000-30 ^{0}C

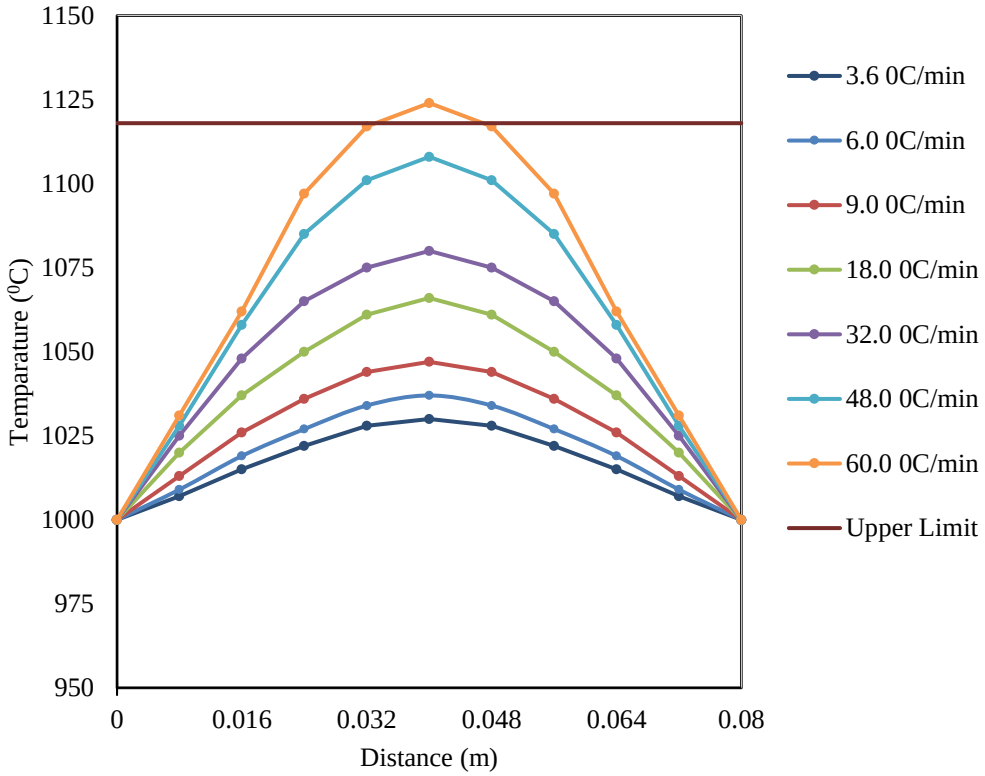

Figure 6.21: Temperature variation of ceramic tile body with cooling rate

The optimal sintering cycle is shown in Figure 6.22, and the constant rate cycle was made by considering only internal thermal and mechanical stress through the sintering. The dynamic rate cycle was prepared by comparing internal stress and reaction completion ability. The constant rate cycle included the optimum heating and cooling rates of 27.6 °C/min and 19.8 °C/min, respectively.

Total sintering time variation with sintering cycle type is shown in Table 6.2. The total time of the optimum constant sintering curve is 112.7 minutes, with 10 minutes of soaking time. The dynamic rate cycle included 51.6 °C/min heating rate between 30-550 ^{0}C, 27.6 °C/min heating rate between 550-1200 ^{0}C, 57 °C/min cooling rate between 1200-1000 ^{0}C, and 19.8 °C/min cooling between 1000-30 ^{0}C. The total time of the optimum dynamic rate sintering curve is 96 minutes.

In this research, the total time period of the sintering curve is 700 minutes with 30 minutes of soaking time. The optimum sintering time of the ceramic tile is 96 min, an 82.2% reduction compared to the reference sintering time. This significantly lowers production costs and improves productivity in the sintering process. Additionally, the shorter time reduces energy costs by minimizing heat loss.

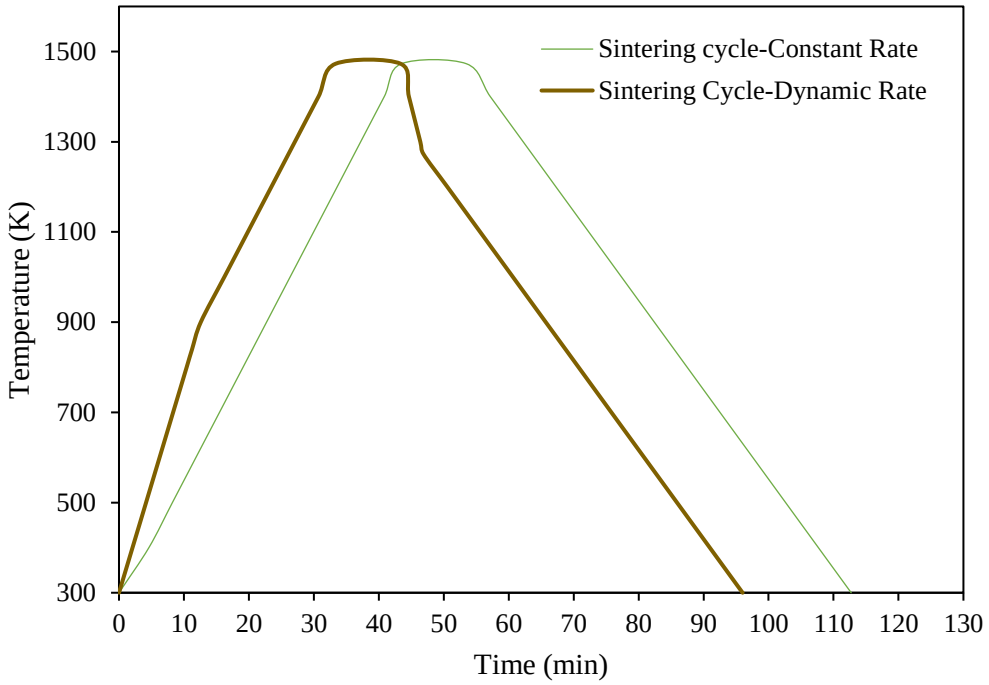

Figure 6.22: Optimum sintering cycle of ceramic tile-maximum sintering temperature 1200 ^{0}C

Table 6.2: SINTERING TIME VARIATION FOR DIFFERENT SINTERING CYCLE TYPE

Sintering Cycle Type	**Preheating Time (min)**	**Soaking Time (min)**	**Cooling Time (min)**	**Total Time (min)**	**Total Time Reduction w.r.t. Reference (%)**
Reference	260	30	410	700	-
Constant rate Cycle	43.48	10	59.24	112.72	83.8
Dynamic Rate Cycle	33.35	10	52.65	96.0	86.2

The linear shrinkage variation for optimum sintering cycles is shown in Table 6.3. The linear shrinkage values for the sintering cycles with constant rate and dynamic rate are 5.38% and 5.33%, respectively.

Table 6.3: LINEAR SHRINKAGE VARIATION OF CERAMIC TILE WITH OPTIMIZE SINTERING CYCLE

Sintering Cycle Type	**Reference**	**Constant Rate Cycle**	**Dynamic Rate Cycle**
Linear shrinkage (%)	7.4	5.38	5.33

The average MOR variation of heating and cooling stages of ceramic tile for optimum dynamic rate cycles and constant rate cycles is shown in Figures 6.23, 6.24, 6.25, and 6.26. The MOR increased with sintering temperature during the heating stage for both graphs. The decrease in the viscosity of the glassy phase during the heating stage caused the elastic characteristics of the ceramic body to weaken over time after 1110 ^{0}C. The ceramic body cools down and eventually regain its elastic properties. The glassy phase becomes more viscous at this period. Thus, as the cooling process begins, MOR increases, as shown in Figure 6.24.

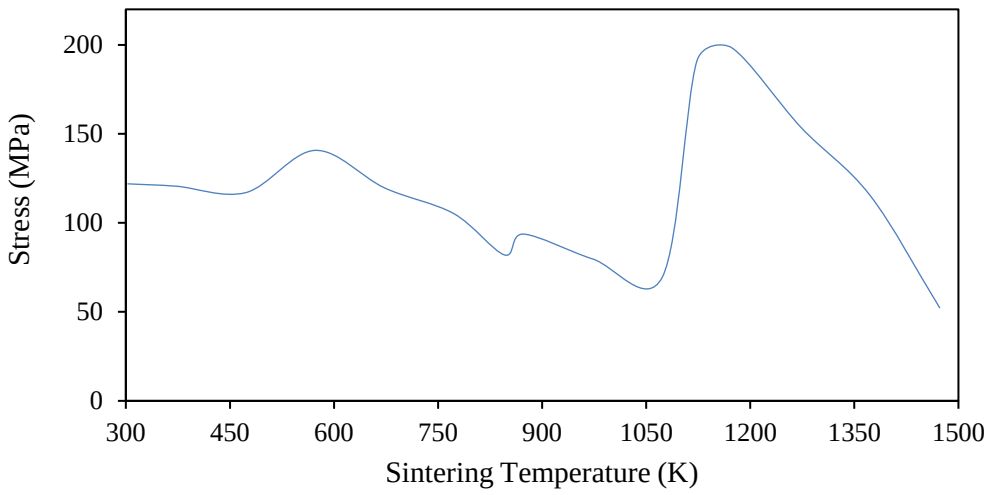

Figure 6.23: Average MOR variation of ceramic tile during cooling stage- Optimum dynamic rate cycle

The cooling rate affects the glassy phase retention time. The MOR of the ceramic tile developed as it started to cool, as shown in Figure 6.17(a). However, after a while, it abruptly dropped as a result of the ceramic tile body turning porcelain or solid. Figure 6.17(b) has a low cooling rate, and the MOR of the ceramic body is increased gradually.

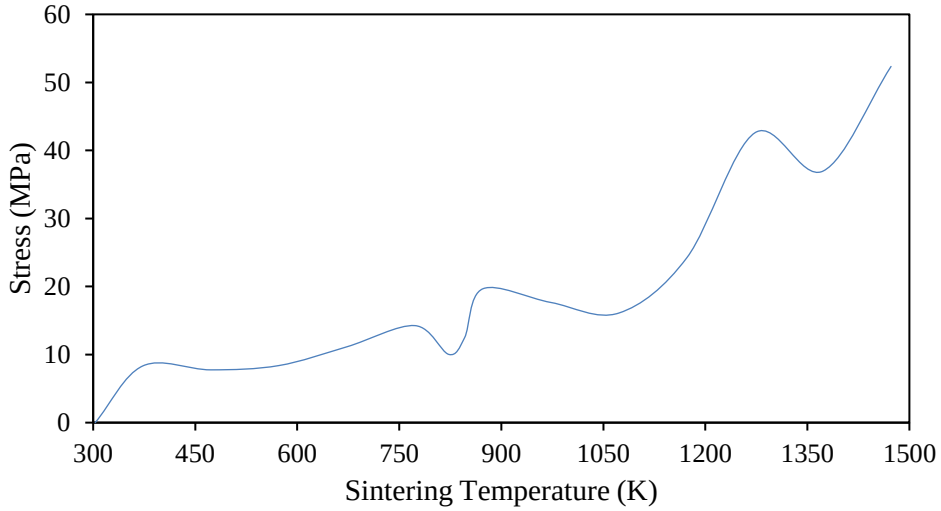

Figure 6.24: Average MOR variation of ceramic tile during heating stage- Optimum dynamic rate cycle

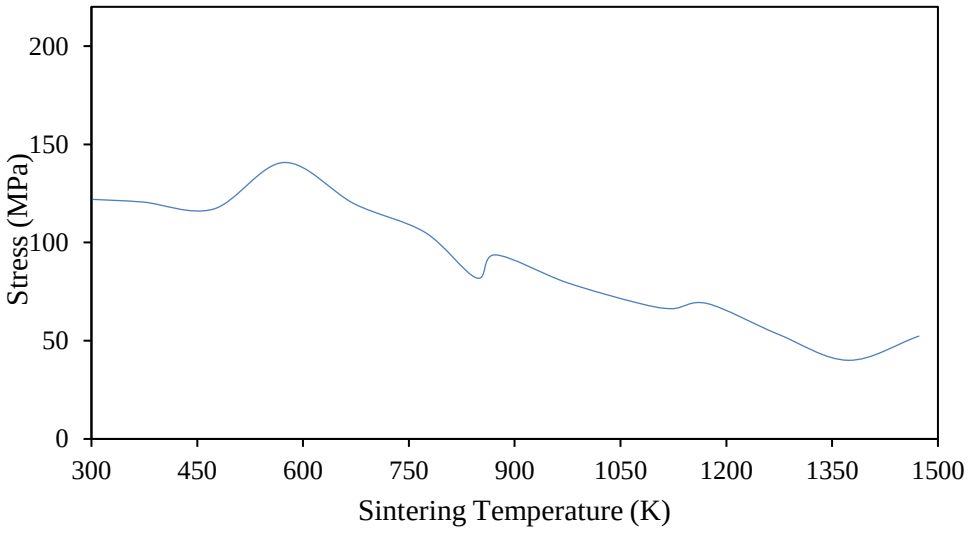

Figure 6.25: Average MOR variation of ceramic tile during cooling stage- Optimum constant rate cycle

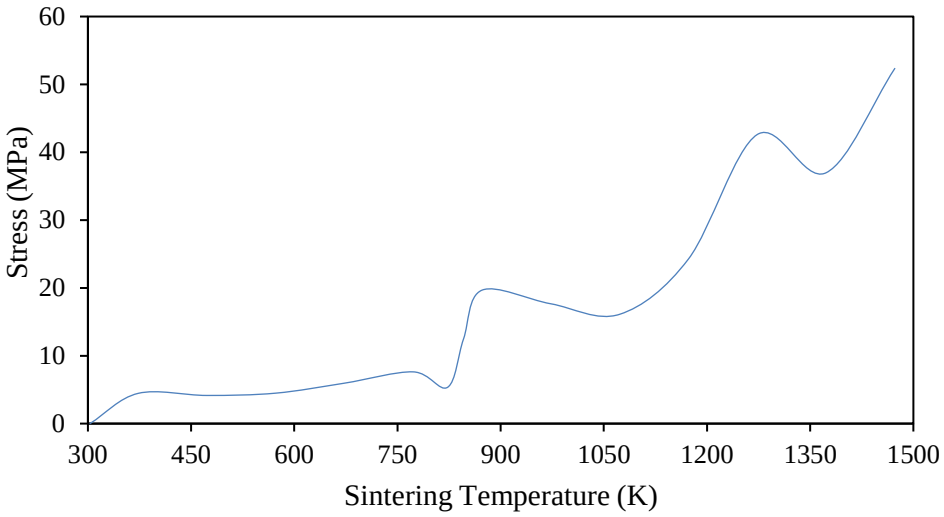

Figure 6.26: Average MOR variation of ceramic tile during heating stage-Optimum constant rate cycle

In this research, ceramic tile size 80×60×10 mm was used for only model validation. Geometry of the tile is a state parameter for the developed model. The physical and chemical transformation of the ceramic tile is independent of the size of the tile. The sintering temperature is a major factor in developing the linear shrinkage, MOR, and thermal stress of ceramic tile. In the sintering model, heat loss quantities are dependent on the surface area of the ceramic tile. When the dimension of the ceramic tile is increased, the temperature gradient throughout the ceramic tile is increased. Then the spatial and temporal variation of linear shrinkage, MOR, and thermal stress also increased. This tile size, 80×60×10 mm, was selected to match the UOM laboratory facility. The validated model can be utilized for any geometry of tile in the ceramic industry.

6.5. Utilize the Drying and Sintering Model in an Industrial Setting

The developed drying and sintering both models can be applied directly for industrial applications to produce ceramic tile by adhering to study findings on the body composition of ceramic tile. The drying temperature, packing density, and initial moisture content are main phase parameters for drying model. The packing density of the green ceramic tile can be determined experimentally, which depends on the particle size distribution of the body mix and powder pressing pressure. The initial moisture content and drying temperature can be changed based on the specific requirements of

the drying process. The main outcome of the drying model is the drying profile related to drying temperature. The CFD model of the drying process has the capability to find spatial variation of moisture exchange rate, and it is a great advantage for estimating the optimum drying temperature for minimum drying time by considering the spatial variation of moisture exchange rate of ceramic tile.

The sintering profile and density of ceramic tile are the main phase parameters in the sintering model. The sintering profile can be defined by the model user, and the user needs some knowledge regarding the ceramic tile sintering process. The density of the tile also can be determined experimentally. According to the size of the tile, the number of mesh and tile dimensions must be adjusted. The CFD model of the sintering process is capable of predicting the temporal and spatial changes in linear shrinkage, MOR, and thermal stress in ceramic tile during the sintering processes. The model is used to find the most appropriate sintering cycle for linear shrinkage and MOR. In the optimization of the sintering process, temporal and spatial changes in MOR and thermal stress of ceramic tile were obtained, and the optimum dynamic temperature profile for minimum sintering time was estimated using a developed sintering model.

Finally, the quality of the ceramic tile is improved, and the drying and sintering times of ceramic tile are reduced. The developed CFD models for the drying and sintering processes enhance the productivity of the ceramic tile industry. If those ceramic tile industries utilise distinct body compositions for this study, ceramic body composition-related parameters have to be taken into consideration, such as thermal conductivity, specific heat capacity, sintering parameters, and Young's modulus. One of the goals of this research was to estimate linear shrinkage, thermal stress, and MOR for ceramic tile bodies without experimental work, which is required in the ceramic industry. Further, this model can be used for different geometries of ceramic products with the same body composition as the industrial requirements. The geometry and meshing generation are required to be modified in the model.

CHAPTER 7

7. CONCLUSIONS, CONTRIBUTION TO KNOWLEDGE, LIMITATIONS AND RECOMMENDATION FOR FUTURE WORKS

7.1. Conclusions

The present research established a robust numerical model for the drying and sintering process of ceramic tiles using computational fluid dynamics (CFD). A numerical model was developed using FVM, and OpenFOAM is used as a model simulation program. Drying and sintering temperature are the main phase parameters for drying and sintering models, and drying temperature was constant and the sintering temperature varied with time. The CFD drying model facilitates finding the moisture variation of the ceramic tile body with drying temperature and time. The CFD model for the sintering process exhibits that there are temporal and spatial changes in temperature, linear shrinkage, and modulus of rupture of ceramic tiles.

To validate the developed model for ceramic tile bodies, M2 Kaolin was utilised as the major raw material for ceramic tile bodies. The green ceramic tile body mix contained quartz, kaolinite, feldspar, and dolomite. The main components of the body mix are 20% quartz, 30% clay with kaolinite and bentonite, 45% feldspar, and 5% dolomite. According to the chemical analysis, the total R2O (K2O + Na2O) and RO (CaO + MgO) contained in the green ceramic tile body mix are 5.59% and 3.75%, respectively. The loss on ignition (LOI) of the green ceramic tile body mix is 10.41%. M2 Kaolin particles spread between 0.05 and 16.32 µm, and the average size of the green body mix particle was 24.012 µm. Thermal characterisation of the green ceramic tile body mix by DTA and TGA confirmed that it contains quartz, kaolinite, and dolomite. XRD analysis and SEM-EDA analysis of sintered ceramic tiles confirmed that they contained mullite, quartz, and glassy phases. The moisture variation of green ceramic tile with time was determined. The linear shrinkage and MOR variation of each sintered tile was determined according to the ISO 13006 standard. The raw material preparation, body preparation, and sintering procedures adopted with the ceramic tiles for this research were comparable with existing techniques in the local tile industry. Therefore, based on this study, the developed body composition is recommended for the ceramic tile manufacturing industry in Sri Lanka.

A mathematical 3D model for the drying process was simulated using the effective moisture diffusion coefficient (D_m). The results of the developed model were validated and complied with experimental results with an R^2 value of 0.9.

The developed drying model was simulated with varying drying temperatures, and the moisture exchange rate variation of the green ceramic tile body was analysed using simulation results. It was confirmed that the maximum drying temperature of this ceramic tile is 180 °C. The optimum drying time of the green ceramic tile body was 60 minutes, and it was reduced by 72.6% of drying time compared to the reference sample. The created CFD drying model facilitates finding the drying profile related to drying temperature and the optimum drying cycle of ceramic tile without laboratory experimental effort.

The results obtained from the CFD sintering model and the experimental outcomes of linear shrinkage and MOR were compared. The simulated results of the linear shrinkage and MOR of the ceramic tiles was compiled to the value obtained experimentally. The simulated results of the established sintering model for ceramic tile were validated and complied with experimental results with an R^2 value of 0.9.

The CFD model of the sintering process is capable of predicting the temporal and spatial changes in linear shrinkage, MOR, and thermal stress in ceramic tile during the sintering processes. The model is used to find the most appropriate sintering cycle for linear shrinkage and MOR. In the optimization of the sintering process, temporal and spatial changes in MOR and thermal stress of ceramic tile were obtained, and the optimum dynamic temperature profile for minimum sintering time was estimated using a developed sintering model. It confirmed that the optimum sintering cycle included 51.6 °C/min heating rate between 30-550 °C, 27.6 °C/min heating rate between 550-1200 °C, 57.0 °C/min cooling rate between 1200-1000 °C, and 19.8 °C/min cooling between 1000-30 °C. The optimum sintering time was 96 minutes, and it was reduced by 82.6% of sintering time compared to the reference sample.

Finally, the quality of the ceramic tile is improved, and the drying and sintering times of ceramic tile are reduced. The developed CFD models for the drying and sintering processes enhance the productivity of the ceramic tile industry.

If those ceramic tile industries utilise distinct body compositions for this study, ceramic body composition-related parameters have to be taken into consideration. This

model can be applied to any dimension of ceramic tiles by changing main phase parameters such as drying temperature and sintering cycle. The suitable mesh development process according to the dimension of the tile needs to be done. Further, this model can be used for different geometries of ceramic products and different M2 Kaolin base body compositions of ceramic products by changing body composition-related parameters in the model. The geometry and meshing generation are required to be modified in the model.

One of the goals of this research was to estimate spatial and temporal variation of linear shrinkage, thermal stress and, MOR for ceramic products without experimental work, which is required in the ceramic industry. This same model can be utilized for different shapes of the ceramic body with M2 Kaolin base body composition with the industrial requirements.

7.2. Contribution to Knowledge

This research enhanced knowledge of both the drying and sintering processes of ceramic tile. This study developed a CFD model for the drying process, especially to examine the spatial variation of moisture and the moisture exchange rate within the green ceramic tile body with dying temperature and time. This approach offers a significant advantage in determining the optimum drying temperature for minimum drying time by accounting for the spatial differences in moisture exchange across the ceramic tile without laboratory experimental effort.

The CFD model developed in this study for the sintering process can predict the temporal and spatial changes in linear shrinkage, MOR, and thermal stress in ceramic tile through the sintering. The model is used to find the most appropriate sintering cycle for linear shrinkage and MOR. In optimising of the sintering process, temporal and spatial changes in MOR and thermal stress of ceramic tile were obtained, and the optimum dynamic temperature profile for minimum sintering time was estimated using a developed sintering model. This sintering model offers a significant advantage in determining the appropriate sintering cycle for linear shrinkage and MOR and, the optimum dynamic temperature profile of ceramic tile without laboratory experimental effort.

As a result, the quality of the ceramic tile is enhanced, and the drying and sintering times are reduced. The developed CFD models for the drying and sintering processes improve ceramic tile productivity.

7.3.Limitations and Recommendation for Future Works

In this study, the kinetics model related to MOR variation of sintering model is based on Kaolin materials, and it is the main limitation in this research. This kinetics model of MOR needs to be modified for all types of ceramic materials. Then the developed model can be applied to any type of body composition of ceramic product by changing body composition-related parameters in the model. This model does not include variation of physical and mechanical properties of ceramic tile with decoration code, and the model needs to be modified considering decoration code also. Then, this model can be applied directly to any geometry of products in the ceramic industry.

This research outcome provides recommendations for a developed drying and sintering model that can be applied to ceramic tile manufacturing industries. The developed sintering model can be used to find exact sintering cycles associated with linear shrinkage and MOR variation of ceramic tiles. The water absorption, fatigue strength, and thermal shock resistance variation are also the most important physical and mechanical properties for ceramic tiles. The developed sintering model can be modified by including kinetics models for water absorption, fatigue strength, etc. It is most applicable for the ceramics industry to improve the quality of the product.

The developed drying model can be modified by considering variations in drying shrinkage and dynamic state parameters. Managing the drying process is a significant challenge for the roofing tile industry in Sri Lanka and comparing the roofing tile industry to the ceramic tile industry, the forming process is entirely different. The initial drying stage of roofing tile has a moisture level of above 18%, and the drying process takes longer than five days. It is possible to optimize the drying profile of roofing tiles by modifying the drying model that was created for ceramic tiles to take roofing tiles into account.

The future work related to the drying and sintering model was focused on industrial applications, and it was a great help improving the quality and productivity of ceramic products. Consequently, the ceramic industry's production costs have decreased.

SPECIFIC NOMENCLATURE

$T_{,D}$ Drying temperature of green ceramic body (K)

D_m Moisture diffusion coefficients green ceramic body (m^2/s)

ρ_D Bulk density of green ceramic body (kg/m^3)

D_0 The variable dimensional parameter depends on bulk density (m^2/s)

b, r, Constant

$\theta_{k,}\ \theta_D$ Constant (K)

a_D , b_D Constant

$T_{,D}$ Drying temperature of green ceramic body (K)

$T_{,D,S}$ Drying temperature of green ceramic body surface (K)

$T_{,D,S}$ Drying air temperature (K)

m_D Moisture content of green ceramic body (kg/m^3)

$m_{D,s}$ Moisture content of ceramic body surface (kg/m^3)

$m_{D,e}$ Equilibrium moisture content of green ceramic body with the surrounding air (kg/m^3)

m_v Vaporized Moisture content from green ceramic body (kg/m^3)

$C_{p,D}$ Heat capacities of green ceramic body (J/(kg.K))

K_D Thermal diffusion coefficients green ceramic body (W/(m.K))

ρ_D Bulk density of green ceramic body (kg/m^3)

G_E Source term for drying process ($J/(m^3.s)$)

γ Latent heat of water (J/kg)

k_0 Constant (1/s)

J_D Moisture diffusion rate green ceramic body (kg/s)

α Moisture exchange coefficient (m/s)

$R_{,i}$ Reaction rates of each transformation (kg/s)

A_i Pre-exponential factor (1/s)

E_i Activation energy (J/mol)

$Q_{heat\ of\ reaction,i}$ Heat of each transformation ($J/(m^3.s)$)

Δh_i Enthalpy of each reaction (J/kg)

$Q_{convection}$ Source term for convection ($J/(m^3.s)$)

$Q_{radiation}$ Source term for radiation ($J/(m^3.s)$)

h_{con} Conversion heat transfer coefficient ($W/(m^2.K)$)

h_{rad} Radiative heat transfer coefficient ($W/(m^2.K)$)

A_S Particle surface area (m^2)

D_S Surface area based mean diameter (μm)

T_g Gas phase temperature (K)

T_s Solid phase temperature (K)

ε_m Wall emissivity

σ Stefan-Boltzmann constant ($W.m/K^4$)

u_g Gas phase velocity (m/s)

p Gas pressure (Pa)

S_R Gas flow resistance

K_{tile} Permeability of tile

Y_{tile} Mass fraction of tile.

$C_{p;g}$ Specific heat capacity of gas phase (J /(kg.K))

$C_{p;s}$ Specific heat capacity of solid phase (J/(kg.K))

ρ_g Density of gas phase (kg/m^3)

ρ_s Density of solid phase (kg/m^3)

k_g Thermal conductivity of gas phases (W/(m.K))

k_s Thermal conductivity of solid phases (W/(m.K))

$m_{i;g}$ Mass variation of gas phase (kg)

$D_{i;g}$ Gas diffusion coefficient (m^2/s)

M_{air} Molecular weight of air (kg/mol)

M_s Molecular weight of solid phase (kg/mol)

σ_i Average collision diameter (Å)

Ω_i Diffusion collision integral

ε Porosity of the ceramic materials

η_s Viscosity of liquid phase (Pa.s)

P_c Capillary pressure (Pa)

γ Glassy phase surface tension (mN/m)

r Radius of porous (μm)

k_0 Frequency factor

E_A Activation energy for shrinkage (J/mol)

t_s Sintering time (s)

n Sintering factor

$\sigma_{F\_C\_heating}$ Fracture strength of ceramic tile during heating (N/m^2)

$\sigma_{F\_C\_cooling}$ Fracture strength of ceramic tile during cooling (N/m^2)

$\sigma_{F\_G\_cooling}$ Fracture strength of glassy phase during cooling (N/m^2)

$\sigma_{thermal,heating}$ Thermal stress of quartz during heating (N/m^2)

$\sigma_{thermal,cooling}$ Thermal stress of quartz during cooling (N/m^2)

$\sigma_{max,\ fired}$ Maximum stress of fired ceramic tile (N/m^2)

E_{fired} Young's modulus of tile after fired (N/m^2)

$E_{C\_heating}$ Young's modulus of tile during heating (N/m^2)

$E_{C\_cooling}$ Young's modulus of tile during cooling (N/m^2)

$E_{Q\_heating}$ Young's modulus of quartz during heating (Nm^{-2})

$E_{Q\_cooling}$ Young's modulus of quartz during cooling (N/m^2)

$\alpha_{C\_heating}$ Coefficient of Linear Thermal Expansion of tile during heating (1/K)

$\alpha_{C\_cooling}$ Coefficient of Linear Thermal Expansion of tile during cooling (1/K)

$\alpha_{Q\_heating}$ Coefficient of Linear Thermal Expansion of quartz during heating (1/K)

$\alpha_{Q\_cooling}$ Coefficient of Linear Thermal Expansion of quartz during cooling (1/K)

$\mu_{C\_heating}$ Poisson's ratio of tile during heating

$\mu_{C\_cooling}$ Poisson's ratio of tile during cooling

$\mu_{Q\_heating}$ Poisson's ratio of quartz during heating

$\mu_{Q\_cooling}$ Poisson's ratio of quartz during cooling

$\lambda_{C\_heating}$ Thermal conductivity of ceramic tile body during heating (W/(m.K))

$\lambda_{C\_cooling}$ Thermal conductivity of ceramic tile body during cooling (W/(m.K))

$C_{C\_heating}$ Specific heat capacity of ceramic tile body during heating (J/(kg.K))

$C_{C\_cooling}$ Specific heat capacity of ceramic tile body during cooling (J/(kg.K))

k Curvature of ceramic tile during the deflection (m)

h Deflection in the Centre of the ceramic tile (m)

L Length of the ceramic tile (m)

t Thickness of the ceramic tile (m)

H_r Ceramic tile heating rate ($^0C/s$)

C_r Ceramic tile cooling rate ($^0C/s$)

A Shape factor of the ceramic tile body

r Characteristic dimension of the tile body during heating or cooling (m)

ρ Density of ceramic tile body during heating or cooling (kg/m^3)

REFERENCES

[1] "Statics World Production and Consumption of Ceramic Tiles.", Association of Italian Manufactures of Machinery and Equipment for ceramic, 2015.

[2] E. V. Romera, F. Xavier and M. Morales, "CURRENT AND FUTURE CHALLENGES OF THE CERAMIC TILE FIRMS (The case of the INKJET technological innovation) Final Year Project (6 credits)".

[3] Hassanein A. Refaey , E. Specht , M.R.Salem, 'Influence of fuel distribution and heat transfer on energy consumption in tunnel kilns' , *International Journal of Advances in Engineering & Technology*, June, 2015

[4] S.H. Jazayeri, A. salem, G. timellini, E. rastelli, 'A kinetic study on the development of porosity in porcelain stoneware tile sintering' , Bol. Soc. Esp. Ceram, V., 46 [1] 1-6 (2007)

[5] M. Romero and J. M. Pérez, "Relation between the microstructure and technological properties of porcelain stoneware. A review," Materiales de Construcción, vol. 65, no. 320, p. e065, Oct. 2015, doi: https://doi.org/10.3989/mc.2015.05915.

[6] J. Martín-Márquez, J. Ma. Rincón, and M. Romero, "Effect of firing temperature on sintering of porcelain stoneware tiles," Ceramics International, vol. 34, no. 8, pp. 1867–1873, Dec. 2008, doi: https://doi.org/10.1016/j.ceramint.2007.06.006.

[7] J. L. Amorós, M. J. Orts, J. García-Ten, A. Gozalbo, and E. Sánchez, "Effect of the green porous texture on porcelain tile properties," Journal of the European Ceramic Society, vol. 27, no. 5, pp. 2295–2301, Jan. 2007, doi: https://doi.org/10.1016/j.jeurceramsoc.2006.07.005.

[8] J. M. Pérez and M. Romero, "Microstructure and technological properties of porcelain stoneware tiles moulded at different pressures and thicknesses," Ceramics International, vol. 40, no. 1, pp. 1365–1377, Jan. 2014, doi: https://doi.org/10.1016/j.ceramint.2013.07.018.

[9] K. E. Atcholi, E. Padayodi, J. C. Sagot, T. Beda, O. Samah, and J. Vantomme, "Thermo-mechanical behaviour of the structures of tropical clays from Togo (West Africa) fired at 500 °c, 850 °c and 1060 °c," Construction and Building Materials, vol. 27, no. 1, pp. 141–148, Feb. 2012, doi: 10.1016/j.conbuildmat.2011.08.009.

[10] G. C. Stangle and I. A. Aksay, "Simultaneous momentum, heat and mass transfer with chemical reaction in a disordered porous medium: application to binder removal from a ceramic green body," Chemical Engineering Science, vol. 45, no. 7, pp. 1719–1731, Jan. 1990, doi: https://doi.org/10.1016/0009-2509(90)87050-3.

[11] K. Murugesan, K. N. Seetharamu, and A. Narayana, "A one dimensional analysis of convective drying of porous materials," Heat and mass transfer, vol. 32, no. 1–2, pp. 81–88, Nov. 1996, doi: https://doi.org/10.1007/s002310050095.

[12] S. Messai, J. Sghaier, D. Lecomte, and A. Belghith, "Drying Kinetics of a Porous Spherical Particle and the Inversion Temperature," Drying Technology, vol. 26, no. 2, pp. 157–167, Jan. 2008, doi: https://doi.org/10.1080/07373930701831127.

[13] H. Suresh, K. Murugesan, P. Narayana, and K. Seetharamu, "DRYING OF POROUS MATERIAL USING FINITE ELEMENT METHOD," presented at the Second International Conference on CFD in the Minerals and process Industries, 1999. Accessed: Jun. 08, 2024. [Online]. Available: https://www.cfd.com.au/cfd_conf99/Conf99_Papers/008SURE.PDF

[14] K. Khalili, M. Bagherian, and S. Khisheh, "Numerical Simulation of Drying Ceramic Using Finite Element and Machine Vision," Procedia technology, vol. 12, pp. 388–393, Jan. 2014, doi: https://doi.org/10.1016/j.protcy.2013.12.504.

[15] J. C. Jarque, C. Segarra, V. Cantavella, and R. Mondragón, "Non-isothermal modeling of drying kinetics of ceramic tiles," Drying Technology, vol. 34, no. 7, pp. 761–772, Aug. 2015, doi: https://doi.org/10.1080/07373937.2015.1076837.

[16] A.-D. la, A.M. Guzmán, C. Gómez-Rodríguez, D.I. Martínez, and N. Elizondo, "Influence of Al2O3 and SiO2 nanoparticles addition on the microstructure and mechano-physical properties of ceramic tiles," Ceramics International, vol. 48, no. 9, pp. 12712–12720, May 2022, doi: https://doi.org/10.1016/j.ceramint.2022.01.140.

[17] F. Güngör and N. Ay, “The effect of particle size of body components on the processing parameters of semi transparent porcelain,” Ceramics International, vol. 44, no. 9, pp. 10611–10620, Jun. 2018, doi: https://doi.org/10.1016/j.ceramint.2018.03.086.
[18] A. J. Souza, A. Pinheiro, and F. Hol, “Sintering Behavior of Vitrified Ceramic Tiles Incorporated with Petroleum Waste,” InTech eBooks, Feb. 2013, doi: https://doi.org/10.5772/53256.
[19] D. Antal, Tomáš Húlan, Igor Štubňa, M. Záleská, and A. Trník, “The influence of texture on elastic and thermophysical properties of kaolin- and illite-based ceramic bodies,” Ceramics International, vol. 43, no. 2, pp. 2730–2736, Feb. 2017, doi: https://doi.org/10.1016/j.ceramint.2016.11.100.
[20] Kornelia Wiśniewska, Waldemar Pichór, and E Kłosek-Wawrzyn, “Impact of the addition of dolomite to cream-firing clays on the technological and color properties of sintered ceramics,” International Journal of Applied Ceramic Technology, vol. 18, no. 3, pp. 1063–1073, Feb. 2021, doi: https://doi.org/10.1111/ijac.13719.
[21] M. Dal Bó, L. Dominguini, A. Zimmer, S. R. Grando, P. Kaspari, and D. Hotza, “Chemical tempering of porcelain tiles,” Ceramics International, vol. 42, no. 14, pp. 15199–15202, Nov. 2016, doi: https://doi.org/10.1016/j.ceramint.2016.06.138.
[22] J. García Ten, M. J. Orts, A. Saburit, and G. Silva, “Thermal conductivity of traditional ceramics. Part I: Influence of bulk density and firing temperature,” Ceramics International, vol. 36, no. 6, pp. 1951–1959, Aug. 2010, doi: https://doi.org/10.1016/j.ceramint.2010.05.012.
[23] C. Zanelli, M. Raimondo, G. Guarini, and M. Dondi, “The vitreous phase of porcelain stoneware: Composition, evolution during sintering and physical properties,” Journal of Non-Crystalline Solids, vol. 357, no. 16–17, pp. 3251–3260, Aug. 2011, doi: 10.1016/j.jnoncrysol.2011.05.020.
[24] E. Garzón, L. Pérez-Villarejo, D. Eliche-Quesada, S. Martínez-Martínez, and P. J. Sánchez-Soto, “Vitrification rate and estimation of the optimum firing conditions of ceramic materials from raw clays: A review,” Ceramics International, vol. 48, no. 11, pp. 15889–15898, Jun. 2022, doi: 10.1016/j.ceramint.2022.02.129.
[25] Abdelaziz Elgamouz, Najib Tijani, I. Shehadi, Md. Kamrul Hasan, and Mohamad Al-Farooq Kawam, “Characterization of the firing behaviour of an illite-kaolinite clay mineral and its potential use as membrane support,” Heliyon, vol. 5, no. 8, pp. e02281–e02281, Aug. 2019, doi: https://doi.org/10.1016/j.heliyon.2019.e02281.
[26] S. A. T. Redfern, “The kinetics of dehydroxylation of kaolinite,” Clay Minerals, vol. 22, no. 4, pp. 447–456, Dec. 1987, doi: https://doi.org/10.1180/claymin.1987.022.4.08.
[27] D. V. Andreev and A. I. Zakharov, “Ceramic item deformation during firing: effects of composition and microstructure (review),” Refract Ind Ceram, vol. 50, no. 4, pp. 298–303, Jul. 2009, doi: 10.1007/s11148-009-9191-y
[28] M. J. Orts, J.L. Amorós, A. Escardino, A. Gozalbo, and C. Feliu, “Kinetic model for the isothermal sintering of low porosity floor tiles,” Applied Clay Science, vol. 8, no. 2–3, pp. 231–245, Aug. 1993, doi: https://doi.org/10.1016/0169-1317(93)90040-8.
[29] M. J. Orts, A. Escardino, J. L. Amorós, and F. Negre, “Microstructural changes during the firing of stoneware floor tiles,” Applied Clay Science, vol. 8, no. 2–3, pp. 193–205, Aug. 1993, doi: https://doi.org/10.1016/0169-1317(93)90037-2.
[30] W. Zeng, L. Gao, L. Gui, and J. Guo, “Sintering kinetics of α-Al2O3 powder,” Ceramics International, vol. 25, no. 8, pp. 723–726, Dec. 1999, doi: https://doi.org/10.1016/s0272-8842(99)00008-5.
[31] S. Yürüyen and H. Ö. Toplan, “The sintering kinetics of porcelain bodies made from waste glass and fly ash,” Ceramics International, vol. 35, no. 6, pp. 2427–2433, Aug. 2009, doi: https://doi.org/10.1016/j.ceramint.2009.02.005.
[32] A. Salem, S. H. Jazayeri, E. Rastelli, and G. Timellini, “Dilatometeric study of shrinkage during sintering process for porcelain stoneware body in presence of nepheline syenite,” Journal of Materials Processing Technology, vol. 209, no. 3, pp. 1240–1246, Feb. 2009, doi: https://doi.org/10.1016/j.jmatprotec.2008.03.033.

[33] A. Salem, S. H. Jazayeri, E. Rastelli, and G. Timellini, “Kinetic model for isothermal sintering of porcelain stoneware body in presence of nepheline syenite,” Thermochimica Acta, vol. 503–504, pp. 1–7, May 2010, doi: https://doi.org/10.1016/j.tca.2010.01.024.

[34] M. Cargnin, S. M. A. G. Ulson de Souza, A. A. Ulson de Souza, and A. De Noni Jr., “MODELING AND SIMULATION OF THE EFFECT OF THE FIRING CURVE ON THE LINEAR SHRINKAGE OF CERAMIC MATERIALS: LABORATORY SCALE AND INDUSTRIAL SCALE,” Brazilian Journal of Chemical Engineering, vol. 32, no. 2, pp. 433–443, Jun. 2015, doi: 10.1590/0104-6632.20150322s00002876.

[35] S. Conte, C. Zanelli, M. Ardit, G. Cruciani, and M. Dondi, “Predicting Viscosity and Surface Tension at High Temperature of Porcelain Stoneware Bodies: A Methodological Approach,” Materials, vol. 11, no. 12, p. 2475, Dec. 2018, doi: https://doi.org/10.3390/ma11122475.

[36] Igor Stubna, A. Trnik, F. Chmelik, and L. Vozar, “Mechanical Properties of Kaolin-Base Ceramics During Firing,” InTech eBooks, Aug. 2011, doi: https://doi.org/10.5772/19199.

[37] J. M. N. Jayaweera, M. Narayana, and S. U. Adikary, “Numerical Modeling of Drying Behavior of Ceramic Tiles with High Silica Content of Kaolin,” in 2023 Moratuwa Engineering Research Conference (MERCon), Moratuwa, Sri Lanka: IEEE, Nov. 2023, pp. 592-597. doi: https://doi.org/10.1109/mercon60487.2023.10355459 .

[38] J. M. N. Jayaweera, M. Narayana, and S. U. Adikary, “Effects of Kaolin with High Silica Content on Properties of Ceramic Tiles,” in 2022 Moratuwa Engineering Research Conference (MERCon), Moratuwa, Sri Lanka: IEEE, Jul. 2022, pp. 1–6. doi: 10.1109/MERCon55799.2022.9906261.

[39] H. A. Refaey, E. Specht, and M. R. Salem, “INFLUENCE OF FUEL DISTRIBUTION AND HEAT TRANSFER ON ENERGY CONSUMPTION IN TUNNEL KILNS,” International Journal of Advances in Engineering & Technology, vol. 8, no. 3, Jun. 2015.

[40] S. Ferrer, A. Mezquita, M. P. Gomez-Tena, C. Machi, and E. Monfort, “Estimation of the heat of reaction in traditional ceramic compositions,” Applied Clay Science, vol. 108, pp. 28–39, May 2015, doi: https://doi.org/10.1016/j.clay.2015.02.019.

[41] H. K. Versteeg and W Malalasekera, An introduction to computational fluid dynamics : the finite volume method. Harlow: Pearson Education, 2011.

[42] F Moukalled, L Mangani, and M Darwish, The Finite Volume Method in Computational Fluid Dynamics An Advanced Introduction with OpenFOAM® and Matlab. Cham Springer International Publishing, 2016.

[43] V. D. Thi, M. Li, M. Khelifa, M. El Ganaoui, and Y. Rogaume, “Finite Element Modeling of Heat and Moisture Transfer in Porous Material,” International Journal of Materials and Metallurgical Engineering , vol. 11, no. 4, 2017.

[44] Ante Sikirica, Luka Grbčić, M. Alvir, and Lado Kranjčević, “Computational Efficiency Assessment of Adaptive Mesh Refinement for Turbulent Jets in Crossflow,” Mathematics, vol. 10, no. 4, pp. 620–620, Feb. 2022, doi: https://doi.org/10.3390/math10040620.

[45] R. Mondragón, J. E. Juliá, L. Hernández, and J. C. Jarque, “Modeling of Drying Curves of Silica Nanofluid Droplets Dried in an Acoustic Levitator Using the Reaction Engineering Approach (REA) Model,” Drying Technology, vol. 31, no. 4, pp. 439–451, Mar. 2013, doi: https://doi.org/10.1080/07373937.2012.738753.

[46] C. Jung, J.-R. Kim, and S. Yi, “Two-dimensional simulation of silica gel drying using computational fluid dynamics,” Journal of Ceramic Processing Research, vol. 9, no. 2, pp. 184–188, Apr. 2008, doi: https://doi.org/10.36410/jcpr.2008.9.2.184.

[47] S. Mahmoudi, E. Srasra, and F. Zargouni, “SIMULTANEOUS OPTIMISATION OF DRYING PARAMETERS OF CERAMIC BODIES,” American Journal of Geoscience, vol. 4, no. 1, pp. 1–7, Jan. 2014, doi: 10.3844/ajgsp.2014.1.7.

[48] Lauro, N., Oummadi, S., Alzina, A., Nait-Ali, B., & Smith, D. S. (2021). Computer model of drying behaviour of ceramic green bodies with particular reference to moisture content dependent properties. Journal of the European Ceramic Society, 41(14), 7321–7329. doi:10.1016/j.jeurceramsoc.2021.0

[49] G. MUSIELAK, T. SLIWA, and M. STASIAK, “NUMERICAL MODELLING OF EFFECTS OF THE DRYING RATE ON KAOLIN FRACTURING,” CERAMIC MATERIALS, vol. 65, pp. 61–64, 2013.
[50] J. Barbosa da Silva, G. S. Almeida, W. C. P. Barbosa de Lima, G. A. Neves, and A. G. B. de Lima, “Heat and Mass Diffusion Including Shrinkage and Hygrothermal Stress during Drying of Holed Ceramics Bricks,” Defect and Diffusion Forum, vol. 312–315, pp. 971–976, Apr. 2011, doi: 10.4028/www.scientific.net/ddf.312-315.971.
[51] M. Hassanein, A. Mohsen, and H. Refaey, “Mathematical Model to Analyze the Heat Transfer in Tunnel Kilns for Burning of Ceramics,” 1978. Accessed: Dec. 14, 2023. [Online]. Available: https://core.ac.uk/download/pdf/51448507.pdf
[52] H. Refaey, M. Karali, A. Al-Hasnawi, and E. Specht, “MATHEMATICAL MODEL TO SIMULATE THE HEAT TRANSFER IN VITRIFIED CLAY PIPES KILN,” The International Conference on Applied Mechanics and Mechanical Engineering, vol. 18, no. 18, pp. 1–12, Apr. 2018, doi: 10.21608/amme.2018.34989.
[53] S. Salem and A. Salem, “Mechanisms of Momentum Transport in Viscous Flow Sintering,” Sintering Applications, Feb. 2013, doi: https://doi.org/10.5772/53259.
[54] C. Zanelli, M. Raimondo?', M. Dondi, G. Guarini?', and P. Cavalcante'", “SINTERING MECHANISMS OF PORCELAIN STONEWARE TILES,” 2004. Accessed: Dec. 16, 2023. [Online]. Available: https://www.qualicer.org/recopilatorio/ponencias/pdfs/0413191e.pdf
[55] Muhammad Shoaib Anwar, “Heat transfer in MHD convective stagnation point flow over a stretching surface with thermal radiations,” Numerical heat transfer. Part A. Applications/Numerical heat transfer. Part A, Applications, pp. 1–16, Jan. 2024, doi: https://doi.org/10.1080/10407782.2023.2299289.
[56] H. S. Ko, Y. H. Bae, and I. H. Cho, “DYNAMIC ANALYSIS OF A FLOATING STRUCTURE USING OPENFOAM,” Journal of Computational Fluids Engineering, vol. 23, no. 1, pp. 101–112, Mar. 2018, doi: https://doi.org/10.6112/kscfe.2018.23.1.101.
[57] M. Gómez-Tena, J. Gilabert, J. Toledo, E. Zumaquero, and C. Machí, “CASTELLÓN (ESPAÑA) RELATIONSHIP BETWEEN THE SPECIFIC SURFACE AREA PARAMETERS DETERMINED USING DIFFERENT ANALYTICAL TECHNIQUES.” Available:https://www.qualicer.org/recopilatorio/ponencias/pdfs/56%20POSTER%20ING.pdf
[58] D. Llorens, “temperature Distribution insiDe a ceramic tiLe During inDustriaL firing,” 2006. Accessed: Dec. 14, 2022. [Online]. Available: https://www.qualicer.org/recopilatorio/ponencias/pdfs/0062312e.pdf
[59] Ján Ondruška et al., “Thermophysical Properties of Kaolin–Zeolite Blends up to 1100 °C,” Crystals, vol. 11, no. 2, pp. 165–165, Feb. 2021, doi: https://doi.org/10.3390/cryst11020165.
[60] R.B. Bird, W.E. Stewart, E.N. Lightfoot, Transport Phenomena, second ed., 2002,https://doi.org/10.1002/aic.690070245.
[61] S. Salem and A. Salem, “Mechanisms of Momentum Transport in Viscous Flow Sintering,” Sintering Applications, Feb. 2013, doi: https://doi.org/10.5772/53259.
[62] T. Húlan et al., “Young’s Modulus of Different Illitic Clays during Heating and Cooling Stage of Firing,” Materials, vol. 13, no. 21, p. 4968, Nov. 2020, doi: https://doi.org/10.3390/ma13214968.
[63] S. L. Correia, K. A. S. Curto, D. Hotza, and A. M. Segadães, “Using Experiments Design to Model Linear Firing Shrinkage of Triaxial Ceramic Bodies,” Materials Science Forum, vol. 498–499, pp. 430–435, Nov. 2005, doi: https://doi.org/10.4028/www.scientific.net/msf.498-499.430.
[64] A. Elimbi, J. M. Dika, and C. N. Djangang, “Effects of Alkaline Additives on the Thermal Behavior and Properties of Cameroonian Poorly Fluxing Clay Ceramics,” Journal of Minerals and Materials Characterization and Engineering, vol. 02, no. 05, pp. 484–501, Jan. 2014, doi: https://doi.org/10.4236/jmmce.2014.25049.

[65] V.-G. Lee and T.-H. Yeh, “Sintering effects on the development of mechanical properties of fired clay ceramics,” Materials Science and Engineering: A, vol. 485, no. 1–2, pp. 5–13, Jun. 2008, doi: 10.1016/j.msea.2007.07.068.
[66] I. Stubna, A. Trnik, F. Chmelik, and L. Vozar, “Mechanical Properties of Kaolin-Base Ceramics During Firing,” in Advances in Ceramics - Characterization, Raw Materials, Processing, Properties, Degradation and Healing, C. Sikalidis, Ed., InTech, 2011. doi: 10.5772/19199.
[67] P. Šín, R. Podoba, I. Štubňa, and A. Trník, “Mechanical properties of alumina porcelain during heating,” presented at the TIM 2013 PHYSICS CONFERENCE, Timisoara, Romania, 2014, pp. 76–80. doi: 10.1063/1.4903017.
[68] A. Elimbi, J. M. Dika, and C. N. Djangang, “Effects of Alkaline Additives on the Thermal Behavior and Properties of Cameroonian Poorly Fluxing Clay Ceramics,” *Journal of Minerals and Materials Characterization and Engineering*, vol. 02, no. 05, pp. 484–501, Jan. 2014, doi: https://doi.org/10.4236/jmmce.2014.25049.
[69] P. P. Parlevliet, H. E. N. Bersee, and A. Beukers, “Residual stresses in thermoplastic composites—A study of the literature—Part II: Experimental techniques,” Composites Part A: Applied Science and Manufacturing, vol. 38, no. 3, pp. 651–665, Mar. 2007, doi: https://doi.org/10.1016/j.compositesa.2006.07.002.
[70] “The TCNA Handbook for Ceramic, Glass and Stone Tile Installation,” www.ceramictilefoundation.org, Sep. 01, 2020. https://www.ceramictilefoundation.org/blog/tcna-handbook
[71] P. K. Panda, T. S. Kannan, J. Dubois, C. Olagnon, and G. Fantozzi, “Thermal shock and thermal fatigue study of ceramic materials on a newly developed ascending thermal shock test equipment,” Science and Technology of Advanced Materials, vol. 3, no. 4, pp. 327–334, Jan. 2002, doi: https://doi.org/10.1016/s1468-6996(02)00029-3.
[72] S. Jazayeri, A. Salem, Timellini, and Rastelli, “Cerámica y Vidrio A kinetic study on the development of porosity in porcelain stoneware tile sintering,” Feb. 2007. Accessed: Feb. 28, 2024. [Online]. Available: https://boletines.secv.es/upload/20070113132809.46%5B1%5D1-6.pdf
[73] V.-G. Lee and T.-H. Yeh, “Sintering effects on the development of mechanical properties of fired clay ceramics,” Materials Science and Engineering: A, vol. 485, no. 1–2, pp. 5–13, Jun. 2008, doi: https://doi.org/10.1016/j.msea.2007.07.068.
[74] P. Šín, R. Podoba, Igor Štubňa, and A. Trník, “Mechanical properties of alumina porcelain during heating,” Nucleation and Atmospheric Aerosols, Jan. 2014, doi: https://doi.org/10.1063/1.4903017.
[75] T. Húlan et al., “Young’s Modulus of Different Illitic Clays during Heating and Cooling Stage of Firing,” Materials, vol. 13, no. 21, p. 4968, Nov. 2020, doi: https://doi.org/10.3390/ma13214968.
[76] A. Vojtko , P. Šín , and I. Štubňa, “POISSON’S RATIO OF KAOLIN CERAMICS AS A FUNCTION OF FIRING TEMPERATURE,” in Material – Acoustics , 2011.
[77] E. Eren Gültekin, “The effect of heating rate and sintering temperature on the elastic modulus of porcelain tiles,” Ultrasonics, vol. 83, pp. 120–125, Feb. 2018, doi: https://doi.org/10.1016/j.ultras.2017.06.005.
[78] A. Elimbi, J. M. Dika, and C. N. Djangang, “Effects of Alkaline Additives on the Thermal Behavior and Properties of Cameroonian Poorly Fluxing Clay Ceramics,” Journal of Minerals and Materials Characterization and Engineering, vol. 02, no. 05, pp. 484–501, Jan. 2014, doi: https://doi.org/10.4236/jmmce.2014.25049.
[79] Martín-Márquez, J. Ma. Rincón, and M. Romero, “Mullite development on firing in porcelain stoneware bodies,” Journal of the European Ceramic Society, vol. 30, no. 7, pp. 1599–1607, May 2010, doi: https://doi.org/10.1016/j.jeurceramsoc.2010.01.002.
[80] A. D. Pekdemir, Y. Sarıkaya, and M. Önal, “Thermal transformation kinetics of a kaolinitic clay,” Journal of Thermal Analysis and Calorimetry, vol. 123, no. 1, pp. 767–772, Jul. 2015, doi: https://doi.org/10.1007/s10973-015-4866-8.

[81] B. F. Rangel, M. M. Viana, M. V. A. Fonseca, J. Dweck, and L. M. Tavares, “Thermal characterization of a new green ceramic material by heating microscopy, thermogravimetry and differential thermal analysis,” Journal of Thermal Analysis and Calorimetry, vol. 121, no. 1, pp. 115–125, Jul. 2015, doi: 10.1007/s10973-015-4496-1.
[82] M. S. Conconi, M. Morosi, J. Maggi, P. E. Zalba, F. Cravero, and N. M. Rendtorff, “Thermal behavior (TG-DTA-TMA), sintering and properties of a kaolinitic clay from Buenos Aires Province, Argentina,” Ceramica, vol. 65, no. 374, pp. 227–235, 2019, doi: 10.1590/0366-69132019653742621.
[83] S. A. T. Redfern, “The kinetics of dehydroxylation of kaolinite,” Clay Minerals, vol. 22, no. 4, pp. 447–456, Dec. 1987, doi: https://doi.org/10.1180/claymin.1987.022.4.08.
[84] I. Hammouda and D. Mihoubi, “Thermodynamic and mechanical characterisation of kaolin clay,” Polish Journal of Chemical Technology, vol. 16, no. 1, pp. 28–35, 2014, doi: 10.2478/pjct-2014-0005.
[85] O. Castelein, B. Soulestin, J. P. Bonnet, and Philippe Blanchart, “The influence of heating rate on the thermal behaviour and mullite formation from a kaolin raw material,” Ceramics International, vol. 27, no. 5, pp. 517–522, Jan. 2001, doi: https://doi.org/10.1016/s0272-8842(00)00110-3.
[86] Hayward and A. Arbor, “Hysteresis upon Repeated Cycling through the Beta-Alpha Cristobalite Transformation,” Journal of Ceramic Science and Technology, vol. 6, no. 1, pp. 55–62, Jan. 2014, doi: https://doi.org/10.4416/jcst2014-00048.
[87] A. I. Rat’ko, A. I. Ivanets, A. I. Kulak, Y. Morozov, and I. O. Sakhar, “Thermal decomposition of natural dolomite,” vol. 47, no. 12, pp. 1372–1377, Nov. 2011, doi: https://doi.org/10.1134/s0020168511120156.
[88] S. Ke, X. Cheng, Y. Wang, Q. Wang, and H. Wang, “Dolomite, wollastonite and calcite as different CaO sources in anorthite-based porcelain,” Ceramics International, vol. 39, no. 5, pp. 4953–4960, Jul. 2013, doi: https://doi.org/10.1016/j.ceramint.2012.11.091.
[89] M. JANKULA et al., “The influence of heat on elastic properties of illitic clay Radobica,” Journal of the Ceramic Society of Japan, vol. 123, no. 1441, pp. 874–879, 2015, doi: https://doi.org/10.2109/jcersj2.123.874.
[90] H. Cengizler, “Effect of calcination temperature on use of high-boron-content waste for low-temperature wall tile production,” Ceramics International, vol. 48, no. 5, pp. 6024–6036, Nov. 2021, doi: https://doi.org/10.1016/j.ceramint.2021.11.138.
[91] S. L. Correia, K. A. S. Curto, D. Hotza, and A. M. Segadães, “Using Experiments Design to Model Linear Firing Shrinkage of Triaxial Ceramic Bodies,” Materials Science Forum, vol. 498–499, pp. 430–435, Nov. 2005, doi: https://doi.org/10.4028/www.scientific.net/msf.498-499.430.
[92] S. OUMMADI, “Drying behaviour of ceramic green bodies: experimental characterization and numerical modeling,” Dec. 2019. Available: https://theses.hal.science/tel-02495750
[93] Y. Cheng et al., “Dehydroxylation and Structural Distortion of Kaolinite as a High-Temperature Sorbent in the Furnace,” vol. 9, no. 10, pp. 587–587, Sep. 2019, doi: https://doi.org/10.3390/min9100587.
[94] Pagliari, L., Dapiaggi, M., Pavese, A., & Francescon, F. (2013). A kinetic study of the quartz–cristobalite phase transition. Journal of the European Ceramic Society, 33(15-16), 3403–3410. doi:10.1016/j.jeurceramsoc.2013.06.014
[95] Ptáček, P., Šoukal, F., Opravil, T., Havlica, J., & Brandštetr, J. (2013). Crystallization of spinel phase from metakaoline: The nonisothermal thermodilatometric CRH study. Powder Technology, 243, 40–45. doi:10.1016/j.powtec.2013.03.031
[96] M. Romero; J. Martín-Márquez; J.Ma. Rincón (2006). Kinetic of mullite formation from a porcelain stoneware body for tiles production. , 26(9), 1647–1652. doi:10.1016/j.jeurceramsoc.2005.03.235
[97] M. Olszak-Humienik and M. Jablonski, “Thermal behavior of natural dolomite,” Journal of Thermal Analysis and Calorimetry, vol. 119, no. 3, pp. 2239–2248, Dec. 2014, doi: https://doi.org/10.1007/s10973-014-4301-6.

[98] Ptáček, P., Opravil, T., & Šoukal, F. (2016). Introduction of novel kinetic approach to calculation of activation energy and its application to the sinter-crystallization of strontian feldspar. Ceramics International, 42(15), 16969–16980. doi:10.1016/j.ceramint.2016.07.203
[99] AmorÃ³s, J.L.; Blasco, E.; Moreno, A.; MarÃ-n, N.; Feliu, C. (2020). Sinter-crystallisation kinetics of a SiOâ€ "AlOâ€ "CaOâ€ "MgOâ€ "SrO glass-ceramic glaze. Journal of Non-Crystalline Solids, 532(), 119900–. doi:10.1016/j.jnoncrysol.2020.119900
[100]AmorÃ³s, J.L.; Blasco, E.; Moreno, A.; MarÃ-n, N.; Feliu, C. (2020). Sinter-crystallisation kinetics of a SiOâ€ "AlOâ€ "CaOâ€ "MgOâ€ "SrO glass-ceramic glaze. Journal of Non-Crystalline Solids, 532(), 119900–. doi:10.1016/j.jnoncrysol.2020.119900
[101]W.-C.R. Chan, Kelbon Marica, B.B. Krieger, Modeling and experimental verification of physical and chemical process during pyrolysis of a large biomass particle, Fuel 64 (1985) 1505e1513
[102]Y. Kobayashi, H. Maekawa, W. Okuno, T. Mizuno, T. Sugimura, and A. Negawa, "Effect of quartz grain size on elastic and thermal expansion properties of porcelain," Journal of the Ceramic Society of Japan, vol. 131, no. 8, pp. 451–457, Aug. 2023, doi: https://doi.org/10.2109/jcersj2.23050.
[103]Igor Štubňa, Marek Mánik, Tomáš Húlan, and A. Trník, "Development of stress on quartz grain in illite ceramics during cooling stage of firing," Journal of the Ceramic Society of Japan, vol. 128, no. 3, pp. 117–123, Mar. 2020, doi: https://doi.org/10.2109/jcersj2.19169.
[104]Alves and João Baptista Baldo, "The Threshold Percolation Volume Fraction of Vitreous Silica on the Thermal Expansion Behavior of Quartz," Journal of Materials Science and Chemical Engineering, vol. 07, no. 06, pp. 1–6, Jan. 2019, doi: https://doi.org/10.4236/msce.2019.76001.
[105]H. S. Houldsworth and J. W. Cobb, "THE REVERSIBLE THERMAL EXPANSION OF REFRACTORY MATERIALS," Journal of the American Ceramic Society, vol. 6, no. 5, pp. 645–662, May 1923, doi: https://doi.org/10.1111/j.1151-2916.1923.tb18141.x.
[106]"Volume Changes in Porcelain Bodies During the Cooling Phase After Firing." Accessed: Aug. 22, 2024. [Online]. Available: https://www.tainstruments.com/pdf/literature/DIL002.pdf
[107]E. Sánchez et al., "Residual stresses in porcelain tiles. Measurement and process variables assessment," Journal of the European Ceramic Society, vol. 39, no. 11, pp. 3364–3372, Sep. 2019, doi: https://doi.org/10.1016/j.jeurceramsoc.2019.04.038.
[108]Ludmila Mahnicka-Goremikina, Ruta Svinka, Visvaldis Svinka, Liga Grase, and Vadims Goremikins, "The formation of phases with low or negative linear thermal expansion coefficient in porous mullite ceramics," Epitoanyag-Journal of Silicate Based and Composite Materials, vol. 72, no. 3, pp. 91–98, Jan. 2020, doi: https://doi.org/10.14382/epitoanyag-jsbcm.2020.15.
[109]Mechanical and Thermal Properties of Ceramics Proceedings of a Symposium Held at Gaithersburg, Maryland chrome-extension://efaidnbmnnnibpcajpcglclefindmkaj/https://nvlpubs.nist.gov/nistpubs/Legacy/SP/nbsspecialpublication303.pdf https://www.expertlabservice.it/en/publication/the-effect-of-cooling-rate-on-the-specific-volume-of-glassy-phases/
[110]J. E. K. Schawe and J. F. Löffler, "Existence of multiple critical cooling rates which generate different types of monolithic metallic glass," *Nature Communications*, vol. 10, no. 1, Mar. 2019, doi: https://doi.org/10.1038/s41467-018-07930-3.
[111]Johnson, J. S., Clark, J., Miller-Antonio, S., Robins, D., Schiffer, M. B., & Skibo, J. M. (1988). Effects of firing temperature on the fate of naturally occurring organic matter in clays. Journal of Archaeological
[112]Leinweber, P., & Schulten, H.-R. (1992). Differential thermal analysis, thermogravimetry and in-source pyrolysis-mass spectrometry studies on the formation of soil organic matter. Thermochimica Acta,
[113]J. M. N. Jayaweera, M. Narayana, and S. U. Adikary, "Numerical Modeling of Drying Behavior of Sri Lankan Kaolin," in 2021 Moratuwa Engineering Research Conference

(MERCon), Moratuwa, Sri Lanka: IEEE, Jul. 2021, pp. 48–53. doi: 10.1109/MERCon52712.2021.9525774.

[114]P. Niedoba, L. Čermák, and M. Jícha, “Meshfree methods for computational fluid dynamics,” EPJ Web of Conferences, vol. 45, p. 01068, 2013, doi: https://doi.org/10.1051/epjconf/20134501068.

[115]J. J. Monaghan, “Smoothed particle hydrodynamics.” Reports on Progress in Physics, Institute of Physics Publishing, Jul. 2005, vol. 68(8), pp.1703–1759. doi:10.1088/0034-4885/68/8/r01

[116]W. A. M. K. P. Wickramaarachchi and M. Narayana, “Pyrolysis of single biomass particle using three-dimensional Computational Fluid Dynamics modelling,” Renewable Energy, vol. 146, pp. 1153–1165, Feb. 2020, doi: https://doi.org/10.1016/j.renene.2019.07.001.

[117]Montorfano, F. Piscaglia, and A. Onorati, “An Extension of the Dynamic Mesh Handling with Topological Changes for LES of ICE in OpenFOAM®,” SAE technical papers on CD-ROM/SAE technical paper series, Apr. 2015, doi: https://doi.org/10.4271/2015-01-0384.

[118] H. Jasak, “Dynamic Mesh Handling in OpenFOAM,” in 47th AIAA Aerospace Sciences Meeting including The New Horizons Forum and Aerospace Exposition, Reston, Virigina: American Institute of Aeronautics and Astronautics, Jan. 2009, doi: http://dx.doi.org/10.2514/6.2009-341